

MASTER OF SCIENCE THESIS

---

# **Influence of flexibility on the clap and peel movement of the DelFly II**

**A numerical study on flexible flapping wings**

**Thijs Gillebaart**

---

September 26, 2011



# **Influence of flexibility on the clap and peel movement of the DelFly II**

**A numerical study on flexible flapping wings**

THIJS GILLEBAART

Submitted in partial fulfillment of the requirements for the degree of  
Master of Science

September 26, 2011



**Delft University of Technology**

Copyright © Thijs Gillebaart, TU Delft  
All rights reserved.

DELFT UNIVERSITY OF TECHNOLOGY  
DEPARTMENT OF  
AEROSPACE DESIGN, INTEGRATION & OPERATIONS  
AERODYNAMICS CHAIR

The undersigned hereby certify that they have read and recommend to the Faculty of Aerospace Engineering for acceptance the thesis entitled **“Influence of flexibility on the clap and peel movement of the DelFly II”** by **Thijs Gillebaart** in fulfillment of the requirements for the degree of **Master of Science**.

Dated: September 26, 2011

Examination committee:

---

prof. dr. ir. drs. H. Bijl

---

dr. ir. A.H. van Zuijlen

---

dr. ir. B.W. van Oudheusden

---

dr. ir. F.M. Bos

---

ir. B.D.W. Remes



# Acknowledgements

In the past year the help and motivation of a lot of people helped me reach my goal of finishing my aerodynamics master. I would like to acknowledge these people here for their support.

First of all, I would like to thank my supervisors Hester Bijl, Alexander van Zuijlen en Wee-Beng Tay. They gave crucial input during my thesis and helped me when problems arose. A special note for Alexander van Zuijlen who always had time for me to discuss the problems and their possible solutions.

Secondly I would like to thank all student in the graduation room at the aerodynamics department for their input and ideas given during one of the many lunches or coffee breaks. Without those discussions it would not have been as exciting as it was now.

Also thanks to Zeljko Tukovic for providing me with his code and his help in implementing the code into OpenFOAM.

Last but most certainly not least, special thanks to my family and my friends for supporting me during the past years.

Thijs Gillebaart  
Delft, September 26, 2011



## Summary

*“The influence of wing flexibility on the performance of the ‘clap-and-peel’ motion in hovering conditions.”*

Although wide range of studies have been performed on the principles of flapping flight, only recently the influence of flexibility on flapping flight and in particular the influence of flexibility on the performance of the ‘clap-and-peel’ motion have been performed. In this thesis new methods and higher Reynolds number flows are used together with experimentally obtained deforming wing shapes of the DelFly II to determine the influence of flexibility on the aerodynamics both in single wing flight and in the ‘clap-and-peel’ motion during hovering conditions.

Two-dimensional computational fluid dynamic simulations are used to perform this study. The arbitrary Lagrangian Eulerian (ALE) unsteady incompressible laminar Navier-Stokes (NS) are modelled in OpenFOAM using a finite volume approach. To move the mesh based on the wing motion, radial basis functions (RBF) are used. By interpolating the motion of the wing to the mesh using RBF mesh interpolation a smoothly deforming mesh is produced. By using a double row of control points it is ensured that the RBF mesh interpolation includes rotation and translation such that the mesh quality is preserved during the complete flapping cycle.

Based on experimental results the periodic chord wise deformation at 71 % of the span of the three dimensional DelFly II wing is obtained. To use these shapes in the simulations, spline interpolation is used in space and Fourier series interpolation is used in time. However the number of Fourier modes used has a direct influence on the forces due to the acceleration of the wing. The frequency of the highest mode is dominating the acceleration, which dominates the frequency of the forces. These excessive acceleration obscure the results and therefore only 4 Fourier modes are used.

Next to this DelFly II like wing three extra wing kinematics are derived. First a rigid wing movement is developed to compare the results of the flexible wing to. Two extra wings, a semi-flexible and a super-flexible, are created to determine if a trend is present when the flexibility is increased or decreased. In both the simulations with a single wing or the ‘clap-and-peel’ motion all four wings are used to determine the influence of flexibility.

Simulating the ‘clap-and-peel’ motion cannot be done with the ALE approach taken for the single wing motion, as the gap between the two wings becomes too small in the clapping phase. By immersing a symmetry plane in the computational domain and enforcing the symmetry conditions at that location the second wing is modelled, while the mesh can still be deformed using RBF as if there was only one wing. Two methods are developed and tested to enforce these symmetry conditions: an immersed symmetry plane with explicit interpolation and a mesh topology chang-

ing method to enforce the symmetry conditions implicitly at the exact location. To validate and compare these methods the Miller and Peskin motion from [25] is used together with the DelFly motion. From the comparison with [25] it is clear that the method of using a symmetry plane to model the second wing is valid. However the immersed symmetry plane method with explicit interpolation shows large numerical oscillations in the DelFly simulations. Smoothing the results does generate a reasonable curve, but the results from the topology changing method do not contain these oscillations. Together with the implicit enforcement of the conditions this topology changing method out performs the explicit method.

Due to the hovering conditions vortices and aerodynamic structures are not convected away from the wing by a global convective flow. As a result shed vortices interact with the wing at irregular intervals causing a periodic chaotic flow. The periodic motion causes periodic characteristics in the flow, but they are obscured by the chaotic interaction between the vortices itself and between the vortices and the wing. This chaotic behaviour causes a very sensitive problem: Each solver parameter introduces a small off-set in the simulation which grows exponentially until the off-set is in the order of the result itself. Instantaneous results can thus not be compared properly. To cope with this a large number of periods (44) is simulated to create a periodic average. A periodic flow is created by adding a free-stream velocity through the field. These two solutions provide the tools to further analyse the results obtained in the mesh study, Courant number study and the influence of flexibility study.

The mesh study shows that the normal mesh (60.000 cells) provides a good trade-off between accuracy and efficiency. However, since the topology changing method for the enforcement of the symmetry conditions can not be performed in parallel, the coarse mesh (15000 cells) is used for the 'clap-and-peel' motion simulations. The Courant number study shows that a Courant number of 0.4 provides good accuracy. Higher Courant numbers are not used due to the immersed symmetry plane methods, which cannot handle high Courant numbers.

In the single wing simulations a clear trend is found: increasing flexibility increases the integrated periodic average upward force. Three mechanisms contribute to this trend. Firstly the ability to bend the leading edge before translation causes a lower angle of attack at the leading edge. This lower angle of attack ensures the stable development of a single strong LEV vortex. For the rigid wing the leading edge angle of attack is too high causing a shedding of the first LEV. Secondly the orientation of the flexible wings during stroke reversal causes more effective horizontal wing area. Thirdly the capturing and/or interaction of the previously shed vortices limits the development of the LEV slightly for the flexible wings causing a negative impact on the force production. In all three phenomena the bending of the leading edge is of major importance.

For the 'clap-and-peel' motion a similar trend can be found. An increase in integrated periodic average upward force is found when flexibility is increased. Also

the force per wing is higher in the 'clap-and-peel' motion for all four wings. The influence of flexibility show similar phenomena. Again the angle of attack causes the main difference. The other two phenomena are also present, even though the difference between the capturing of the previously shed vortex for the different wings diminishes in the 'clap-and-peel' motion. An extra phenomena is found during the clap phase. Due to the higher acceleration during the clap phase for a more flexible wing, higher forces are generated when flexibility is increased. However the validity of these high accelerations are doubtful, due to the major influence of fluid-structure interaction in this phase for very flexible wings, which is completely ignored in these simulations.

For both motions and all four wing kinematics the required energy is calculated based on the assumption of passive flexibility. Looking at the ratio of integrated periodic average upward force over the required energy a clear trend is found. For both the single wing motion and the 'clap-and-peel' motion this efficiency term increases for more flexible wings. However this is only a first indication because in the simulations active flexibility is simulated. Still these results show a promising trend for both the use of flexible wings and the 'clap-and-peel' motion.

Also the gap size between the 'two' wings is varied for the DelFly motion and the rotated DelFly motion. Both results show no significant influence on the integrated forces. In the instantaneous forces a clear increase in force can be found during the clap phase. This is caused due to the higher pressure between the wings for smaller gap sizes.

From these results it can be concluded that the ALE Navier-Stokes together with the RBF mesh interpolation provide a good and robust tool to simulate deforming flapping wings. Also the newly developed mesh topology changing method provides a reliable tool in simulating two clapping wings. The aerodynamic caused by the enforcement of a deformable wing is highly depending on the acceleration introduced due to the interpolation. By choosing a low number of Fourier modes the results are not obscured by these excessive accelerations.

Chaotic flow is produced during hovering conditions. By applying a free-stream velocity through the domain a periodic flow is obtained. Averaging over a large number of periods provide a converged periodic average. From these periodic averages for the different wings it is clear that increasing flexibility increases the force produced and the efficiency. This is the case for both single wing motion and the 'clap-and-peel' motion. The main phenomena is the stable development and attachment of the LEV for the more flexible wings due to the lower angle of attack at the start of the out-stroke. The forces per wing also increase when the 'clap-and-peel' motion is compared to the single wing motion. Higher velocities over the leading edge during the peel phase, caused by the low pressure region between the wings, result in a stronger LEV and thus higher forces. Both flexibility and the 'clap-and-peel' motion are potentially efficient and good mechanisms to increase the upward force generated during hovering flapping flight.

Further investigation is needed by introducing fluid-structure interaction. This will damp the acceleration and will make the problem less sensitive. Three-dimensional simulations are needed to check whether similar phenomena can be observed when flexibility is changed. Combining these two improvement will results in new insight in the influence of flexibility in the 'clap-and-peel' motion.

# List of Symbols

## Greek Symbols

$\Delta\alpha$	Angular amplitude . . . . .	[–]
$\Delta\tau_{acc}$	Normalized acceleration duration . . . . .	[–]
$\Delta\tau_{dec}$	Normalized deceleration duration . . . . .	[–]
$\Delta\tau_{rot}$	Normalized rotation duration . . . . .	[–]
$\lambda$	Heat conduction transport coefficient . . . . .	[W/m/K]
$\lambda_i$	RBF weighting coefficients . . . . .	[–]
$\mu$	Dynamic viscosity . . . . .	[Ns/m <sup>2</sup> ]
$\nu$	Kinematic viscosity . . . . .	[m <sup>2</sup> /s]
$\omega_{rot}$	Normalized rotational velocity . . . . .	[–]
$\phi$	Flux . . . . .	[m <sup>3</sup> /s]
$\Phi_{cc}$	Basis function matrix . . . . .	[m]
$\phi_{mf}$	Mesh face flux . . . . .	[m <sup>3</sup> /s]
$\rho$	Density . . . . .	[kg/m <sup>3</sup> ]
$\rho^*$	Dimensionless density . . . . .	[–]
$\rho_{ref}$	Reference density . . . . .	[kg/m <sup>3</sup> ]
$\sigma$	Stress tensor . . . . .	[N/m <sup>2</sup> ]
$\tau$	Normalized time . . . . .	[–]
$\tau_{acc}$	Normalized acceleration delay time . . . . .	[–]
$\tau_{dec}$	Normalized deceleration delay time . . . . .	[–]
$\tau_{rot}$	Normalized rotation delay time . . . . .	[–]
$\xi$	Polynomial coefficients . . . . .	[–]

## Latin Symbols

$\bar{C}_X$	Integrated periodic average horizontal force coefficient . . . . .	[–]
$\bar{C}_Y$	Integrated periodic average upward force coefficient . . . . .	[–]
$\Delta \mathbf{x}_i$	Moving internal points displacement . . . . .	[m]
$\Delta \mathbf{x}_m$	Moving control points displacement . . . . .	[m]
$\mathbf{q}$	Heat flux . . . . .	[W/s]
$\mathbf{u}$	Flow velocity vector . . . . .	[m/s]
$\mathbf{u}^*$	Dimensionless flow velocity vector . . . . .	[–]
$\mathbf{u}_{mf}$	Mesh face velocity vector . . . . .	[m/s]
$\mathbf{u}_m$	Mesh velocity vector . . . . .	[m/s]
$\mathbf{x}_c$	Control point displacement . . . . .	[m]
$\mathbf{x}_{DelFly}$	Delfly wing position . . . . .	[m]
$\mathbf{x}_{flex}$	Scaled new flexible wing position . . . . .	[m]
$\mathbf{x}_{flex}^*$	Non-scaled new flexible wing position . . . . .	[m]
$\mathbf{x}_{LE}$	Leading edge position . . . . .	[m]
$\mathbf{x}_{rigid}$	Rigid wing position . . . . .	[m]
$A_{flex}$	Flex parameter . . . . .	[–]
$C_X$	Horizontal force coefficient . . . . .	[–]
$C_Y$	Upward force coefficient . . . . .	[–]
$Co$	Courant number . . . . .	[–]
$E$	Required energy coefficient . . . . .	[–]
$e$	Total specific energy . . . . .	[J/kg]
$f$	Frequency . . . . .	[Hz]
$F_{inert}$	Inertia forces . . . . .	[N]
$f_{ref}$	Reference frequency . . . . .	[Hz]
$F_{visc}$	Viscous forces . . . . .	[N]

$H_m$	Moving RBF evaluation matrix	[–]
$L_{DelFly}$	DeIFly wing length	[m]
$L_{flex}^*$	Non-scaled new flexible wing length	[m]
$L_{ref}$	Reference length	[m]
$N_c$	Number of control points	[–]
$p$	Pressure	[N/m <sup>2</sup> ]
$p^*$	Dimensionless pressure	[–]
$Q$	Nett energy generation	[Jm <sup>3</sup> /kg]
$Q_c$	Polynomial matrix	[m]
$R$	Specific gas constant	[J/mol/K]
$Re$	Reynolds number	[–]
$S_f$	Face surface area normal	[m <sup>2</sup> ]
$St$	Strouhal number	[–]
$T$	Temperature	[K]
$t$	Time	[s]
$t^*$	Dimensionless time	[–]
$T_{conv}$	Convective time scale	[s]
$T_{motion}$	Flapping time scale	[s]
$U_{ref}$	Reference velocity	[m/s]
$V$	Maximum translational velocity	[m/s]
$V_C$	Control volume	[m <sup>3</sup> ]
$V_P$	Cell volume	[m <sup>3</sup> ]



# Contents

<b>List of Symbols</b>	<b>ix</b>
<b>1 Introduction</b>	<b>1</b>
<b>2 Governing equations</b>	<b>3</b>
2.1 Navier-stokes equations . . . . .	3
2.1.1 Incompressible laminar flow . . . . .	4
2.1.2 Dimensionless form of the incompressible N-S . . . . .	5
2.2 Navier-Stokes in finite volume form . . . . .	6
2.2.1 Discrete finite volume formulation of the Navier-Stokes equations	6
Temporal term . . . . .	7
Convective term . . . . .	7
Diffusive term . . . . .	8
Pressure term . . . . .	8
2.2.2 Solving the equation using PISO . . . . .	8
2.3 Including moving meshes . . . . .	10
2.3.1 Arbitrary Lagrangian-Eulerian (ALE) Navier-Stokes equation . .	10
2.3.2 PISO algorithm including moving meshes . . . . .	11
<b>3 Mesh movement</b>	<b>13</b>
3.1 RBF mesh interpolation . . . . .	13
3.2 RBF interpolation in OpenFOAM . . . . .	14
3.3 Mesh quality for ‘zero-thickness’ wing . . . . .	16
<b>4 Wing kinematics</b>	<b>19</b>
4.1 DelFly II wing kinematics . . . . .	19
4.1.1 Wing shape approximation in space . . . . .	20
4.1.2 Interpolating the wing shape in time . . . . .	21
4.1.3 Motion characteristics . . . . .	22

4.2	Influence of Fourier modes on forces . . . . .	24
4.3	Equivalent rigid wings . . . . .	25
4.3.1	Purely translating rigid wing . . . . .	26
4.3.2	Equivalent rigid pitching wing . . . . .	27
4.4	Semi-flexible and super flexible wings . . . . .	28
4.5	Miller-Peskin rigid wing . . . . .	28
<b>5</b>	<b>Methods to simulate 'clap-and-peel'</b>	<b>33</b>
5.1	Changing mesh topology . . . . .	33
5.1.1	Method description . . . . .	33
	Move symmetry plane faces . . . . .	34
	Redefining the old mesh . . . . .	34
	Split the mesh at symmetry plane . . . . .	35
	Interpolating at symmetry plane . . . . .	36
	Solving the fluid equations . . . . .	36
5.1.2	Changes in the DGCL . . . . .	36
5.1.3	Overview of method . . . . .	37
5.2	Immersed symmetry plane (ISP) method . . . . .	37
5.2.1	Cell and face identification . . . . .	38
5.2.2	Set velocity values at boundary and solve the momentum equation	39
5.2.3	Correct fluxes . . . . .	39
5.2.4	Solve pressure equation and correct for symmetry conditions . .	39
5.2.5	Iterations within a single time step . . . . .	40
<b>6</b>	<b>Chaotic flow behaviour</b>	<b>41</b>
6.1	Quantifying chaotic flow . . . . .	42
6.2	Periodic solution with free-stream velocity . . . . .	43
6.3	Determining the order of instability . . . . .	44
6.3.1	Tolerance . . . . .	45
6.3.2	Parallel computing . . . . .	46
6.3.3	Initial conditions . . . . .	46

6.3.4	Linear solver . . . . .	47
6.4	Coping with 'periodic chaos' . . . . .	47
<b>7</b>	<b>Mesh study and time step</b>	<b>51</b>
7.1	Mesh study . . . . .	51
7.1.1	Periodic flow . . . . .	51
7.1.2	Chaotic flow . . . . .	53
7.2	Influence of the Courant number . . . . .	54
7.2.1	Periodic flow . . . . .	54
7.2.2	Chaotic flow . . . . .	56
<b>8</b>	<b>Results</b>	<b>59</b>
8.1	Influence of flexibility for a single wing . . . . .	59
8.2	Clap and peel with flexible and rigid wings . . . . .	64
8.2.1	Method comparison . . . . .	64
Miller-Peskin motion	. . . . .	64
DeFly II motion	. . . . .	66
8.2.2	Validation with Miller-Peskin . . . . .	69
Fling . . . . .	. . . . .	69
Clap and fling . . . . .	. . . . .	72
Influence of wing thickness . . . . .	. . . . .	72
8.2.3	Influence of flexibility . . . . .	75
8.3	Rotated wing and gap size . . . . .	81
8.3.1	Rotated wing . . . . .	81
8.3.2	Influence of the gap size . . . . .	82
Original wing . . . . .	. . . . .	83
Rotated wing . . . . .	. . . . .	84
Original versus rotated wing . . . . .	. . . . .	85
<b>9</b>	<b>Conclusion and recommendations</b>	<b>87</b>
9.1	Conclusions . . . . .	87
RBF mesh interpolation . . . . .	. . . . .	87

Enforcing the wing kinematics . . . . .	87
Periodic chaotic flow . . . . .	88
Mesh and Courant number study . . . . .	88
Symmetry plane method comparison . . . . .	89
Influence of flexibility . . . . .	89
Influence of 'clap-and-peel' . . . . .	91
Gap size influence . . . . .	91
Final conclusions . . . . .	92
9.2 Recommendations . . . . .	92
<b>Appendices</b>	
<b>A Solver charts</b>	<b>I</b>
<b>B Fourier coefficients</b>	<b>V</b>
<b>References</b>	<b>VIII</b>

# 1

## Introduction

Research into flapping wings started more than 100 years ago when biologists starting looking into bird and insect flight in more detail ([7, 8]). After this, numerous studies have been performed into the flight motion and power (metabolism) in insect and bird flight. In the same period aerodynamicists focused on the different flow phenomena present in flapping flight. This started with studies into the effect of the angle of attack ([4, 20]). A break through in determining the important flow phenomena of flapping flight was achieved by [13], which identified the attached leading edge vortex do be the dominating aerodynamic phenomena in flapping flight. In [33] the first study into the 'clap-and-peel' motion are performed and show the potential of this mechanism. Numerical simulations on flapping wings with the Unsteady Navier-Stokes equation started in 1998 by [23], while before this vortex models or quasi-steady models were used. Only recently studies on the influence of flexibility have been performed by [2, 9, 15, 35]. These studies show that flexibility can be used to improve the lifting forces and/or efficiency. However only a single study focused on the influence of the wing flexibility and deformation on the 'clap-and-peel' motion (see [26]), while the potential of both the benefits of flexibility and the 'clap-and-peel' motion can result in an efficient flapping mechanism. In [26] an immersed boundary method is used to simulate the fling and 'clap-and-peel' motion at low Reynolds numbers (up to 128). Results show that flexibility can increase both the efficiency and lift forces in the 'clap-and-peel' motion.

In this study the influence of a flexible wing on the 'clap-and-peel' motion will be studied by applying the Arbitrary Lagrangian Eulerian (ALE) Navier-Stokes equations and a new immersed symmetry plane method. To generate the flexible wings experimental results of the deforming DelFly II wings are used to enforce these deforming shapes in the simulations. The goal is to investigate the influence of wing flexibility on the performance of the 'clap-and-peel' motion for a hovering DelFly II like wing.

Full fluid-structure interaction is not possible, since the structural properties of the DelFly II wings are unknown. Therefore the deforming wing is imposed based on experimental measurements to model 'flexibility'. To determine the influence of flexibility three additional wings are derived from the experimental wing shapes: an equivalent rigid wing, a super-flexible wing and a semi-flexible wing.

Enforcing a deforming wing requires a tool to incorporate this in fluid simulations. Because of the moderately high Reynolds number (9600) the ALE approach is used. To deform the mesh, radial basis function (RBF) mesh interpolation is used, which can preserve the mesh quality for large translations and rotations. The RBF mesh interpolation is further implemented to generate an efficient and smooth method to deform the mesh based on the flexible wing movement.

The flexible wing shapes are obtained from previously performed experiments. By interpolating in space using splines and in time by using Fourier interpolation, the flexible shape is known throughout the complete flapping cycle. With this interpolation additionally problems arise due to the absence of fluid-structure interaction and the direct enforcement of the wing acceleration on the flow. Therefore the interpolation must be chosen such that the goal, which is the study into the influence of flexibility, can be achieved.

Additionally a tool is developed to simulate the 'clap-and-peel' motion. The standard ALE approach fails due to the small gap between the wings in the clap phase. By introducing an immersed symmetry plane into the computational domain and enforcing the symmetry conditions on the flow the second wing is modelled, while the mesh is still deformed as if only one wing is present. Two methods are developed, tested and validated to determine which method performs best. The first method is based on explicit interpolation from the immersed symmetry plane to the fluid field and the second method is a topology changing method to construct a computational boundary where the conditions can be imposed implicitly. For the validation the results from [25] are used, which simulated rigid flapping wings performing the 'clap-and-fling' motion at low Reynolds numbers using two-dimensional simulations. With these methods the four wings are simulated both in the single wing motion and the 'clap-and-peel' motion.

Based on the upward force coefficient, vorticity fields and the required energy needed for a single flapping cycle the performance of flexible wings in 'clap-and-peel' motion is analysed. From this analysis conclusions can be reached on the influence of flexibility in single wing motion and the 'clap-and-peel' motion. Also the performance of the 'clap-and-peel' motion when compared to a single wing motion is determined.

The set-up, results and conclusions are presented in nine chapters. First the governing equations, which are the ALE Navier-Stokes equations, are explained in Chapter 2. After this (Chapter 3) the RBF mesh interpolation algorithm and the implementation in OpenFOAM is discussed. In this chapter the mesh quality throughout the period is discussed for two methods of controlling the RBF mesh interpolation. All wing kinematics used during the study are shown in Chapter 4. In Chapter 5 the two methods to simulate the 'clap-and-peel' motion are discussed. Due to the hovering conditions chaotic periodic flow is present. How this is handled is shown in Chapter 6. A study on the influence of mesh density and Courant number is performed in Chapter 7. In Chapter 8 all results concerning influence of flexibility and the performance of the different methods are stated. Finally the conclusions and recommendations can be found in Chapter 9.

# 2

## Governing equations

To simulate fluid movement due to a flapping wing, a set of equations describing the fluid movement is required. In fluid dynamics the Navier-Stokes equations describe the movement of a fluid. Generally flapping flight is used at Reynolds numbers ranging from 10 to  $10^5$  ([29]). Due to the low Reynolds number and the low velocities in the fluid the unsteady, incompressible laminar Navier-Stokes equations are used. Other studies, such as [6],[12] and [30] have taken the same approach. In this chapter it is shown how the final equations used in OpenFOAM are derived from the full Navier-Stokes equations.

### 2.1 Navier-stokes equations

The starting point of this derivation is the full set of Navier-Stokes equations. An unsteady, compressible and viscous fluid is described by this set of equations. Different forms of the Navier-Stokes equations can be used as shown in [1],[34] and [6]. Applying the three conservation laws (mass, momentum and energy) to a fluid the Navier-Stokes equations are derived. Here the vector form of the Navier-Stokes equations are stated. Conservation of mass for a fluid is shown in equation 2.1.

$$\frac{\partial \rho}{\partial t} + \nabla \bullet (\rho \mathbf{u}) = 0 \quad (2.1)$$

In this equation  $\rho$  [kg/m<sup>3</sup>] is the fluid density and  $\mathbf{u}$  [m/s] is the flow velocity vector. The definition of the  $\nabla$  operator in three dimension is

$$\nabla = \begin{pmatrix} \frac{\partial}{\partial x} \\ \frac{\partial}{\partial y} \\ \frac{\partial}{\partial z} \end{pmatrix} \quad (2.2)$$

Next equation is the conservation of momentum. In this equation gravity and additional body forces are neglected. The result is stated in equation 2.3.

$$\frac{\partial \rho \mathbf{u}}{\partial t} + \nabla \bullet (\rho \mathbf{u} \mathbf{u}) = \nabla \bullet \sigma \quad (2.3)$$

$\sigma$  [N/m<sup>2</sup>] is the stress tensor, which is needed for viscous flows. Finally the conservation of energy is needed. In equation 2.4 the conservation of energy is shown.

$$\frac{\partial \rho e}{\partial t} + \nabla \bullet (\rho e \mathbf{u}) = \nabla \bullet (\sigma \mathbf{u}) - \nabla \bullet \mathbf{q} + \rho Q \quad (2.4)$$

In this equation  $e$  [J/kg] equals the total specific energy,  $\mathbf{q}$  [W/s] is the heat flux vector and  $Q$  [J m<sup>3</sup>/kg] is the nett energy generation. Together these equations form the full Navier-Stokes equations. However these three equations cannot be solved for all variables in the equation. To solve these equations constitutive relations are needed to close the set of equations. First is the stress tensor, which for a Newtonian fluid, can be defined as

$$\sigma = - \left( p + \frac{2}{3} \mu \nabla \bullet \mathbf{u} \right) \mathbf{I} + \mu (\nabla \mathbf{u} + \nabla \mathbf{u}^T) \quad (2.5)$$

$\mathbf{I}$  is the identity tensor,  $p$  [N/m<sup>2</sup>] represents the pressure and  $\mu$  [Ns/m<sup>2</sup>] equals the dynamic viscosity. Next the equation of state, here the perfect gas law, is used to close the energy equation.

$$p = \rho R T \quad (2.6)$$

$R$  [J/(mol K)] is the specific gas constant and  $T$  [K] the temperature. The constitutive relation for the total specific energy is as follows:

$$e = e(p, T) \quad (2.7)$$

Modelling the heat conduction is done with Fourier's law and is shown below.

$$\mathbf{q} = \lambda \nabla T \quad (2.8)$$

In this equation  $\lambda$  [W/(m K)] is the heat conduction transport coefficient.

### 2.1.1 Incompressible laminar flow

The first simplification of the full Navier-Stokes equation is assuming incompressible flow. When a flow with a Mach number lower than 0.3 is considered the incompressible Navier-Stokes equations describe this flow accurately. Due to the small size of this problem (chord of 7.4 cm and frequency of 11 Hz) the Mach number does not reach this value ([32]). [23] was the first to use it in 1998 and after this the incompressible form of the Navier-Stokes equations (N-S) is used in simulating flapping flight, also by [6]. Secondly is the assumption of laminar flow. The Reynolds number for insects vary from 10 to 10,000 and for birds up to 10<sup>5</sup> as [12] states. Because of this the flow can be assumed laminar for insect flight. For bird flight near a Reynolds number of 10<sup>5</sup> this assumption becomes invalid. This form of the Navier-Stokes equations is used for flapping flight from the moment [23] applied them to the flapping wing aerodynamics and validated them more extensively in

[22]. [6] also validates these assumptions for the lower Reynolds numbers. Applying these assumption results in Equations (2.9) and (2.10), known as the unsteady, incompressible laminar Navier-Stokes equations.

$$\nabla \bullet \mathbf{u} = 0 \quad (2.9)$$

$$\frac{\partial \mathbf{u}}{\partial t} + \nabla \bullet (\mathbf{u}\mathbf{u}) = -\frac{\nabla p}{\rho} + \nu \nabla^2 \mathbf{u} \quad (2.10)$$

Here  $\nu = \mu/\rho$  [m<sup>2</sup>/s] is the kinematic viscosity. An advantage of the incompressible form of the N-S is that the energy equation is not needed any more to close the model. With these two equations the fluid flow can be modelled.

### 2.1.2 Dimensionless form of the incompressible N-S

By making the Navier-Stokes equations dimensionless two important dimensionless numbers are found: Reynolds and Strouhal number. Each of the variables in Equations 2.9 and 2.10 are made dimensionless as by

$$x^* = \frac{x}{L_{ref}}, \quad \mathbf{u}^* = \frac{\mathbf{u}}{U_{ref}}, \quad \rho^* = \frac{\rho}{\rho_{ref}}, \quad p^* = \frac{p}{\rho_{ref} \cdot U_{ref}^2}, \quad t^* = t \cdot f_{ref}$$

Variables with a star (\*) represent the dimensionless variables. Since incompressible flow is assumed, the density is constant and the dimensionless density equals one. By substituting these definitions in the incompressible N-S the dimensionless form is obtained. This new set of equations is shown in equation (2.11) and (2.12).

$$\nabla \bullet \mathbf{u}^* = 0 \quad (2.11)$$

$$St \frac{\partial \mathbf{u}^*}{\partial t} + \nabla \bullet (\mathbf{u}^* \mathbf{u}^*) = -\nabla p + \frac{1}{Re} \nabla^2 \mathbf{u}^* \quad (2.12)$$

As can be seen two dimensionless numbers are present in the equations. These are known as the Strouhal ( $St$ ) and Reynolds number ( $Re$ ), from which the definitions are stated in Equations (2.13) and (2.14). When considering the Strouhal number in flapping flight the reference values can be set according to the kinematics. For the frequency the flapping frequency is chosen, while for the reference velocity the undisturbed flow velocity is chosen. When hovering conditions are considered the characteristic speed of the wing is used as reference velocity for both the Reynolds and Strouhal number. In general the reference length is chosen to be equal to the chord, but in hovering flapping flight a different length is of importance to scale the aerodynamics. In most studies the distance the wing tip travels during half a flapping cycle, or in other words the stroke amplitude, is chosen. This value is calculated by multiplying the wing span by the stroke angle amplitude.

$$Re = \frac{U_{ref} L_{ref}}{\nu} = \frac{F_{inert}}{F_{visc}} \quad (2.13)$$

$$St = \frac{f_{ref} L_{ref}}{U_{ref}} = \frac{T_{conv}}{T_{motion}} \quad (2.14)$$

In the above equations  $F_{inert}$  are the inertia forces,  $F_{visc}$  are the viscous forces,  $T_{conv}$  the convective time scale and  $T_{motion}$  is the flapping motion time scale.

## 2.2 Navier-Stokes in finite volume form

OpenFOAM uses a finite volume approximation of the dimensional Navier-Stokes equations. By taking the momentum equation from the incompressible Navier-Stokes equation (Equation (2.10)) and integrating it over a control volume ( $V_C$ ) Equation (2.15) is obtained.

$$\int_{V_C} \frac{\partial \mathbf{u}}{\partial t} dV + \int_{V_C} \nabla \cdot (\mathbf{u}\mathbf{u}) dV - \int_{V_C} \nabla \cdot (\nu \nabla \mathbf{u}) dV = \int_{V_C} \frac{\nabla p}{\rho} dV \quad (2.15)$$

Each of these terms can be computed in discrete form using Gauss' theorem based on the integral over a cell volume and its boundary (in meshes boundaries equals faces). All of the terms will be shortly discussed. For a more detailed explanation see [18] and [6].

### 2.2.1 Discrete finite volume formulation of the Navier-Stokes equations

Before looking at each term individually the general use of the volume integral, surface integral and Gauss' theorem in the finite volume method is explained. In Equation (2.16) and (2.17) the volume integral and surface integral are shown, respectively.

$$\int_{V_P} \theta(\mathbf{x}) dV \approx \theta_P V_P \quad (2.16)$$

Here  $V_P$  is the volume of the cell under consideration,  $\theta(\mathbf{x})$  is the scalar variable present in the cell and  $\theta_P$  is the average value of the scalar variable in the cell centre. A volume integral of a scalar variable is equal to the cell centre value multiplied with the cell volume. A more extensive explanation can be found in [18].

$$\int_f d\mathbf{S} \cdot \mathbf{a} = \mathbf{S}_f \cdot \mathbf{a}_f \quad (2.17)$$

Where  $S_f$  is the face surface area normal vector with a magnitude equal to the face area and  $\mathbf{a}$  is a vector variable associated with the cell and its surfaces. A relation between these two integrals exists. This relation is called the Gauss theorem and is shown in Equation (2.18).

$$\int_{V_P} \nabla \cdot \mathbf{a} dV = \oint_{S_P} d\mathbf{S} \cdot \mathbf{a} = \sum_f \int_{S_f} d\mathbf{S} \cdot \mathbf{a} \approx \sum_f \mathbf{S}_f \cdot \mathbf{a}_f \quad (2.18)$$

With these three equations the discrete form of each term in Equation (2.15) can be determined. This is done in the following sections.

### Temporal term

The first term is the temporal term, which is rather straightforward because only Equation (2.16) needs to be used besides the time discretisation. By applying the volume integral to the temporal term Equation (2.19) can be obtained.

$$\int_{V_P} \frac{\partial \mathbf{u}}{\partial t} dV = \frac{\partial \mathbf{u}}{\partial t} V_P \quad (2.19)$$

Only step left is to discretise the time derivative. It will be shortly discussed here for a uniform time step to explain the concept of first and second order approximation and the Courant number. Both terms shown here are based on the assumption of uniform mesh and fixed time step. At a later stage these two concepts will be used to explain the choices made during the study. In Equation (2.20) and (2.21) the first and second order approximation of the time derivative is shown, respectively.

$$\frac{\partial \mathbf{u}}{\partial t} V_P = \frac{\mathbf{u}^{n+1} - \mathbf{u}^n}{\Delta t} V_P = c_p \mathbf{u}_p + \mathbf{Q}_u \quad (2.20)$$

$$\frac{\partial \mathbf{u}}{\partial t} V_P = \frac{\frac{3}{2} \mathbf{u}^{n+1} - 2\mathbf{u}^n + \frac{1}{2} \mathbf{u}^{n-1}}{\Delta t} V_P = c_p \mathbf{u}_p + \mathbf{Q}_u \quad (2.21)$$

Here the superscript  $n$  indicates at which time the variable should be taken, where  $n$  is the currently known time and  $n + 1$  is the next time.  $c_p$  are diagonal terms of the sparse system of equations and  $\mathbf{Q}_u$  are the source terms associated with the temporal discretisation. To increase the order of the approximation an additional field of the variable  $\mathbf{u}$  should be available in time. Based on the time step, the face flux (derived from the velocity) and the face area the Courant number can be calculated. Equation (2.22) shows the definition of the Courant number used in OpenFOAM.

$$Co = \Delta c \frac{|\phi| \Delta t}{S_f} \quad (2.22)$$

Here  $\phi$  is the face flux,  $S_f$  is the face area and  $\Delta c$  is 1 over the distance between the cell centres belonging to the face. The Courant number is an indication of how long a ‘particle’ takes to travel through a cell. At a later stage the use of this variable is explained.

### Convective term

The second term found in the momentum equation is the convective term. As can be seen in Equation (2.15) this term is non-linear. Instead of using an expensive non-linear solver to solve for this term a Newton linearisation is used ([6]). Using this the following discrete form of the convective term can be derived.

$$\int_{V_P} \nabla \cdot (\mathbf{u}\mathbf{u}) dV = \sum_f \mathbf{S}_f \cdot \mathbf{u}_f \mathbf{u}_f = \sum_f \phi_f \mathbf{u}_f = a_p \mathbf{u}_p + \sum_N a_N \mathbf{u}_N \quad (2.23)$$

Here  $\phi_f$  is the mass flux which is given by  $\mathbf{S}_f \cdot \mathbf{u}_f$ ,  $a_p$  and  $a_N$  are the diagonal and off-diagonal terms of the sparse system of equations, respectively. The mass flux is still depending on  $\mathbf{u}$ , which makes the problem non-linear. By taking the existing velocity field to calculate this variable it is assumed that the non-linear coupling in this convective term is much smaller than the linear pressure-velocity coupling. For small time steps (or Courant numbers) this is a valid assumption ([17]). With this approximation a linear system of equations is build.

### Diffusive term

The diffusive term is the third term in the momentum equation and can be calculated using Gauss' theorem as discussed before. By applying this theorem and the surface integral in one step Equation (2.24) results.

$$\int_{V_P} \nabla \cdot (\nu \nabla \mathbf{u}) dV = \sum_f \mathbf{S}_f \cdot (\nu \nabla \mathbf{u})_f = b_p \mathbf{u}_p + \sum_N b_N \mathbf{u}_N \quad (2.24)$$

Here  $b_p$  and  $b_N$  are the diagonal and off-diagonal terms in the sparse system of equations. It can be seen that the gradient of  $\mathbf{u}$  must be known at the faces. How this is done in OpenFOAM can be found in [18]. Again this term can be constructed as a sparse system of equations as holds for the other two terms.

### Pressure term

The Gauss' theorem discussed before also holds in a similar manner for a volume integral of the gradient of a scalar variable. In this case the scalar variable is equal to the pressure. Without loss of generality it is assumed that the density is one for convenience. How to obtain the discrete finite volume form of the pressure term is shown in Equation (2.25).

$$\int_{V_P} \nabla p dV = \oint_{S_P} d\mathbf{S} p = \sum_f \int_{S_f} d\mathbf{S} p \approx \sum_f \mathbf{S}_f p_f \quad (2.25)$$

Again a sum over the faces of the cell under consideration is the result of the discretisation.

## 2.2.2 Solving the equation using PISO

The discrete finite volume form of the Navier-Stokes equations can be solved in several ways. In OpenFOAM the Pressure Implicit with Splitting of Operators (PISO) method is used ([17]). A similar short explanation of the method as shown below can be found in [6]. Lets start by grouping all the final results of the discrete finite

volume terms of the momentum equation. The results can be found in Equation (2.26).

$$\begin{aligned}
 (a_p + b_p + c_p)\mathbf{u}_p &= A_p\mathbf{u}_p = -\sum_N (a_N + b_N)\mathbf{u}_N + \mathbf{Q}_\mathbf{u} - \nabla p \\
 &= -\sum_N A_N\mathbf{u}_N + \mathbf{Q}_\mathbf{u} - \nabla p \\
 &= \mathbf{H}(\mathbf{u}) - \nabla p
 \end{aligned} \tag{2.26}$$

Together with the discretised continuity equation shown in Equation (2.27) this can be used to construct the pressure equation.

$$\nabla \cdot \mathbf{u} - \sum_f \mathbf{S}_f \cdot \mathbf{u}_f = 0 \tag{2.27}$$

Before using the continuity equation the momentum equation can be rewritten such that it has the new velocity as result. The result is shown in Equation (2.28).

$$\mathbf{u}_p = A_p^{-1}\mathbf{H}(\mathbf{u}) - A_p^{-1}\nabla p \tag{2.28}$$

Using this last equation in the continuity equation results in Equation (2.29), which is the pressure equation of the PISO method.

$$\nabla \cdot (A_p^{-1}\nabla p) = \nabla \cdot (A_p^{-1}\mathbf{H}(\mathbf{u})) \tag{2.29}$$

Finally the two equations can be finalized by also using the discrete finite volume approximations of the pressure term in the momentum equation and the two terms in the pressure equation. The two resulting equations which are the basis of the PISO algorithm are shown in Equation (2.30) and (2.31).

$$A_p\mathbf{u}_p = \mathbf{H}(\mathbf{u}) - \sum_f \mathbf{S}_f p_f \tag{2.30}$$

$$\sum_f \mathbf{S}_f \cdot (A_p^{-1}(\nabla p)_f) = \sum_f \mathbf{S}_f \cdot (A_p^{-1}\mathbf{H}(\mathbf{u}))_f \tag{2.31}$$

Here the pressure of the current time is used in Equation 2.30 to determine the velocity at the new time. When the pressure is calculated based on the new velocities the velocity can be updated. This will result in a PISO loop. As last step the new face flux can be calculated based on the new velocity as shown in Equation (2.32).

$$\phi_f = \mathbf{S}_f \cdot \mathbf{u}_f = \mathbf{S}_f \cdot \left( (A_p^{-1}\mathbf{H}(\mathbf{u}))_f - A_p^{-1}(\nabla p)_f \right) \tag{2.32}$$

How this is implemented in OpenFOAM will be discussed at a later stage after the influence of the mesh movement has been incorporated into the Navier-Stokes equations.

## 2.3 Including moving meshes

Using the PISO loop the finite volume form of the incompressible Navier-Stokes equations can be solved. The last step is to include the mesh movement in the equation. When the mesh is moving it creates fluxes through the faces because these faces sweep through the fluid. Also the volume of the cells can change. This convective term and source term should be taken into account when dealing with moving meshes. How this is done is discussed in this section.

### 2.3.1 Arbitrary Lagrangian-Eulerian (ALE) Navier-Stokes equation

Generally fluid flows are solved using the Eulerian description as shown in the previous sections. In the Eulerian description the fluid flows through the mesh while the mesh itself is fixed. When the mesh is attached to the fluid or solid and moves with it, the method is called Lagrangian. Combining these two methods results in the Arbitrary Lagrangian-Eulerian (ALE) method ([10]). This method has proven itself in fluid-structure interaction and also in flapping flight simulations ([6] and [2]). A study ([24]) has shown that the ALE method performs best when simulating fluid problems with deforming or moving objects. The momentum equation in the ALE form is shown in Equation (2.33), where  $\mathbf{u}_m$  equals the mesh velocity. When describing a fluid in a Lagrangian framework the mesh velocity is equal to the fluid velocity, which results in the elimination of the second term. This implies that for example the mass in the control volume is constant. In the Eulerian framework the mesh velocity equals zero, which is the most common method of describing fluids. In the case where the mesh is moving the value of  $\mathbf{u}_m$  varies, resulting in the Arbitrary Lagrangian Eulerian Navier-Stokes equations. The mesh velocity is thus incorporated in the equation.

$$\frac{\partial}{\partial t} \int_{V_C} \mathbf{u} dV + \oint_{S_C} \mathbf{n} \cdot (\mathbf{u} - \mathbf{u}_m) \mathbf{u} dS - \int_{V_C} \nabla \cdot (\nu \nabla \mathbf{u}) dV = \int_{V_C} \frac{\nabla p}{\rho} dV \quad (2.33)$$

As can be seen from this equations is that an extra convective term is added. This term describes the flux created by the movement of the faces through the fluid. Also the temporal term is different. Due to the change in volume of each cell over time the derivative term cannot be place inside the integral. Instead of Equation (2.20) and (2.21) the discretisation of the temporal term is as stated in Equation (2.34) and (2.35).

$$\frac{\partial}{\partial t} \int_{V_P} \mathbf{u} dV = \frac{\mathbf{u}^{n+1} V^{n+1} - \mathbf{u}^n V^n}{\Delta t} \quad (2.34)$$

$$\frac{\partial}{\partial t} \int_{V_P} \mathbf{u} dV = \frac{\frac{3}{2} \mathbf{u}^{n+1} V^{n+1} - 2 \mathbf{u}^n V^n + \frac{1}{2} \mathbf{u}^{n-1} V^{n-1}}{\Delta t} \quad (2.35)$$

From this new equation a requirement for the convective term can be derived. This new requirement is called the Geometric Conservation Law (GCL). When a uniform

flow is considered the solution should also be uniform independent of the mesh movement. For a uniform flow Equation (2.33) becomes Equation (2.36).

$$\frac{\partial}{\partial t} \int_{V_C} dV = \oint_{S_C} \mathbf{u}_m \cdot \mathbf{n} dS = \sum_f \mathbf{u}_m \cdot \mathbf{S}_f \quad (2.36)$$

From this statement it can be concluded that the change in volume should be equal to the volume swept by the faces of the cell. When the discrete equation is considered this should also be true. In OpenFOAM this requirement is implemented for several time discretisation schemes. The volume swept by the faces is used for the convective term (based on the GCL). This is shown in Equation (2.37).

$$\oint_{S_C} \mathbf{n} \cdot (\mathbf{u} - \mathbf{u}_m) \mathbf{u} dS = \sum_f \mathbf{S}_f \cdot (\mathbf{u}_f - \mathbf{u}_{m_f}) \mathbf{u}_f = \sum_f (\phi_f - \phi_{m_f}) \mathbf{u}_f \quad (2.37)$$

Here  $\mathbf{u}_{m_f}$  is the mesh velocity at the faces and  $\phi_{m_f}$  is the mesh flux through the faces.

### 2.3.2 PISO algorithm including moving meshes

Since the influence of the mesh motion on the finite volume form of the Navier-Stokes equations is now known, it can be used to alter the PISO algorithm to incorporate the mesh motion. As can be seen the temporal term and the convective term have changed. For the temporal term only the discretisation needs to be changed, which is already incorporated automatically in OpenFOAM. For the convective term the flux used in the equations must be calculated using the fluid flux minus the mesh flux to make sure the discrete geometric conservation law (DGCL) is satisfied. In Figure A.1, shown in Appendix A, a flow diagram is given of the solver used. The darker blue blocks are needed to use moving meshes in the PISO loop.



# 3

## Mesh movement

When using the ALE form of the Navier-Stokes equation the mesh should be moved in an efficient and robust way to preserve the mesh quality. In general the movement of a certain part of the grid is known. Based on the movement of those points or body the rest of mesh should move with it. Several methods are available to perform this. In this thesis RBF mesh interpolation is used. The choice for this method is based on the studies shown in [6] and [5]. In the first section it is shortly explained why RBF mesh interpolation is a good method for the problem under consideration. Also the general description of this method is given. After this the second section is used to show how this method is implemented in OpenFOAM. Finally the mesh quality for a full clapping period is shown using two different approaches.

### 3.1 RBF mesh interpolation

Radial basis functions are well suited to interpolate the movement of a mesh based on known displacements of a set of points. As shown in [6] the RBF interpolation preserves the mesh quality well when compared to the Laplace equation with variable diffusivity ([16]) and the solid body rotation stress equation ([11]). Especially when rotating bodies are simulated the RBF interpolation provides a robust method of moving the mesh based on the body movement. In this section the use of radial basis functions in mesh movement will be explained as used in [6].

Interpolating from a set of points with known movement to the surrounding points is the main idea of RBF mesh interpolation. By summing up a set of basis functions the interpolation function is defined as shown in Equation (3.1).

$$s(\mathbf{x}) = \sum_{i=1}^{N_c} \gamma_i \phi(\|\mathbf{x} - \mathbf{x}_{c_i}\|) + q(\mathbf{x}) \quad (3.1)$$

Here  $N_c$  is the number of control points,  $\gamma_i$  are the weighting coefficients,  $\phi$  is the radial basis function with the euclidean distance  $\|\mathbf{x}\|$  as parameter,  $\mathbf{x}_{c_i}$  is the known movement of the control points and  $q$  is a polynomial. The minimal required degree of the polynomial depends on the choice of basis function ([5]). When the basis function is a conditional positive definite function a unique interpolant is given. If

these basis functions are conditionally positive definite of order  $m \leq 2$ , the order of the polynomial  $q$  can be one [3]. Since only basis functions are considered which satisfy this criterion a linear polynomial is used in the rest of the derivation. Two conditions are used to determine the weighting coefficients and the polynomial coefficients. At control points the displacement is known and thus a boundary condition is available as shown in Equation (3.2).

$$s(\mathbf{x}_{c_j}) = \Delta \mathbf{x}_{c_j} \quad (3.2)$$

Here  $\Delta \mathbf{x}_{c_j}$  are the known displacements of the control points. Together with the second requirement shown in Equation (3.3) all the coefficients can be determined ([5]).

$$\sum_{i=1}^{N_c} \gamma_i p(\mathbf{x}_{c_j}) = 0 \quad (3.3)$$

This second requirement should hold for all polynomials  $p$  with a degree less or equal than that of polynomial  $q$ .

From these two conditions a linear system of equations can be constructed which can then be solved to obtain all basis function coefficients and the four polynomial coefficients. In Equation (3.4) the set of equations to be solved are shown.

$$\begin{bmatrix} \Delta \mathbf{x}_c \\ 0 \end{bmatrix} = \begin{bmatrix} \Phi_{cc} & Q_c \\ Q_c^T & 0 \end{bmatrix} \begin{bmatrix} \gamma \\ \xi \end{bmatrix} = A\beta \quad (3.4)$$

The vector  $\beta$  consists of both the basis function coefficients  $\gamma$  and the four polynomial coefficients  $\xi$ . Matrix  $A$  consists out of the matrix  $\Phi_{cc}$  with all the basis function evaluations between the control points resulting in a size of  $N_c$  by  $N_c$  and the polynomial matrix  $Q_c$  evaluated at each control point location. The  $Q_c$  matrix has a size of  $N_c$  by 4 and is filled for each row with the following row vector  $[1 \ \mathbf{x}_{c_j}]$ . Solving this system of equations returns all the coefficients needed for the evaluation of all internal points using Equation (3.1).

For all RBF mesh interpolation calculations during this thesis the thin plate spline (TPS) is used as radial basis function. This is done based on the results from [5], which show that the TPS performs the best of the global supported radial basis functions.

## 3.2 RBF interpolation in OpenFOAM

Implementing the RBF mesh interpolation in OpenFOAM is done by storing a final evaluation matrix, such that only a matrix vector product must be calculated each time step to obtain the deformed mesh. This is possible because two-dimensional simulations are needed and the required amount of memory is available on most machines. The memory needed scales with the number of moving control points,

which is limited for two-dimensional simulations. In this section this implementation is discussed.

Starting from Equation (3.4) and combining this equation with Equation (3.1) the evaluation step can be written as a constant matrix multiplied with a vector containing the displacements of the control points. Rewriting Equation (3.4) results in Equation (3.5).

$$\begin{bmatrix} \Delta \mathbf{x}_c \\ 0 \end{bmatrix} = \begin{bmatrix} \Delta \mathbf{x}_m \\ \Delta \mathbf{x}_s \\ 0 \end{bmatrix} = \mathbf{d}_c = A\beta \Rightarrow \beta = A^{-1}\mathbf{d}_c \quad (3.5)$$

Here  $\mathbf{d}_c$  is the vector with the control points displacements and four additional zeros. These displacements can be split into moving control points ( $\Delta \mathbf{x}_m$ ) and static control points ( $\Delta \mathbf{x}_s$ ). Displacements for the static control points will always be zero, which will be used in the derivation of the smallest matrix needed to be stored. From this equation the basis function coefficients and the polynomial functions are retrieved. Instead of actually calculating the values of the coefficients this equation is substituted into Equation (3.1), resulting in Equation (3.6).

$$\begin{aligned} s(\mathbf{x}) = \Delta \mathbf{x}_i &= \sum_{j=1}^{N_c} \gamma_j \phi(\|\mathbf{x}_i - \mathbf{x}_{c_j}\|) + q(\mathbf{x}_i) \\ &= \begin{bmatrix} \Phi_{ic} & Q_i \end{bmatrix} \begin{bmatrix} \gamma \\ \xi \end{bmatrix} = B\beta = B A^{-1}\mathbf{d}_c = H \begin{bmatrix} \Delta \mathbf{x}_m \\ \Delta \mathbf{x}_s = \mathbf{0} \\ 0 \end{bmatrix} \end{aligned} \quad (3.6)$$

In this equation  $\Phi_{ic}$  is the matrix filled with basis function evaluations based on the euclidean distance between the internal points and the control points with size  $N_i$  by  $N_c$ .  $Q_i$  is the polynomial matrix of size  $N_i$  by 4. Combined these two matrices are written as a single matrix  $B$ . Substituting the definition of the coefficients from Equation (3.5) a new matrix can be constructed which is the evaluation matrix  $H$ . Its size is  $N_i$  by  $N_c + 4$ . As can be seen the vector which multiplies with the matrix  $H$  contains zeros for both the the last four rows and the static control points. The last  $N_{c_s} + 4$  columns of the matrix  $H$  are therefore not needed. Only the moving points are needed for the final evaluation once the matrix  $H$  is known. The final equation used in OpenFOAM is stated in Equation (3.7).

$$\Delta \mathbf{x}_i = H \begin{bmatrix} \Delta \mathbf{x}_m \\ \Delta \mathbf{x}_s = \mathbf{0} \\ 0 \end{bmatrix} = H_m \Delta \mathbf{x}_m \quad (3.7)$$

Where  $H_m$  is the ‘moving’ evaluation matrix of size  $N_i$  by  $N_{c_m}$ . This matrix is calculated before the simulation starts based on the initial mesh. With this matrix the new mesh can be calculated at each timestep by multiplying this matrix by the moving control point displacements relative to the initial positions.

### 3.3 Mesh quality for ‘zero-thickness’ wing

In OpenFOAM the DelFly II wing is simulated using a ‘zero-thickness’ wing. The same points in the mesh are used for both sides of the wing, with a double row of faces: one pointing towards the opposite direction of the other. The moving control points are located such that this wing is moved according to the approximate wing shape obtained from experiments and interpolation. However to incorporate the rotation of the complete wing and obtain good mesh quality a second row of moving control points are needed, which are parallel to the wing and its original control points. In this section it is shown how this influences the mesh quality.

In Figure 3.1 a small piece of the wing and the mesh with the control points is shown for both the cases (single and double row of control points). When a double

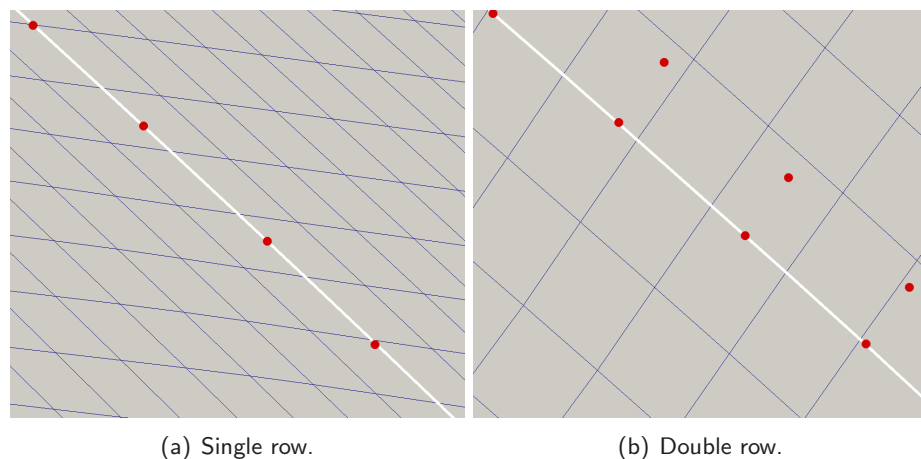


**Figure 3.1** Close up view of mesh around the wing for a single and double row of control points. Control points are illustrated with red dots.

row of control points is used the mesh stays perpendicular to the local gradient of the wing (the white line in Figure 3.1), while the single row of control points only translates the mesh. To capture the rotation of the wing a double row of control points is needed. As a consequence the mesh quality of the two different approaches is significantly different. In Figure 3.2 the mesh quality is shown for both cases by calculating the maximum skewness and non-orthogonality. It can clearly be seen that the double row of control points is needed to ensure a good mesh quality throughout the complete flapping cycle, while a single row of control points does not provide sufficient quality in terms of non-orthogonality. The definition of skewness is shown in Figure 3.3(a) and for non-orthogonality Figure 3.3(b) illustrates the definition of the non-orthogonality parameter. Skewness is defined as the ratio between the length of  $m$  and  $d$  shown in Figure 3.3(a). It is a measure on how much the face centre is displaced from the line connecting the two cell centres ( $\alpha_N$ ). In

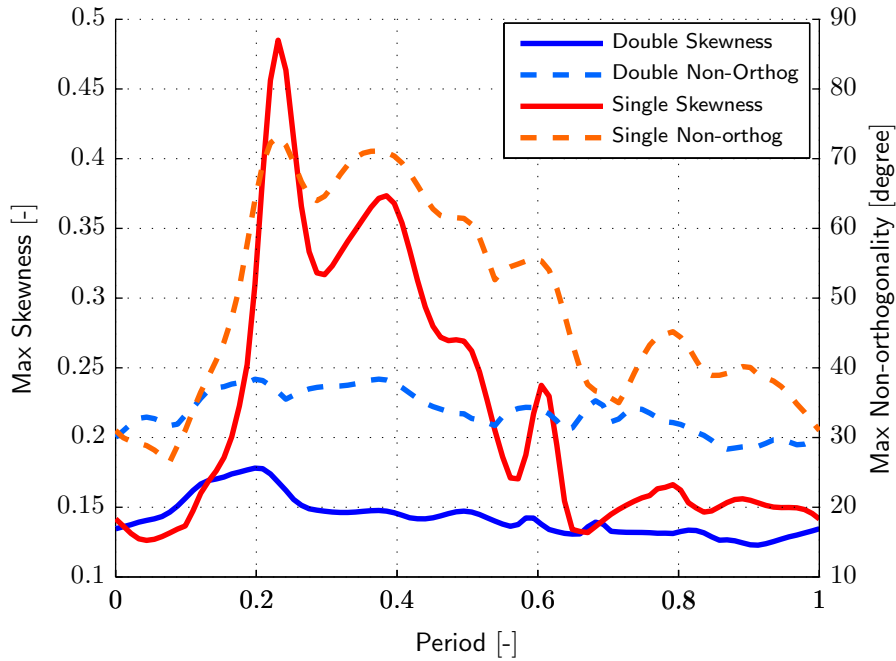


**Figure 3.2** Mesh quality in terms of skewness and non-orthogonality for a single and double row of control points.

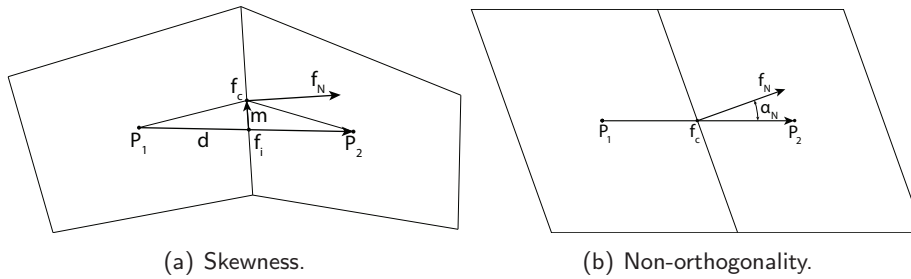


**Figure 3.3** Illustrations of mesh quality definitions for both the mesh skewness and non-orthogonality.

an ideal cell there is no skewness and the face centre is located on this line. Non-orthogonality is the angle between the face normal and the line connecting the two cell centres. Minimizing the truncation error on the diffusion term requires a low non-orthogonality, while a low skewness is desired to ensure that the interpolation from the cell centres to the face centre is accurate ([6]).



# 4

## Wing kinematics

In Particle Image Velocimetry (PIV) experiments on the DelFly II wings, the wing motion and deformation are measured by means of images [14]. This is done for several span-wise locations. From these results the chord wise wing kinematics at 71% of the span (including the deformation) can be retrieved for specific points in time. Based on these shapes a spline interpolation is made in space and a Fourier series interpolation is made in time to approximate the kinematics during a full flapping cycle. The experimental set-up is shown in Figure 4.1. Two dimensional

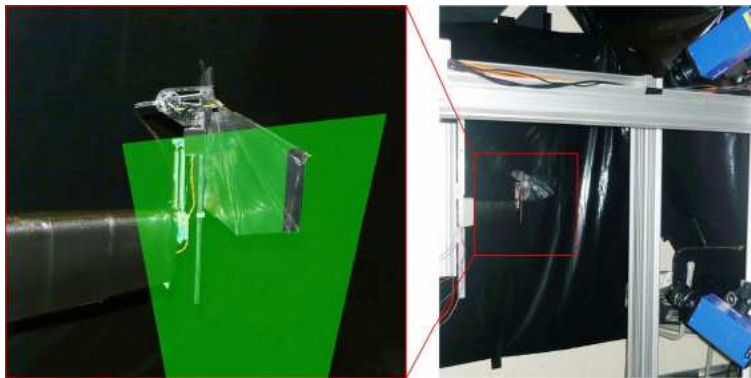


**Figure 4.1** DelFly II PIV experimental set-up used by [14].

wing profiles at a fixed span position are obtained using this set-up. Since no rigid wings are tested an equivalent rigid wing is derived from the deforming wing kinematics. To further investigate the influence of flexibility two extra wings are derived from the rigid and DelFly wing. All the kinematics and derivations are explained in this chapter together with the kinematics used in the validation for the immersed symmetry plane methods.

### 4.1 DelFly II wing kinematics

From the experiments images of the chord-wise deforming wing shapes are available for specific points in time. First splines are used to create a continuous function of the shapes in space for each specific point in time. By taking a set of discrete

points along the wing, interpolation in time can be performed using Fourier series interpolation for each individual point and its coordinates. Both the steps will be explained in the following paragraphs.

### 4.1.1 Wing shape approximation in space

From experiments chord-wise wing shapes are obtained by using a phase-locked PIV set-up [14]. Phase-locked PIV is used to ensure that the laser sheet is perpendicular to the wing at each point in the cycle. As a consequence the shapes for different moments during the flapping cycle are not recorded in the same instantaneous flapping cycle. However when periodic deformation of the wing is assumed this method is valid, because the shape recorded at a fixed time in the period will always be the same. In Figure 4.2 the final results including the spline interpolation can be found for both the clap and peel motion. These shapes are the result of manually

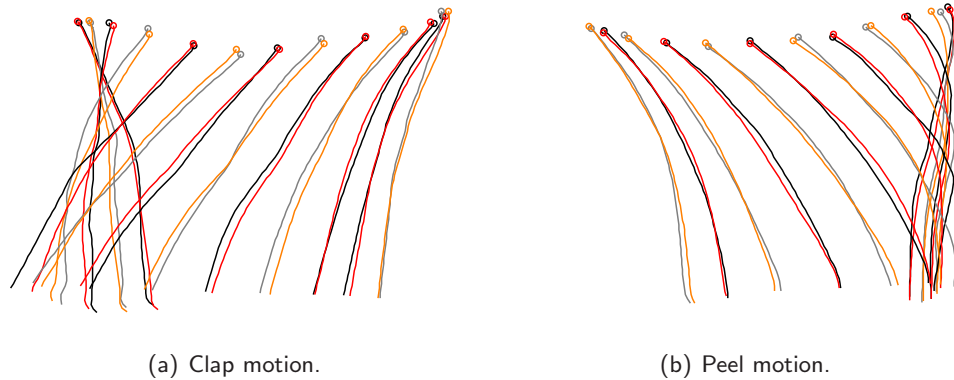


**Figure 4.2** DelFly II chord-wise deforming wing shapes at 71 % of the chord from experiments [14] in black and grey. Resulting wing shapes after Fourier series interpolation are shown in red and orange.

drawing a spline describing the wing shape in each PIV image obtained during the experiment. In Figure 4.3 such an image and its spline are shown. In this figure two wings are present because the image is taken during the clap phase, while at the largest part of the flapping cycle the right wing is not captured. Thus only the left wing is used, because the light sheet is not perpendicular to the right wing and the right wing is not captured through the whole flapping period. It should be mentioned that the shape is upside-down, because the leading edge (small curved part) is at the bottom. Doing this for all 50 images the shape is approximated in space at specific points in time by means of a continuous function. For CFD simulations the wing shape should be known at all simulation times. Interpolation in time is needed to get an approximate wing shape at all simulation times.

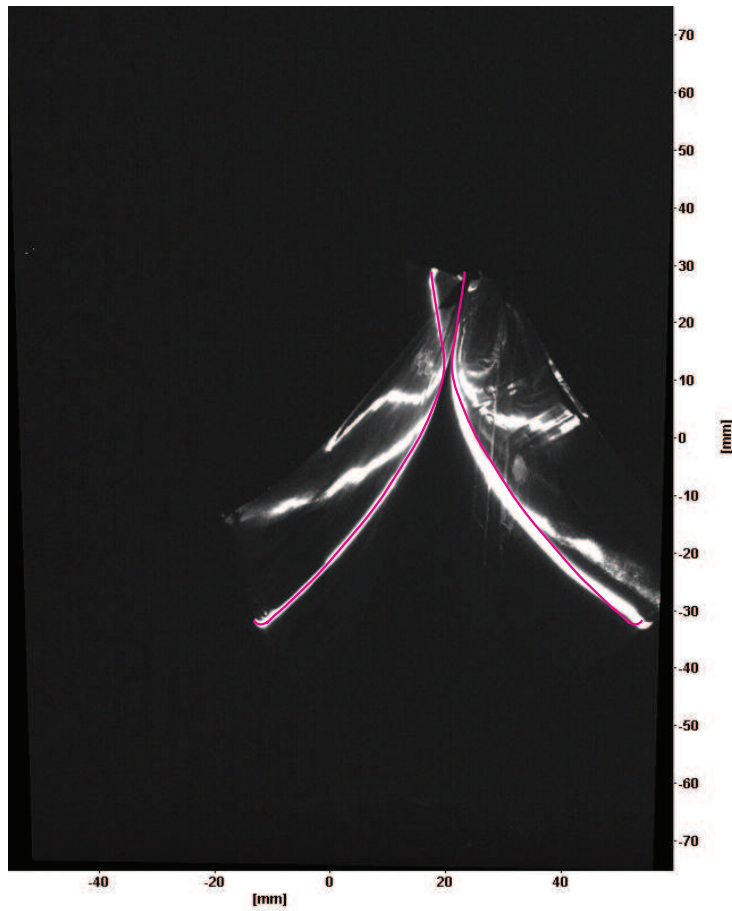


**Figure 4.3** PIV image of the DelFly II wing at 71 % of the span together with the spline interpolation.

#### 4.1.2 Interpolating the wing shape in time

Fourier series interpolation is used to approximate the wing shape in time based on the 50 splines obtained from the interpolation in space. Fourier series interpolation needs discrete points in time to be used as the function to be approximated. The spline is evaluated at a fixed number of points for each of the 50 splines. For each of these points both the x-coordinate and y-coordinate are approximated in time by means of a separate Fourier series. In all CFD simulations 60 points, uniformly distributed along the wing, in space are used for the Fourier series interpolation. This results in a total of 120 Fourier series interpolations per coordinate (60 of the spline points and 60 additional to incorporate rotation in the mesh deformation). There is only one parameter which controls the Fourier series interpolation, which is the number of modes used to approximate the function in time. Fourier series interpolation does not fit through the given points, which leads to a

measurable error in the approximation. When more modes are used in the Fourier series interpolation a smaller error is present in this approximation. However as will be shown in the next section choosing the maximum number of Fourier modes will obscure the results due to excessive accelerations. In Figure 4.4 the error against the number of modes used is shown. As expected both the 2-norm and the maximum

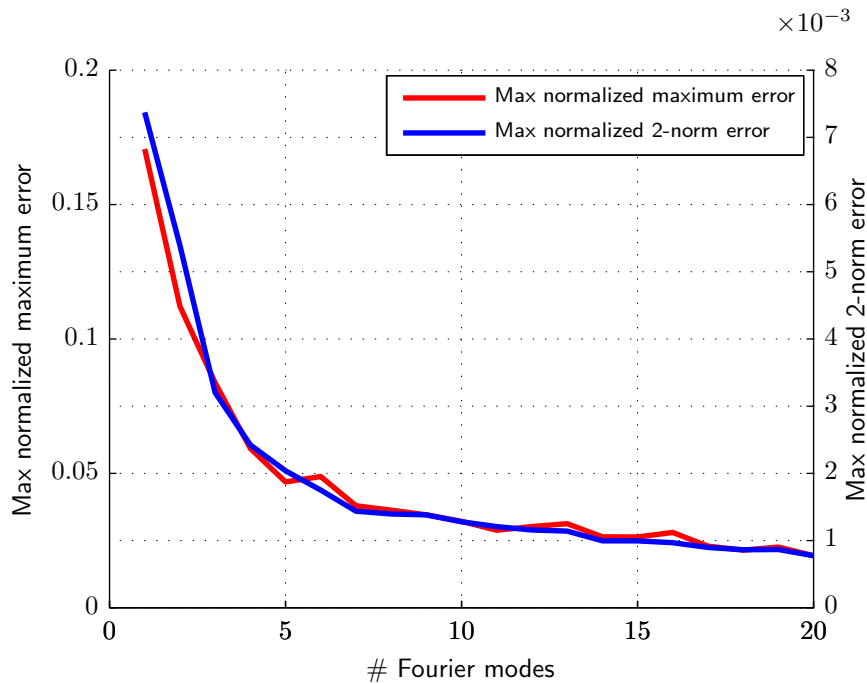


**Figure 4.4** Position error against number of Fourier modes used for interpolation.

error drop when more modes are used. It can also be seen that the graph flattens out, such that using more than 7 modes does not provide a significant decrease in error any more. Besides the position error also the acceleration of the wing is of great importance in incompressible aerodynamics. In Figure 4.5 the acceleration of the leading edge based on the Fourier series interpolation can be seen for a full flapping cycle using different number of modes for interpolation. From this it can be seen that the dominating frequency in the acceleration equals the highest Fourier mode used for the interpolation. Higher frequencies in the acceleration do reflect back in the forces due to the time derivative of the velocity at the wing in the momentum equations. A trade-off should be made because fast oscillations in the acceleration disturb the force profile during a flapping cycle, which is undesirable.

### 4.1.3 Motion characteristics

Based on the DelFly wing motion obtained via the experimental data, characteristics variables can be determined describing this motion. The characteristic velocity, stroke length, chord length, frequency, Reynolds number and Strouhal number are

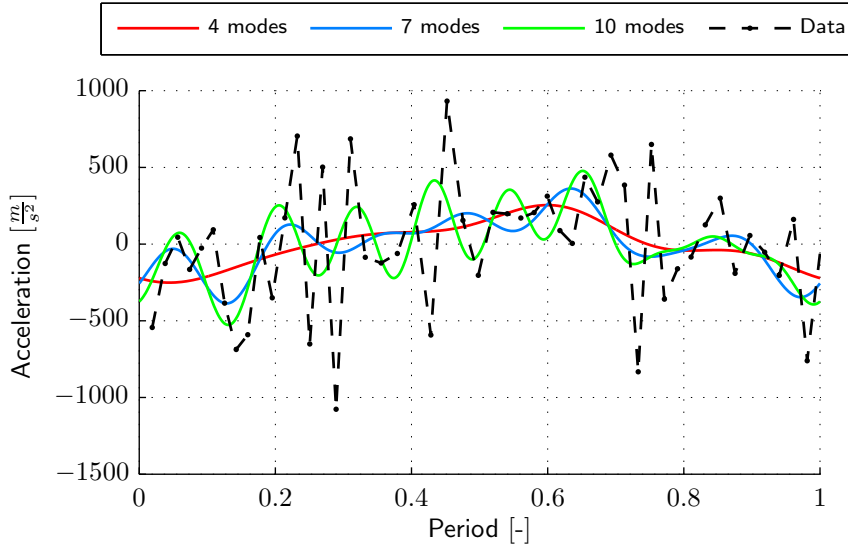


**Figure 4.5** Acceleration of leading edge during a complete flapping cycle for several Fourier modes.

**Table 4.1** Motion characteristics

Variable name	Symbol	Value	Units
Frequency	$f$	11	Hz
Chord length	$c$	7.4	cm
Stroke length	$L_{ref}$	8.0	cm
Characteristic velocity	$U_{ref}$	1.76	m/s
Reynolds number	$Re$	9641	-
Strouhal number	$St$	0.5	-

the variables describing this motion. The choice or derivation of these variables will be stated in this paragraph and their values are summarised in Table 4.1. The frequency, chord length and stroke length can directly be obtained from the PIV images or the experimental set-up. During the experiment a flapping frequency of 11 Hz is used. At 71 % of the span the chord length is equal to 7.4 cm. To determine the stroke length the PIV images are used and the movement of the leading edge is tracked to derived the value. From the experimental data a stroke length of 8 cm is derived. In hovering conditions there is no free-stream velocity and thus the characteristic (or reference) velocity is determined differently. Based on the stroke length and the frequency this value is derived. An average wing velocity is calculated

based on the stroke length and the frequency. This is shown in Equation (4.1).

$$U_{ref} = 2L_{ref}f \quad (4.1)$$

$$Re = \frac{U_{ref}L_{ref}}{\nu} = \frac{2f(L_{ref})^2}{\nu} \quad (4.2)$$

$$St = \frac{fL_{ref}}{U_{ref}} = \frac{fL_{ref}}{2L_{ref}f} = \frac{1}{2} \quad (4.3)$$

Based on the characteristic length (stroke length) and the characteristic velocity the Reynolds number and Strouhal number can be calculated for this problem based on Equation (4.2) and (4.3). Doing so results in a Reynolds number of 9641 and a Strouhal number of 0.5.

## 4.2 Influence of Fourier modes on forces

The number of Fourier modes used for interpolation has a strong influence on the acceleration, which reflects in the force profile of flapping cycle. It is important to separate the influence of the interpolation on the forces, which is undesired, and the influence of the movement of the wing on the forces, which is desired. Looking at the force profile for different number of Fourier modes, see Figure 4.6, a first estimate of the influence of the interpolation can be made. Using higher modes for

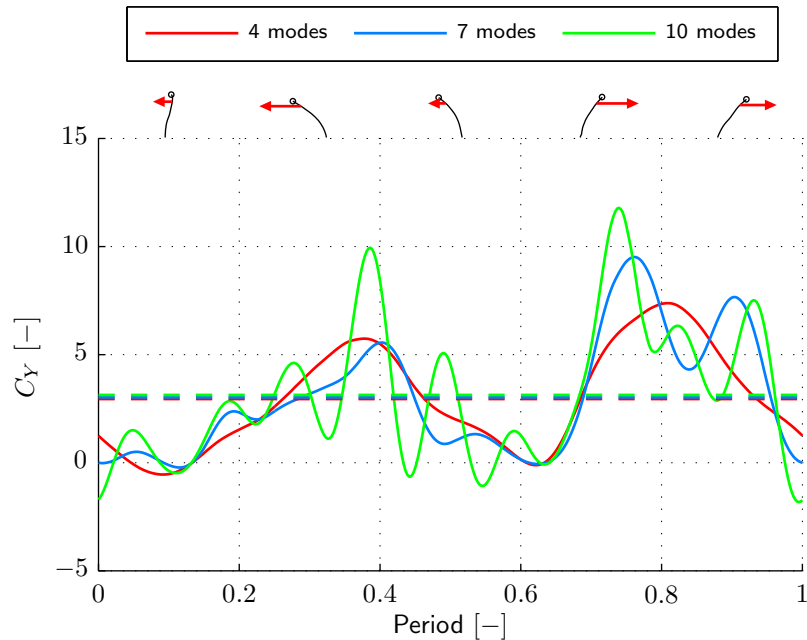


**Figure 4.6** Upward force coefficient for a complete flapping cycle for different number of Fourier modes.

interpolation will directly reflect in the dominating frequency in the forces. This is

related to the acceleration of the wing. Two aspects should be taken into account to determine what is desirable in these simulations and how many Fourier modes should be used.

Firstly, the wing shapes from the experiments are not obtained by averaging, but by taking a single snap shot in different periods for each shape. Due to the chaotic aerodynamics (both found in simulations and experiments) also the shape of the wing is chaotic in time. However, this is not used in the simulation, because only a single shape per specific time is obtained during the experiments. Obtaining an accurate approximation of a DelFly II wing in time does not necessarily need a very small position error due to this chaotic behaviour in experiments. The only requirement is that the approximated wing is closely related to the DelFly II wing. Secondly there is a direct relation between the acceleration of the wing and the pressure around the wing. Including higher frequencies will directly influence the forces as can be seen in Figure 4.6. Large pressure fluctuations occur, because there is no damping effect from the fluid (incompressible flow) and the wing (enforced shape). In reality the wing is very flexible and will deform according to the fluid. However since no structure model is taken into account now the wing shape is forced into the fluid causing a more direct impact on the forces.

From these two aspects it can be concluded that using higher Fourier modes does not help in determining the influence of flexibility. Higher modes will only enforce higher frequency acceleration forced onto the fluid without any damping in the simulation. This is undesirable. The shapes obtained from the experiments are recorded with some measurement error (in the order of 2 %). More important is the assumption that the wing shape is periodic. As will be shown in Chapter 6 and what is observed during the experiments is that the aerodynamics are not periodic. Consequently the wing deformation is not periodic, while this is assumed when using phase-locked PIV. Due to this there is no need to interpolate the shape at high precision. In Figure 4.6 it can be seen that the amplitude of the high frequency oscillations for the 7 and 10 modes curve is equal or higher than the amplitude of the general force (4 modes). Therefore four Fourier modes are chosen as a good trade-off between sufficient accurately modelling a DelFly II like deforming wing and at the same time reducing the frequency and amplitude of the acceleration.

### 4.3 Equivalent rigid wings

Besides the deforming wing shapes obtained from the experiments also a rigid wing is used in the simulations. This is done to determine the influence of this deformation. Based on the movement of the leading and trailing edge of the deforming wing the rigid wing is constructed.

### 4.3.1 Purely translating rigid wing

The movement of the wing induced by the driving mechanism of the DelFly II is a translational movement, without pitching. Due to the flexibility of the wing it is passively pitching during the flapping cycle. However when the wing would be rigid this pitching movement would not be present. Generating this equivalent rigid wing is straight forward. The movement of the leading edge is the same as for the flexible wing and the length is constant. The direction is vertical which causes a 90 degrees angle of attack. In Figure 4.7 both this equivalent translational wing and the flexible wing profile can be found for several time instances during an out-stroke. However this wing would generate no upward force, due to the lack of surface in

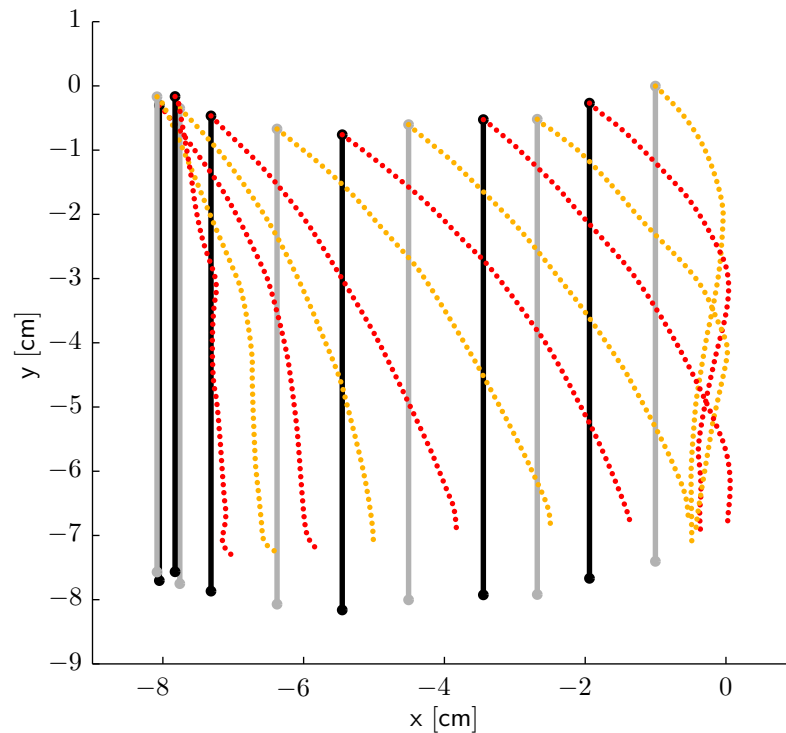


**Figure 4.7** Flexible and equivalent translational wing.

horizontal direction. Therefore this wing is not used for simulation, but to show what the direct consequence would be if the flexible wing is replaced by a rigid wing on the DelFly II. An equivalent rigid wing is derived from the flexible wing shape to determine the influence of the deforming DelFly II wing on the aerodynamics compared to a rigid wing. The derivation of this equivalent rigid wing is found in the next paragraph.

### 4.3.2 Equivalent rigid pitching wing

Besides translation the rigid wing can also perform a rotating movement. To achieve this in reality the wing must be actively pitched during the flapping cycle by the driving mechanism. Based on the angle between the leading edge and the trailing edge of the deforming wing the pitch angle in time is determined.

The leading edge motion of the rigid wing is equal to that of the flexible wing. Drawing a line from the leading edge to the trailing edge of the flexible wing gives the direction which is used as pitch angle. With these two parameters (leading edge location and pitching angle in time) and the constant wing length (7.4 cm) the equivalent rigid wing can be modelled during the complete flapping period. In Figure 4.8 both the flexible and the equivalent rigid wing are shown for different moments in time during the out-stroke. The symmetry plane is located at 0.425

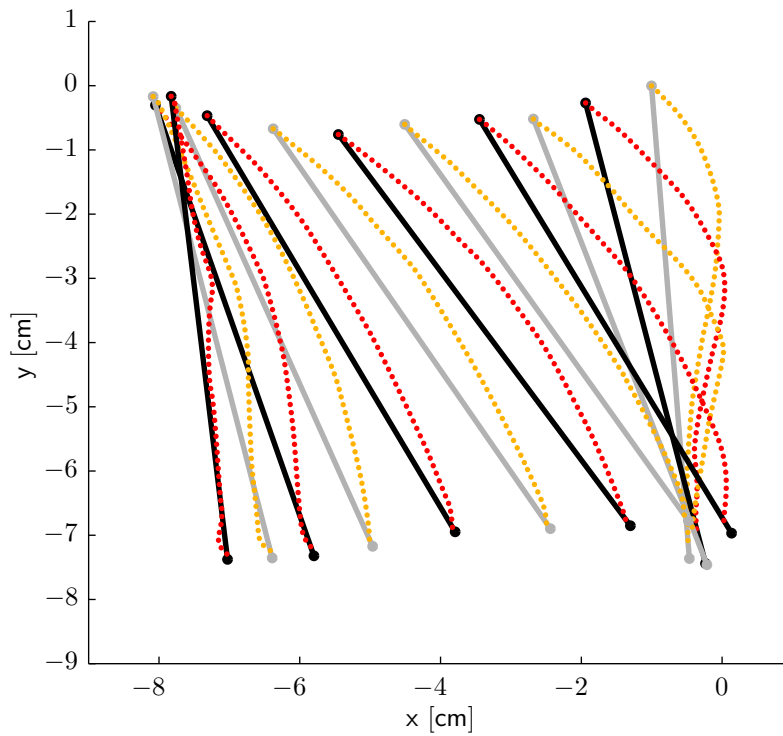


**Figure 4.8** Flexible and equivalent rigid pitching wing.

cm causing an minimum gap for the deforming wing equal to 3.5 % of the chord between the wing and the symmetry plane. The equivalent rigid wing will not move through the symmetry plane during its motion.

## 4.4 Semi-flexible and super flexible wings

In an attempt to further investigate the influence of deformation in the flexible wings, two extra wings are created based on the deforming DelFly II wing. A semi-flexible wing (see Figure 4.9), which in terms of deformation is in between the rigid and the DelFly II wing, and a super-flexible wing (see Figure 4.10), which is more flexible than the DelFly II wing.

To derive these wings a two step approach is taken. First the shape is determined via a linear movement of points, on the wing, over the line from the rigid to the flexible DelFly wing shape. Secondly and lastly the length is adjusted such that it is equal to the DelFly II chord length. In this last step the whole shape is scaled such that the amount of deformation remains as derived in the first step. In Equation (4.4) and (4.5) the two steps are shown in mathematical form. These two equations are applied to all points on the wing.

$$\mathbf{x}_{flex}^* = \mathbf{x}_{rigid} + A_{flex} \underbrace{(\mathbf{x}_{DelFly} - \mathbf{x}_{rigid})}_{\text{Flex direction}} \quad (4.4)$$

$$\mathbf{x}_{flex} = \mathbf{x}_{flex}^* + \underbrace{\left(1 + \frac{L_{DelFly} - L_{flex}^*}{L_{flex}^*}\right)}_{\text{Length multiplier}} \underbrace{(\mathbf{x}_{flex}^* - \mathbf{x}_{LE})}_{\text{Scale direction}} \quad (4.5)$$

Where  $\mathbf{x}_{flex}^*$  is the non-scaled new flexible wing point position,  $\mathbf{x}_{rigid}$  is the rigid wing point position,  $A_{flex}$  is the flex parameter,  $\mathbf{x}_{DelFly}$  is the DelFly II wing point position,  $\mathbf{x}_{flex}$  is the scaled new flexible wing point position,  $L_{DelFly}$  is the length of the DelFly wing,  $L_{flex}^*$  is the length of the non-scaled new flexible wing position and  $\mathbf{x}_{LE}$  is the leading edge position, which is equal for all wings. All parameters but one are determined by the DelFly wing and rigid wing. The flex parameter must be chosen and determines the amount of deformation/flexibility. If the flex parameter is equal to zero the rigid wing is obtained, while at a value of 1.0 the DelFly wing is found. For the semi-flexible wing a value of 0.5 is chosen, while for the super-flexible wing the flex parameter is set to 1.5. In Figure 4.9 the semi-flexible wing shape at 24 % of the flapping cycle is shown together with the rigid, DelFly and non-scaled new flexible wing. In this figure the black lines show the 'Flex direction', which is the vector from the rigid wing point to the DelFly wing point. For the super-flexible wing a similar plot can be found in Figure 4.10.

## 4.5 Miller-Peskin rigid wing

For validation of the immersed symmetry plane the motion described in [25] is used. In this study an immersed boundary method is tested on low Reynolds numbers for two typical motions also seen in the DelFly II. First only a fling half-stroke is simulated, after which also a single 'clap-and-fling' motion is performed. Both these

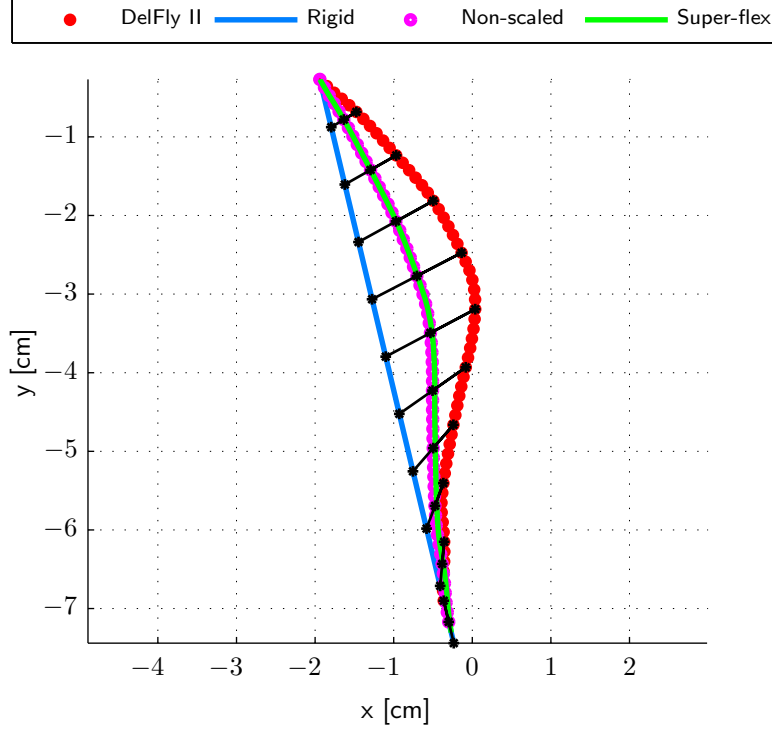


**Figure 4.9** Semi-flexible wing based on the DelFly II wing and the equivalent rigid wing.

motion are simulated at a Reynolds numbers of 128.

Harmonic and linear functions are used to generate the movement based on translational and rotational velocities. This ensures a continuous function in terms of acceleration, which is needed in the simulations. The equation describing the motion in [25] are rewritten in terms of translational and angular position, such that they can be used in the mesh movement algorithm. In Figure 4.11 the translational movement and rotation of the Miller-Peskin fling half-stroke wing can be found. The translational position is normalised by the chord length and the rotational position by the maximum deflection angle. The movement is described using the following phases: translational acceleration, constant velocity, rotational phase and constant angle phase. Each of these phases are described by equations below. In Equation (4.6) the position during the translational acceleration phase is described.

$$x = 0.5V \left( \tau + \sin \left( \pi + \pi \frac{\tau - \tau_{acc}}{\Delta\tau_{acc}} \right) \frac{\Delta\tau_{acc}}{\pi} \right) + c_1 \quad (4.6)$$

Here  $V$  is the maximum translation velocity in the complete movement,  $\tau$  is the normalized time ranging from 0 to 1 for a single period,  $\tau_{acc}$  is the time the acceleration starts,  $\Delta\tau_{acc}$  is the length of the acceleration and  $c_1$  is the integration constant which varies based on the start position and the moment of acceleration. For con-

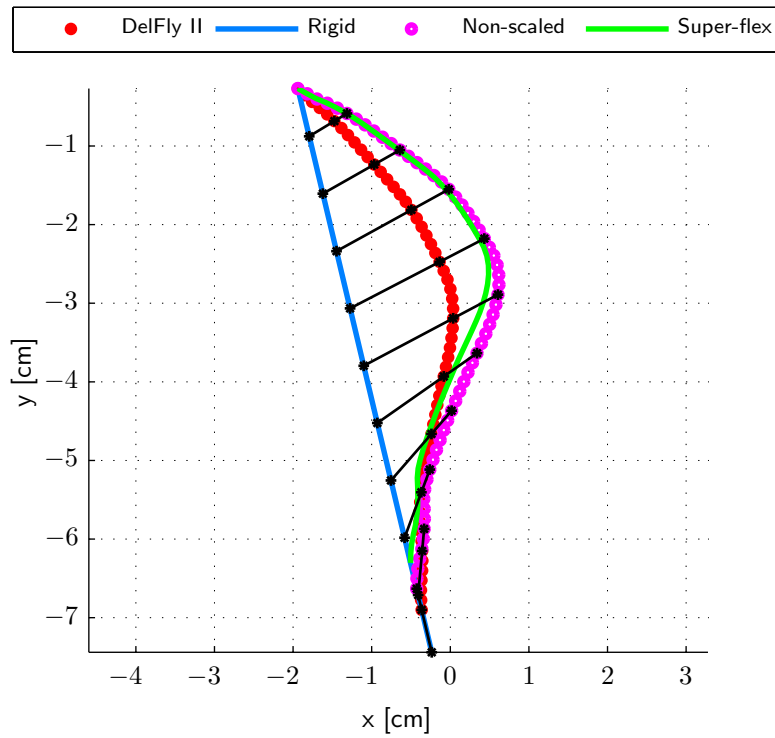


Figure 4.10 Super-flexible wing based on the DelFly II wing and the equivalent rigid wing.

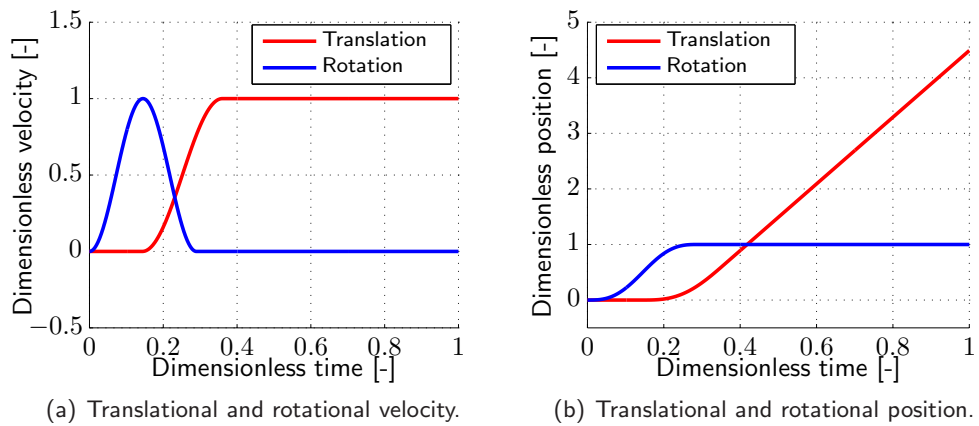


Figure 4.11 Miller-Peskin fling half-stroke kinematics from [25] in terms of velocity and position.

stant speed a simple linear function is used with the slope equal to  $V$ . Lastly the rotation is described with a function for the angle between the wing vertical axis. In Equation (4.7) the function for the angle during the rotational phase is found.

$$\alpha = 0.5\omega_{rot} \left( \tau - \sin \left( 2\pi \frac{\tau - \tau_{rot}}{\Delta\tau_{rot}} \right) \frac{\Delta\tau_{rot}}{2\pi} \right) + b_1 \quad (4.7)$$

Here  $\omega_{rot} = 2\Delta\alpha/\Delta\tau_{rot}$ , where  $\Delta\alpha$  is the angular amplitude of the motion. Similar to the translation acceleration and deceleration phases, the rotational phase uses two time values to describe the moment of rotation ( $\tau_{rot}$ ) and the length of rotation ( $\Delta\tau_{rot}$ ).

In Table 4.2 the parameters used to describe this rigid wing motion are stated. For validation the highest Reynolds number tested in [25] is used, which corresponds to 128. Besides the fling half-stroke motion also a single 'clap-and-fling' motion is

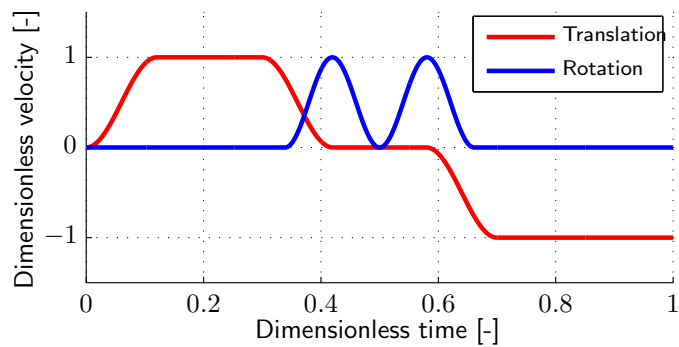
**Table 4.2** Parameters for the Miller-Peskin fling half-stroke motion

Variable	Value	Units
Chord	5.0	cm
Maximum Velocity	0.06	m/s
End time	6	s
$\Delta\alpha$	45	degrees
$\tau_{acc}$	0.1433	-
$\Delta\tau_{acc}$	0.2167	-
$\Delta\tau_{rot}$	0.29	-
$\tau_{rot}$	0	-
$\nu$	$2.3438 \cdot 10^{-5}$	$\text{m}^2/\text{s}$

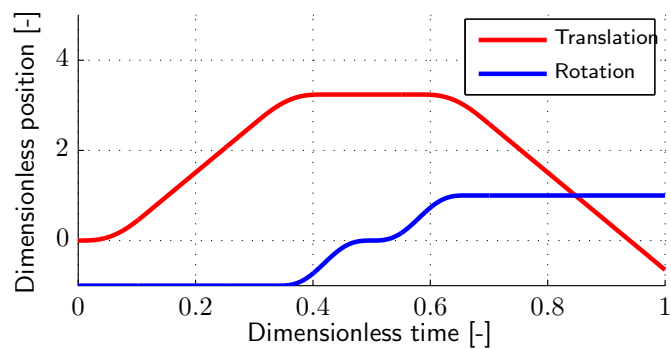
simulated in [25]. The same equations can be used as for the fling half-stroke. For translational deceleration a minus sign should be added to Equation (4.6) and the value of  $c_1$  will change based on the location of the wing prior to the deceleration phase. In Figure 4.12 the velocities and positions in time can be found. The first part of the movement is the clap phase. Initially the wing has an angle of -45 degrees and accelerates immediately to the maximum velocity. At the end of the clap phase the wing decelerates and rotates around the leading edge such that the trailing edges are clapping together. For the fling phase the same motion as shown in Figure 4.11 is used. To generate this motion the parameters stated in Table 4.3 are used.

**Table 4.3** Parameters for the Miller-Peskin clap-and-fling motion

Variable	Value	Units
Chord	5.0	cm
Maximum Velocity	0.06	m/s
End time	9	s
$\Delta\alpha$	45	degrees
$\tau_{acc}$	0.0796296	-
$\tau_{dec}$	0.0796296	-
$\Delta\tau_{acc}$	0.12037	-
$\Delta\tau_{dec}$	0.12037	-
$\Delta\tau_{rot}$	0.161111	-
$\tau_{rot}$	0	-
$\nu$	$2.3438 \cdot 10^{-5}$	$\text{m}^2/\text{s}$



(a) Translational and rotational velocity.



(b) Translational and rotational position.

**Figure 4.12** Miller-Peskin 'clap-and-fling' kinematics from [25] in terms of velocity and position.

# 5

## Methods to simulate 'clap-and-peel'

To simulate the 'clap-and-peel' motion a symmetry plane is used. Because the gap between the two wings (or in this case between the wing and the symmetry plane) is small (in the order of 1% of the chord) the ALE approach with RBF mesh interpolation is not feasible. This approach fails because the cells between the wing and the symmetry plane will have to vary a lot in size to simulate the movement. Two other methods are proposed to simulate the symmetry plane as an immersed boundary. RBF mesh interpolation is still used to move the mesh in a smooth way and another method is used to enforce the symmetry boundary conditions in the domain. Firstly a method which deforms the mesh near the immersed symmetry plane is used. The mesh is deformed such that the symmetry boundary can be constructed implicitly in the discrete equations. The second method is an immersed boundary method (IBM) which enforces the boundary conditions explicitly by interpolation. Both methods will be explained in this chapter.

### 5.1 Changing mesh topology

To enforce the symmetry boundary conditions on the correct location a mesh boundary must be present there, while the RBF mesh interpolation must still be used to ensure the mesh quality. Combining the immersed symmetry plane with an additional mesh movement near the symmetry plane to create a real boundary a new method is developed during this thesis. In this method cells near the symmetry plane are deformed to create a real boundary of faces where the symmetry conditions can be enforced. In this way the boundary conditions are taken into account in the discretisation and solved for implicitly, while the ALE approach with RBF mesh interpolation is still used to ensure a smooth deforming mesh. In this section the details of this new method are explained.

#### 5.1.1 Method description

The basis of this new method is still the ALE method. Every time step the complete mesh is moved based on the control points to get a smoothly deforming mesh. After this the new method is applied to enforce the symmetry plane conditions at

the correct location. The new method uses five steps to enforce these symmetry conditions at the correct location. First the symmetry plane is updated. This is done by recreating the mesh without symmetry plane at  $t^n$  after which the RBF mesh interpolation can be performed to obtain the mesh at  $t^{n+1}$ . In this new mesh the symmetry plane faces are identified and the symmetry plane is created by moving these faces to the correct location ( $t_{sym}^{n+1}$ ). In the second step the old mesh is updated to ensure that the discrete geometric conservation law (DGCL) is satisfied. By splitting the mesh at the symmetry plane in the third step the boundary conditions (symmetry conditions) can be applied implicitly. As a fourth step interpolation, based on the previous symmetry plane velocity and pressure values, is used to redefine the old values of pressure and velocity at the symmetry plane. Finally the fluid is solved with the symmetry conditions enforced at the correct location.

In Figure 5.1 the mesh moving and deforming steps are shown. In these figures the vertical red line is the immersed symmetry plane, green stroked cell centres indicate the first fluid cells next to the symmetry plane, red stroked cell centres indicate the first non-physical cells next to the symmetry plane, black dots represent other cell centres, pink dots represent face points used to construct the symmetry plane and blue faces are moved to construct the symmetry plane. In the coming paragraphs each figure will be explained in detail.

### Move symmetry plane faces

After the mesh at  $t^n$  is recreated from  $t_{sym}^n$  and is moved to the new location for this time step by using the RBF mesh interpolation (see Figure 5.1.(a) to Figure 5.1.(c)) the fluid cells (cells in the non-grey area) can be identified. The faces between the fluid and non-physical cells are known after this step, which are the blue faces in Figure 5.1.(c). These faces will be used to construct the new symmetry plane. Once the faces are identified each of these face is moved such that they are exactly at the symmetry plane with the correct orientation, see Figure 5.1.(d). An additional algorithm is present during this step to ensure that no zero or negative volume cells are created. At the end of this step the new mesh has two rows of deformed cells with their shared faces forming a boundary at the immersed symmetry plane location.

### Redefining the old mesh

As will be explained in paragraph 5.1.2 the mesh must be moved back to its previous location to recalculate the cell volumes and the mesh fluxes. All points are moved back except for the points associated with the faces at the symmetry plane. These points will not be moved. In this way the old mesh is updated with new values for the old cell volumes, which are shown in Figure 5.1.(e). When the old volumes and

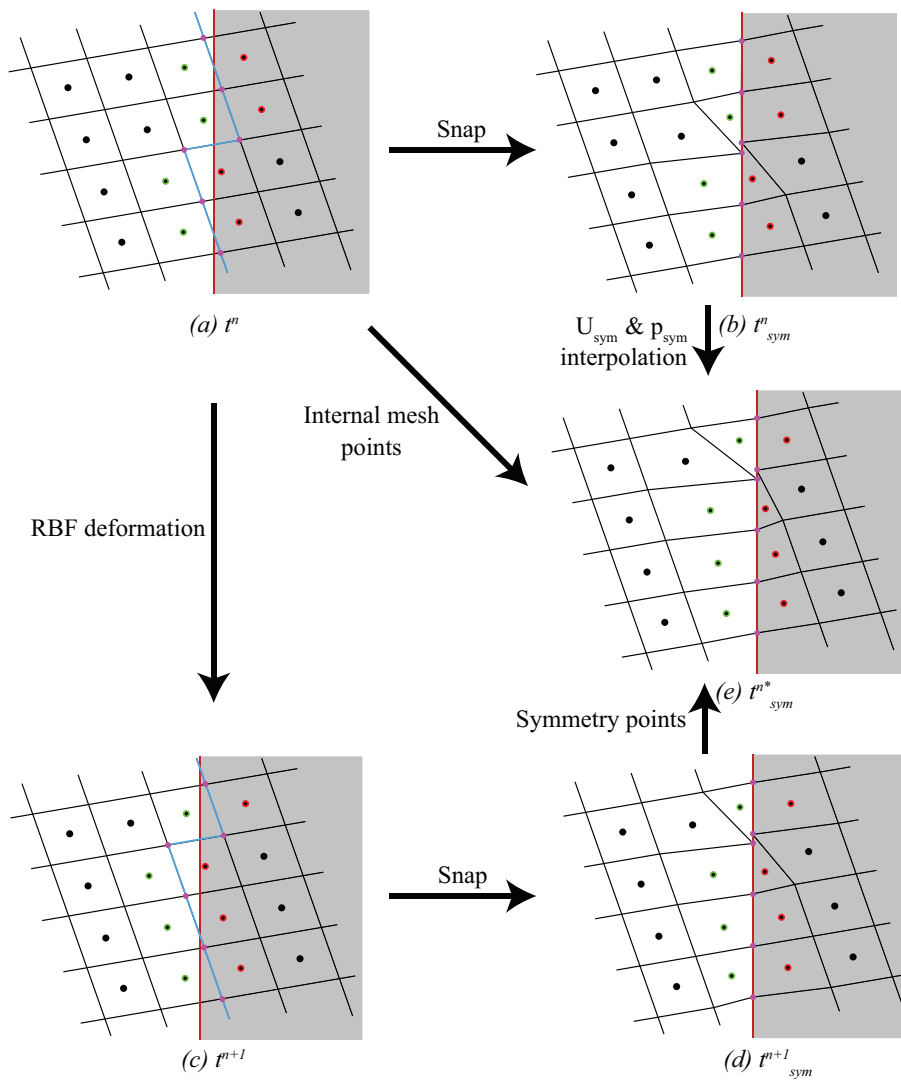


**Figure 5.1** Steps taken to alter the meshes to obtain mesh with faces at the symmetry plane boundary.

old mesh fluxes are updated the mesh is moved to its new location, which has been calculated in the previous step (from Figure 5.1.(e) to Figure 5.1.(d)).

### Split the mesh at symmetry plane

Now the mesh has a row of faces at the symmetry plane the mesh can be split at that location. After the mesh is split the correct boundary conditions can be enforced on these faces. For the pressure and the tangential velocity component a zero-gradient condition is applied, while the normal velocity is set to zero at the symmetry plane.

Now the new mesh topology is known it can be used in OpenFOAM to construct the matrices for solving the momentum equation and the Laplace equation for the pressure.

### **Interpolating at symmetry plane**

Every time step the mesh is stitched and split. Due to this the initial values at the symmetry plane faces at the new time are set to zero automatically by OpenFOAM. By means of a linear interpolation from the face values at the end of the previous time to the new locations of the cell at the current time, the initial pressure and velocity values are set. For the normal component of the velocity this is not needed, since this will be zero at all times. After this interpolation all field variables from the previous time are transferred to the new mesh as initial value. However cells from the non-physical domain do enter the fluid domain due to the mesh movement. These cells have zero velocity and zero pressure as old value. When these values are not changed a large value for the temporal term will be found, which will disturb the pressure field and thus the forces. To reduce these disturbances a second interpolation is performed for the initial (and old) values of the new fluid cells. Based on the surrounding fluid cells and the symmetry plane face values the initial (and old) pressure and velocity values for the new fluid cells entered from the non-physical domain are interpolated using a simple linear weighting.

### **Solving the fluid equations**

Matrices can now be created using the new mesh and its boundary conditions. Due to the direct enforcing of the symmetry plane boundary conditions in the matrix at the correct location, these conditions will be satisfied. A standard PISO loop is performed with one additional step: setting all non-physical cells to zero solution prior to solving the system of equations. This is done for both the velocity in the momentum equation and the pressure in the Laplace equation. In this way only the equations for the fluid cells are solved, which reduces the size of the matrices.

#### **5.1.2 Changes in the DGCL**

As mentioned above the old mesh is updated at the beginning of a each new time step. This is done to calculate the actual volume change and mesh fluxes felt by the fluid. At the symmetry plane (which is not moving) mesh fluxes will be present, since the mesh is first moved with RBF mesh interpolation and after this the faces are moved to the symmetry plane. OpenFOAM recognizes this as actual mesh fluxes, while in theory the symmetry plane faces are not moving and thus no mesh fluxes are present. To ensure a correct implementation of the DGCL the old mesh is updated with the symmetry plane faces at the same location as at the current

time. In this way the mesh fluxes at the symmetry plane are zero. Based on the updated old mesh ( $t_{sym}^{n*}$ ) and the new mesh ( $t_{sym}^{n+1}$ ) the actual mesh fluxes can be calculated and also the corresponding change in cell volumes are calculated. These values are then used to correct the fluid fluxes and to calculate the temporal term, which includes the change in cell volumes.

When the old mesh is updated (at  $t_{sym}^{n*}$ ) the values for the pressure and velocity remain the same even though the volume changes. Looking at the general discrete form of the conservation laws, as stated in Equation (5.1), it can be seen that if the volume changes, but the values remain unchanged, conservation for momentum may not be preserved.

$$\sum_i \phi_i V_i^{t^{n*}} \neq \sum_i \phi_i V_i^{t^n} \quad (5.1)$$

However for the mass conservation the equation is still satisfied, since the density is the same in the whole field and the total volume remains constant as well. However for the momentum conservation small deviations are present due to the change in volume and the non constant field for the pressure and velocity. This might influence the solution. Most important is the conservation of mass, because otherwise stable calculations will be difficult. Determining the influence of the discrepancy in the momentum conservation does not fit in the scope of this thesis.

Lastly the calculation of the DGCL depends on the temporal discretisation scheme as seen in Chapter 2. However only a single old volume is known and thus only a first order discretisation scheme can be used in this method.

### 5.1.3 Overview of method

In Figure A.2 an overview is given of the solver including the PISO loop. All steps discussed in the previous sections are shown in a flow diagram together with the standard PISO loop. Appendix A also shows the charts of the standard solver and the immersed symmetry plane method with explicit interpolation.

## 5.2 Immersed symmetry plane (ISP) method

Initially a simpler method had been developed, which did not need extra mesh deformation steps. An immersed symmetry plane is used to impose the symmetry conditions on the flow. The basis of the immersed symmetry plane method is interpolating the boundary conditions present on this immersed boundary onto the surrounding cells. Each time step this is done explicitly. For interpolation the weighted non-linear least squares (WNLLS) method is used. Several steps are taken to interpolate the symmetry conditions from the symmetry plane to the surrounding cells. First the cells cut by the symmetry plane, their neighbours in the fluid and

the faces in between these two cells are identified. Next the velocities in the non-physical domain are set to zero, while the immersed boundary cells (cells between the non-physical and physical domain) are set to an interpolated value based on the WNLLS interpolation between the surrounding cell values and the symmetry conditions. After the velocity field is determined the fluxes through the faces near the symmetry plane are corrected to ensure mass conservation. For the pressure equation the non-physical domain is set to zero pressure solution, while after the pressure equation is solved for the pressure is corrected at the symmetry plane to incorporate the boundary conditions. This step is executed iteratively to ensure a convergence in the boundary conditions. Except for the first step all steps are performed several times within a single time step to ensure the conditions are imposed, while the fluid is solved. This is the consequence of the explicitness of this method. In this section each step is explained more extensively.

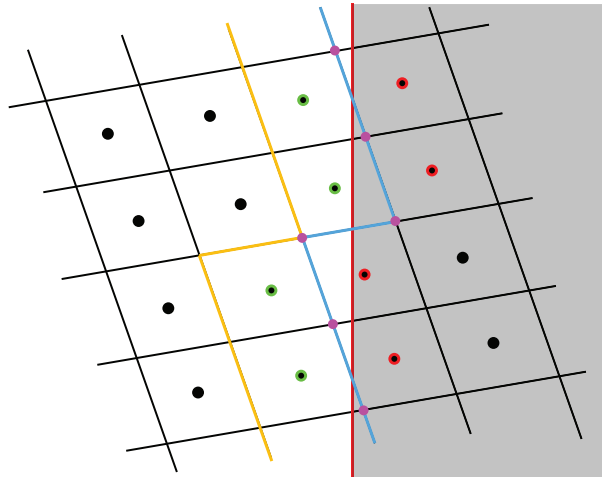


**Figure 5.2** Overview of mesh for explicitly enforcing the symmetry conditions at the immersed symmetry plane.

### 5.2.1 Cell and face identification

In Figure 5.2 the identified cells and faces are shown. The green dots show the immersed boundary cells, which separate the fluid (physical) domain from the non-physical domain. All cells to the right of the red cells and the red cells itself are part of the non-physical domain. Faces used for the flux correction are displayed in yellow, while the faces between the two domains are shown in blue.

### 5.2.2 Set velocity values at boundary and solve the momentum equation

After the previous step the values at the immersed boundary cells are interpolated based on the symmetry conditions at the immersed symmetry plane and the surrounding cell values from the previous velocity field solution. For this interpolation the weighted non-linear least squares (WNLSS) is used with a two dimensional polynomial of second order. For the tangential velocity the derivative in normal direction of the symmetry plane is taken such that the zero-gradient boundary condition can be incorporated. To incorporate the zero normal velocity condition at the symmetry plane in the interpolation the normal WNLLS function is used. At the immersed boundary cells the values are set as boundary conditions prior to solving the momentum equation for the velocity. Besides the interpolation of the value itself, the temporal term for the immersed boundary cells is set to zero, because the value is set as fixed value boundary condition.

### 5.2.3 Correct fluxes

Based on the velocities solved in the previous step the fluxes through the faces close to the immersed symmetry plane are corrected for conservation of mass. The total flux over these faces is calculated. The total flux over the immersed symmetry plane should be equal to zero. Weighted by the percentage of contribution to the total flux the magnitude of the total flux is subtracted from the faces. In this way it is ensured that the sum of fluxes over these faces is equal to zero. This correction is needed to ensure that the conservation of mass is satisfied.

### 5.2.4 Solve pressure equation and correct for symmetry conditions

Opposed to the momentum equation, the pressure equation is solved with only the solution in the non-physical domain set to zero. Also the faces for which the flux correction is applied are set to zero gradient faces. With these two conditions the pressure equation is solved after which the solution is corrected by interpolating the symmetry conditions from the immersed symmetry plane to the immersed boundary cells. Again the WNLLS is applied by using the symmetry conditions and the surrounding field values. As done for the tangential velocity the derivative in the normal direction of the symmetry plane is used to incorporate the zero-gradient condition for the pressure at the symmetry plane. This complete step is repeated several times to ensure that the interpolated values at the immersed boundary cells converge. However due to the interpolation of the conditions and the assumptions made the boundary conditions will not be imposed correctly. Faces near the symmetry plane will have a zero pressure gradient, while this should be at the symmetry plane, and the immersed boundary cells will have a zero time derivative value for the velocity. Also the interpolation function (WNLLS) does not ensure correct symmetry conditions when the cell centre is on top of the symmetry plane. This

method provides a relative simple method without mesh topology changing algorithms. However these assumptions and approximations of the conditions should be taken into account when analysing the results.

### 5.2.5 Iterations within a single time step

Besides the standard PISO loop an extra loop is present because of the explicit nature of this method. Both the symmetry conditions for the pressure and the velocity are implemented explicitly and therefore this extra loop is needed. The number of iterations of this final loop is specified by the user and should be chosen such that there is a certain amount of convergence in the interpolated values at the immersed boundary cells. In Figure A.3, shown in Appendix A, the schematic overview of this method is given.

# 6

## Chaotic flow behaviour

Due to the hovering flight conditions shed vortices remain near the wing. Circulation patterns in the flow transports vortices back to the wing several periods later causing the flow dynamics to change (see Figure 6.1). Also leading and trailing edge vortices remain near the wing, since there is no global convecting flow in the domain (zero free-stream velocity). Because the frequency of interaction of these 'old' vortices with the wing is not equal to the flapping frequency the flow dynamics change each period. As a consequence the measured flow dynamics are chaotic. This can both be seen in the pressure and velocity fields and the forces derived from them. In this

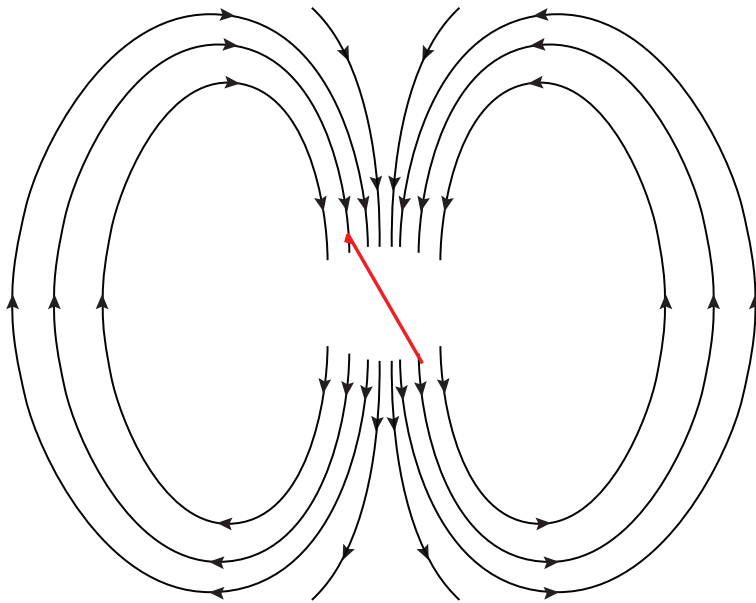


**Figure 6.1** Illustration of the global circulatory flow pattern around the wing for hovering flight.

chapter it is shown that the hovering condition is causing this chaotic behaviour. Also a method using the Lyapunov exponent will be used to determine the rate of instability. Finally it is shown that a change in every parameter of the simulation will cause a different instantaneous force profile and corresponding flow.

## 6.1 Quantifying chaotic flow

To quantify the level of chaos in this problem the Lyapunov exponent is used as measure of instability of chaotic growth. In [19] the fundamentals of this Lyapunov exponent are explained. This exponent describes the rate of growth between two simulations with only a small difference at their initial conditions. Due to the chaotic problem this small difference will grow exponentially until the order of the solution itself is reached. The first exponential part is where the Lyapunov exponent describes the rate of growth. In Figure 6.2 the example from [19] is given. In the

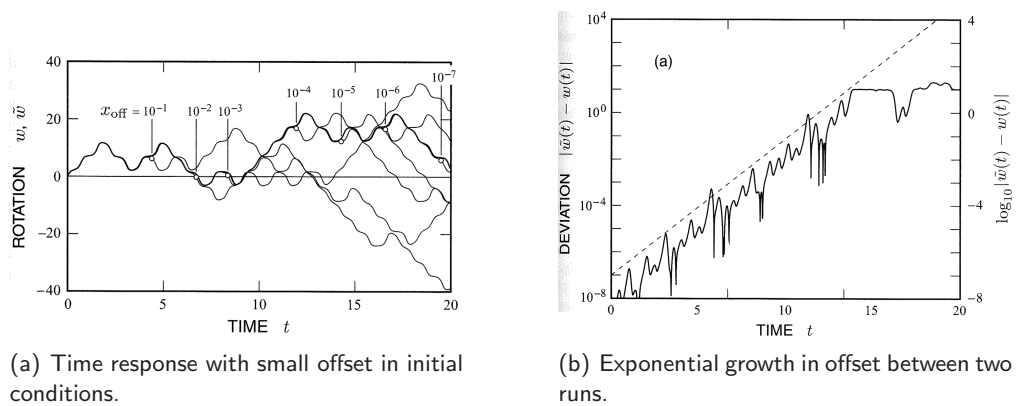


**Figure 6.2** Example from [19] illustrating the Lyapunov exponent in the results of Lorenz simulations with different initial conditions.

time response (see Figure 6.2(a)) the results are shown for a set of initial conditions based on a small offset to the original initial condition. All of them eventually depart and the rate of growth from this small offset value to a difference in the order of the system itself is called the Lyapunov exponent. In Figure 6.2(b) this rate of growth is indicated as the dashed line. Here it can be seen that a difference in the order of  $10^{-8}$  grows within 20 seconds to a difference in the order of the response itself (around  $10^1$ ). In Equation (6.1) the approximate formula for the initial growth is given.

$$|\tilde{w}(t) - w(t)| \approx C e^{\lambda t} \quad (6.1)$$

In this equation  $\tilde{w}(t)$  is the time response for the perturbed system (with a small offset in the initial conditions),  $w(t)$  is the time response of the original system,  $C$  is the constant indicating the initial difference between the two systems and  $\lambda$  is the Lyapunov exponent indicating the rate of exponential growth.

Several methods have been developed to accurately find the Lyapunov exponent from a single time series as shown in [28]. However in this thesis the Lyapunov exponent is merely used to indicate that parameters, which normally hardly influence the results, will now cause a difference in results in the order of the system itself due to this exponential growth. By comparing two simulations with slightly different settings for certain parameters (linear solver, number of processors used, tolerance

and initial velocity) the rate of growth can be found and thus the instability of the system can be determined by means of the Lyapunov exponent.

## 6.2 Periodic solution with free-stream velocity

No periodic solution is found for the simulations with hovering conditions. This is due to the absence of a global convective flow in the domain. By enforcing a certain free-stream velocity through the domain the vortices should be convected away from the wing before they can interact with it. As a consequence the flow topology will change and the wing is not simulated in hovering conditions any more. However this would indicate that the chaotic flow behaviour is caused by the interaction between shed leading and trailing edge vortices with the wing due to the circulatory flow pattern.

To determine which free-stream velocity is needed to create a periodic flow several simulations are performed increasing this free-stream velocity each time. To show that the flow is periodic a phase diagram is used. In Figure 6.3 the phase diagrams are shown for a free-stream velocity of 2 m/s and 3 m/s. When compared to Figure 6.4, which shows the result for hovering conditions, it is clear that the flow is chaotic without free-stream velocity and becomes periodic when adding a flow through the domain. Also a free-stream velocity of 1 m/s has been simulated, but did not result in a periodic flow. Therefore 2 m/s is considered to be the minimum free-stream velocity needed to obtain periodic flow. Both in Figure 6.3 and 6.4

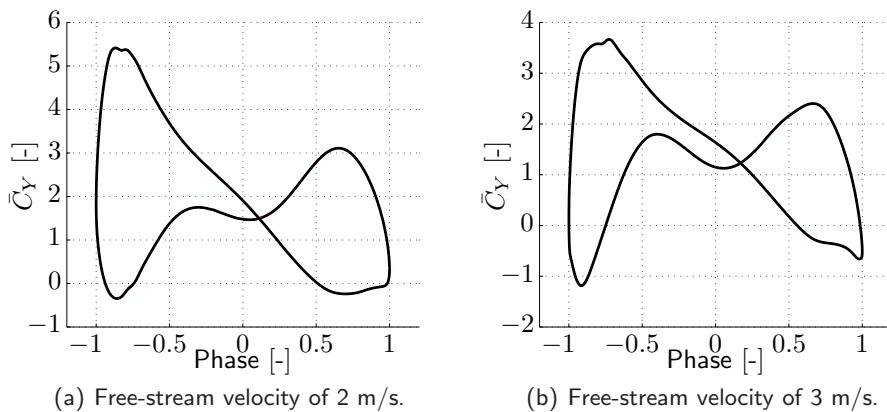


**Figure 6.3** Phase diagrams for different free-stream velocities.

the thick black line is the result of the last simulated period and the red line is the result of other periods before the last one. From these results it is clear that adding a global convective flow to the domain will create a periodic solution, since the red line is barely visible. This indicates that the circulatory flow is one of the phenom-

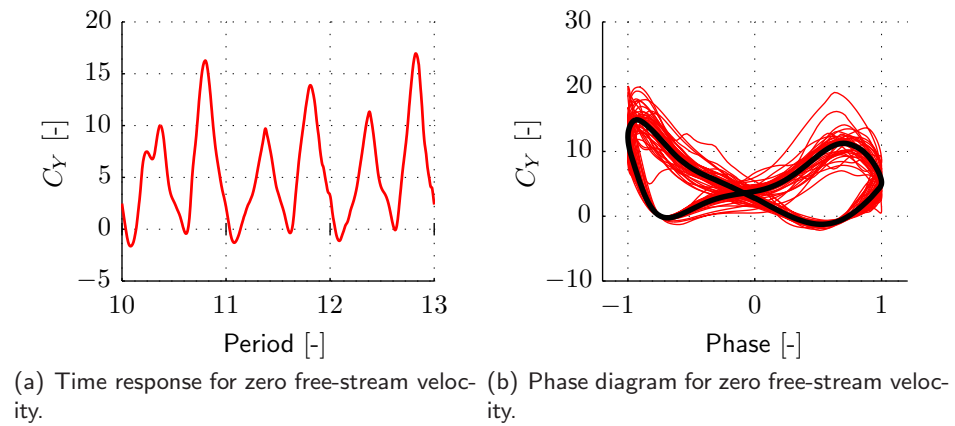


**Figure 6.4** Phase diagrams and time response for zero free-stream velocity.

ena that creates the chaotic behaviour in the flow and thus results in a sensitive problem to all simulation parameters.

### 6.3 Determining the order of instability

Due to this chaotic behaviour every difference in the simulation can cause a difference in results in the order of the results itself due to the exponential growth. To show this and to determine the rate of growth (Lyapunov exponent) several simulations are performed using slightly different settings. This is done for both the hovering conditions and the free-stream velocity causing a periodic flow. The following parameters are used for these simulations.

- Tolerance: standard  $10^{-7}$  is used a tolerance. For the 'perturbed' a tolerance of  $10^{-8}$  is used.
- Number of processors: standard 4 processors are used. For the 'perturbed' simulation 6 processors are used.
- Initial velocity: standard zero velocity is used as initial value. For the 'perturbed' simulation an initial negative y velocity of  $10^{-6} m/s$  is used.
- Linear solver: standard the Algebraic Multi-Grid (AMG) solver is used. For the 'perturbed' simulation the Preconditioned Conjugate Gradient (PCG) solver is used.

By varying each of these parameters a small offset is generated in the flow field near the order of the tolerance ( $10^{-7}$ ). This difference can also be seen in the upward force on the wing. This force is used to indicate the initial difference and

the growth of this difference between the original and the perturbed simulations. In the following sections each of these parameters and there resulting exponential growth is discussed.

### 6.3.1 Tolerance

By changing the tolerance from  $10^{-7}$  to  $10^{-8}$  for the pressure equation a difference in the order of  $10^{-7}$  is created. This is also reflected in the upward force on the wing as shown in Figure 6.5. The initial difference is in the order of  $10^{-7}$  and it

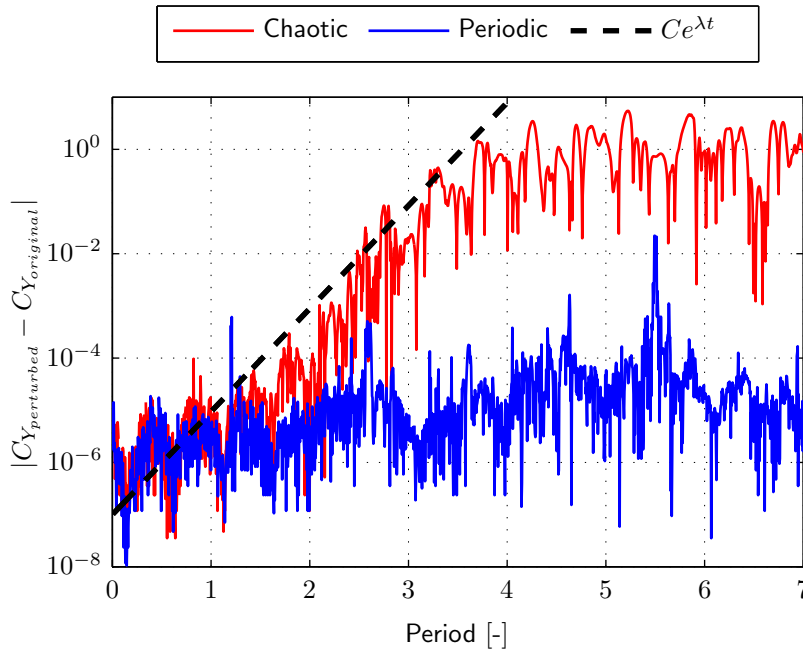


**Figure 6.5** Difference in upward force coefficient between the original and 'perturbed' simulation with a difference in tolerance for the pressure equation.

indeed grows approximately exponential to a difference in the order of  $10^0$  to  $10^1$ . By approximating the initial growth with Equation (6.1) the Lyapunov exponent can be determined. The dashed line shows the exponential function with  $\lambda$  equal to 50. From this it can be concluded that for the hovering conditions the Lyapunov exponent equals 50 indicating that a difference in the order  $10^{-7}$  will become significant in the results within 4 periods (0.36 seconds). For the periodic case the difference remains near the order equal to the tolerance as expected.

### 6.3.2 Parallel computing

In OpenFOAM parallel computations solves blocks of the complete matrix and iterates at the processors boundaries. The tolerance of the computation is still met, only the actual value of the residual depends on the number of processors and how the domain is split into several sub-domains. By using 6 instead of 4 processors the exponential growth of this system can be computed. In Figure 6.6 the result of this simulation is shown. The same order of instability is found as for the tolerance case:

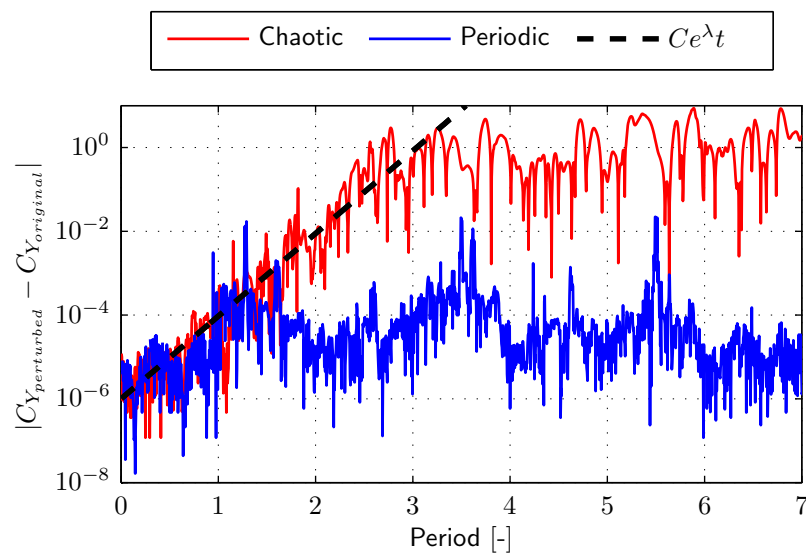


**Figure 6.6** Difference in upward force coefficient between the original and 'perturbed' simulation with a difference in the number of processors used.

$\lambda$  is equal to 50. Also the initial difference for the upward force coefficient is of the same order ( $10^{-6}$ ). For the periodic solution the difference does not grow towards a larger value, but remains near the initial difference.

### 6.3.3 Initial conditions

A third option is to change the initial conditions slightly. In this case the vertical velocity in the domain is set to  $-10^{-6} m/s$  instead of zero. Based on the previous two runs exponential growth is expected. The result is shown in Figure 6.7 and indeed again exponential growth is present. Also here the slope of the exponential growth is equal to 50 and the periodic solution does not grow in time. This small perturbation at the start of the computation changes the instantaneous response within 4 periods in the order of the solution itself.

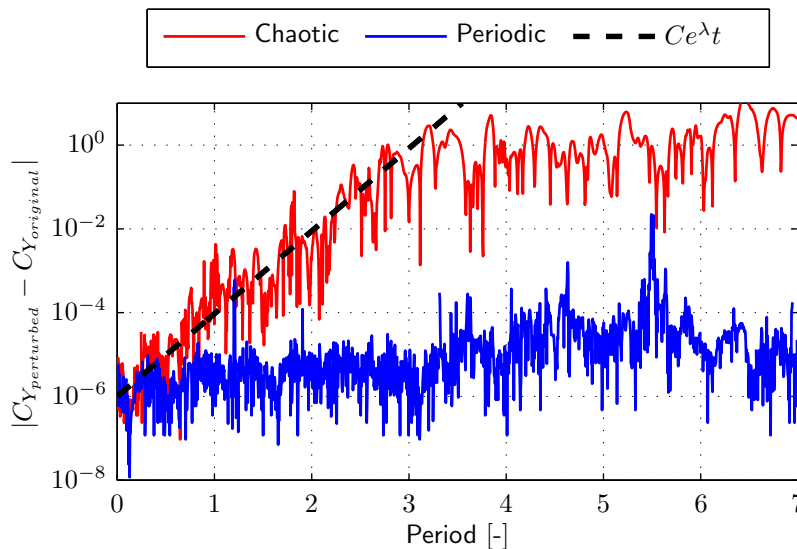


**Figure 6.7** Difference in upward force coefficient between the original and 'perturbed' simulation with a difference in the initial velocity.

### 6.3.4 Linear solver

Finally the linear solver is changed. Even though both the solvers solve until the same tolerance is achieved, the actual field values do differ from each other in the same order as the tolerance. This is due to the different method used to solve the matrix, which results in a slightly different result. In Figure 6.8 the result can be found. As expected a small difference is present at the first time step, which is near the order of the tolerance. Exponential growth causes this small difference to grow to bigger difference in the order of  $10^0$ . The slope of this growth is again 50, while the periodic solution does not grow in time.

## 6.4 Coping with 'periodic chaos'

From these four simulation it can be seen that the instantaneous solutions do differ significantly from each other once one parameter is changed in the simulation. Even the linear solver and the number of processors used have a major influence due to the exponential growth. It is also clear that the circulatory flow pattern, together with the vortices which remain near the leading edge after shedding, are responsible for this chaotic behaviour. Since imposing a global convective flow (free-stream velocity) through the domain eliminates this exponential growth. However the study is focused on the influence of flexibility in hovering conditions. A way to filter out

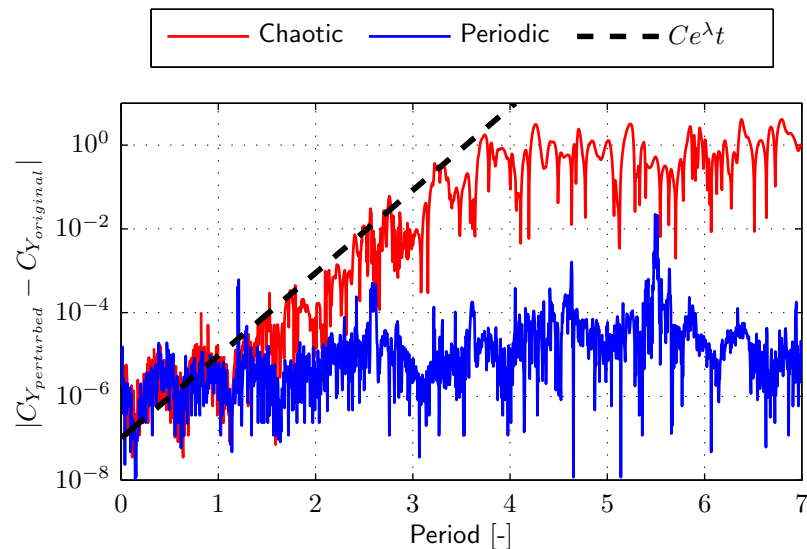
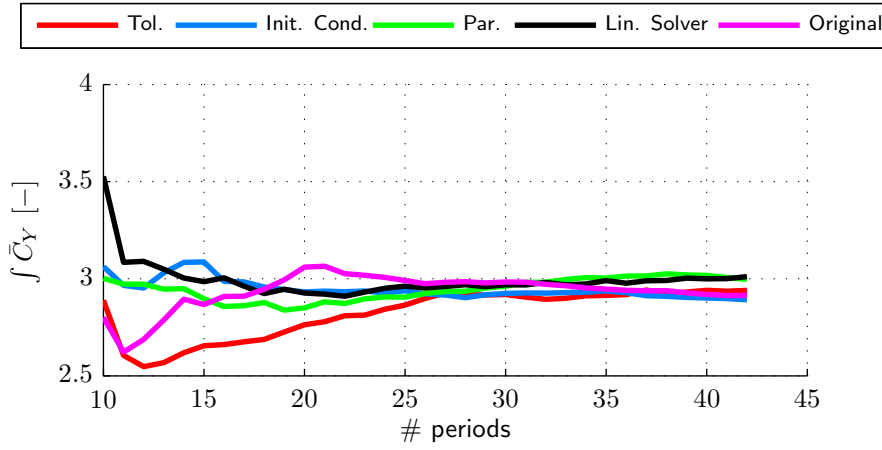


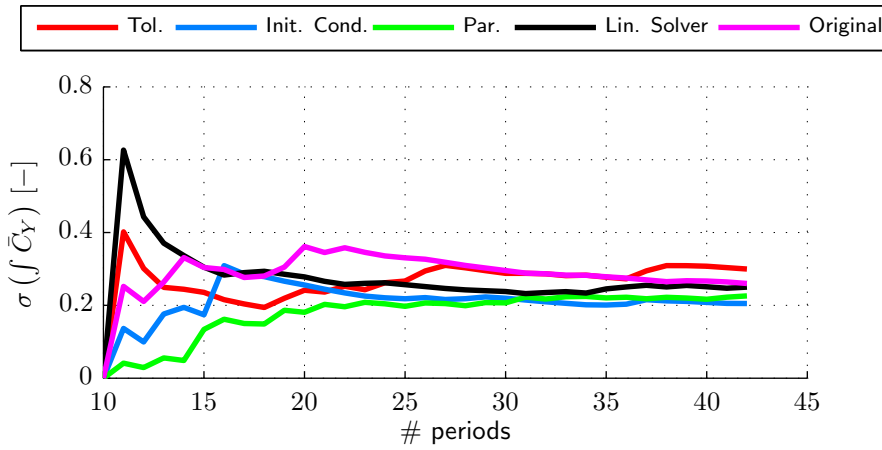
**Figure 6.8** Difference in upward force coefficient between the original and 'perturbed' simulation with a difference in linear solver.

the period to period variation is to calculate a periodic average based on a large number of periods. The statistical parameters, such as the average and standard deviation, can be calculated from the simulation data. Based on the convergence of these variables the number of periods required is estimated. When this is done for the simulations discussed in the previous section, Figure 6.9 is the resulting convergence of the average and the standard deviation. It can be seen that the average does converge when more periods are used for the average. In this case a total of 43 periods are simulated and the first 10 are not used for the calculation of the average to eliminate the start up vortices from the average. If 43 periods are simulated this should provide a converged average and standard variation. However there is still a difference in the averages between the results obtained with different parameters. Since the same physical problem is solved it can be expected that eventually the difference between the average will become smaller if more periods are used. This is however not feasible when considering calculation times. The maximum number of periods will be set to 44 to have sufficient data to average over and obtain a certain level of convergence for the different simulations (see also mesh study results in Chapter 7). More periods will increase the simulation time even further, which will limit the amount of work which can be done in this thesis.

The next step is to determine what a significant difference between results is based on Figure 6.9. In Table 6.1 the differences between the original and the four simulations with altered settings are shown. Based on these results it can be said that a difference between results lower than 4 % is not significant since this difference could also be achieved by altering the solver settings. This knowledge will be used in the mesh and



(a) Convergence of integrated periodic average.



(b) Convergence of standard deviation.

**Figure 6.9** Convergence of statistical parameters for the integrated periodic average for the 5 simulations.

**Table 6.1** Parameters for the Miller-Peskin fling half-stroke motion

Simulation	Integrated periodic average $C_Y$	Difference [%]
Original	2.91	-
Tolerance	2.94	0.90
Initial Cond.	2.89	0.76
Parallel	3.00	2.84
Linear solver	3.01	3.33

Courant number study and the results analysis. For the interpretation of the final results considering the influence of flexibility this is also an important parameter. As an additional tool the simulations with a free-stream value creating a periodic solution can be used to help in determining the required mesh density and maximum Courant number.

# 7

## Mesh study and time step

It is important to determine the mesh resolution which is needed to accurately capture the force variation within a period. Also the maximum Courant number is determined in this study. Both these short studies will be discussed in this chapter. Since the aerodynamics are chaotic the mesh study is performed using both a periodic flow (by using a free-stream flow through the domain) and the chaotic flow (with hovering boundary conditions). The goal is to find the least dense mesh and largest Courant number, which still provides reliable results to be used in determining the influence of flexibility.

### 7.1 Mesh study

For the periodic flow a free-stream velocity of  $3\text{ m/s}$  is used. In Chapter 6 it has been shown that a velocity of  $2\text{ m/s}$  also produces periodic results. However in a finer mesh this showed slightly more variations in the periodic flow. Therefore a 'safer' velocity is chosen by taking the free-stream velocity equal to  $3\text{ m/s}$ . For this periodic flow the final periodic solution is used to compare the meshes. The difference between the solutions should not be significant compared to the variation in the chaotic flow results shown in Chapter 6. After this the chaotic flow is used to determine whether the difference in the average is acceptable. This is done by comparing the results to the differences caused by the variation in the solver parameters shown in Chapter 6. All this is done using a single wing. The simulations for the complete 'clap-and-peel' motion with two wings cannot be performed in parallel and is therefore not applicable in the mesh study simulations due to the long simulation times. Four meshes are used during the simulation. In Table 7.1 the size of meshes is stated. All meshes have the same far-field distance (45 chords in each direction).

#### 7.1.1 Periodic flow

Firstly the periodic flow is used to determine which mesh resolution is sufficient when considering the flapping wings in hovering conditions. By inducing a flow through the domain the flow becomes periodic. A velocity of  $3\text{ m/s}$  is used to achieve this.

**Table 7.1** Meshes used during the mesh study.

Mesh name	Number of cells
Very coarse	6098
Coarse	15314
Normal	59906
Fine	231628

In Figure 7.1 the upward force coefficient in the last period is shown for the four meshes considered during this study. Looking at the integrated upward force the

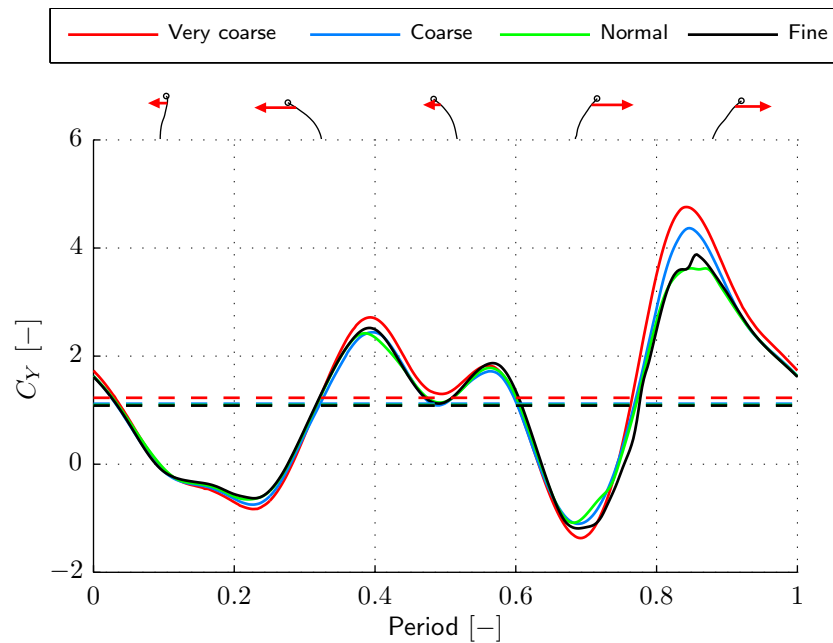


**Figure 7.1** Upward force coefficient for different meshes when a free-stream velocity of  $3 \text{ m/s}$  is induced on the flow.

deviation compared to the finest mesh for the other 3 meshes are as stated in Table 7.2. It is clear the the coarsest mesh is way off. The coarse mesh and the normal mesh are near or below the 4 % deviation seen in the chaotic simulations. However the periodic force profile shows a difference between the coarse and the two finer meshes at the second peak. Here the coarse mesh shows a bigger deviation than average.

**Table 7.2** Integrated upward force for 4 meshes in the periodic conditions and chaotic conditions.

Mesh name	Periodic	Chaotic
Very coarse	1.227 (13.292 %)	2.88 (5.0 %)
Coarse	1.117 (3.122 %)	2.95 (7.6 %)
Normal	1.093 (0.944 %)	2.85 (3.9 %)
Fine	1.083 (0 %)	2.74 (0 %)

### 7.1.2 Chaotic flow

For the hovering conditions again the four meshes are used for simulating 44 periods of the DelFly II flapping motion. To eliminate the start up effects the first 10 periods are not used in calculating the average. The resulting periodic averaged upward force can be found in Figure 7.2 for all four meshes. In Table 7.2 the integrated values

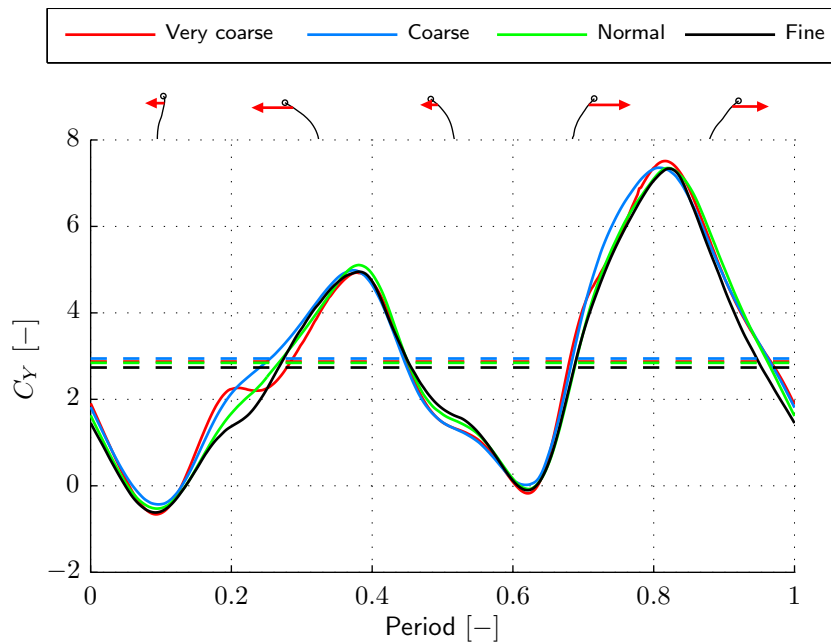


**Figure 7.2** Upward force coefficient for different meshes when hovering conditions are used.

can be found. When using the hovering conditions the integrated force coefficients do not show a clear trend as seen in the periodic conditions. For the chaotic case the coarse mesh shows the biggest deviation with a value of 7.6 %. However the other two deviations are similar to the deviations found due to different solver parameters as shown in Chapter 6. A second comparison can be made on the trend in the force within a period. For the coarsest mesh it can be seen that shedding of the

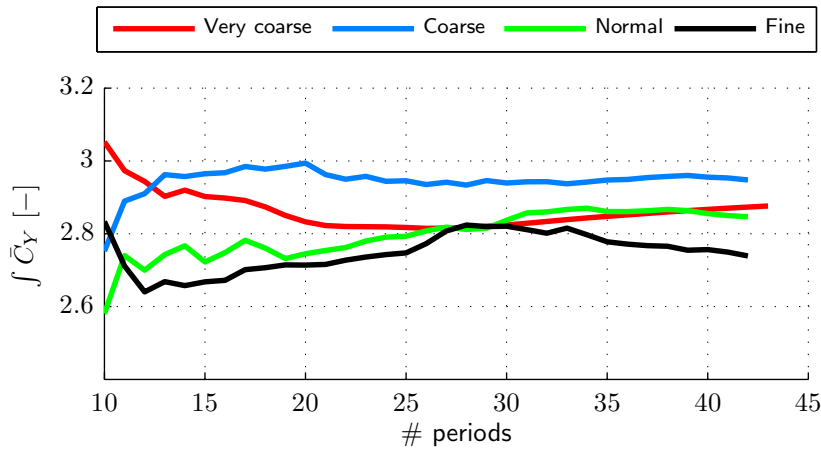
leading edge vortex takes place during the start of the out-stroke (at 24 % of the period), while the other meshes do not show this behaviour. Therefore it is clear that the coarsest mesh is not suitable to get a clear picture of vortex shedding near the wing. Another question is how well the average is estimated. Looking at average and standard deviation convergence from the results shown in Figure 7.2 it can be concluded that for the finer meshes the convergence is less. In Figure 7.3 the two statistical parameters are displayed against the number of periods used for determining their values. There is still convergence, however it seems that the graph is still oscillating around a value. Based on the convergence and the actual value of the standard deviation it is clear that for finer meshes the deviations from the average are larger. Especially between period 25 and 28 the instantaneous force profiles show large deviations from the 'average'. This can be concluded from both the average, which shows a small increase, and the standard deviation, which shows a large jump due to this larger deviation. It is clear that the normal mesh is the best trade-off between capturing the important aerodynamics, efficient calculations and convergence of statistical values. When parallel processing is available this mesh will be used. For the 'clap-and-peel' simulations parallel processing is not available for all methods. Therefore the coarse mesh will be used there. It is important to realise that the comparison must be based on differences between results and the the actual values of the upward force coefficient are of less importance and less reliable. The coarse mesh is still able to capture the general trend of the force, which is important for comparing the results of rigid and flexible wings.

## 7.2 Influence of the Courant number

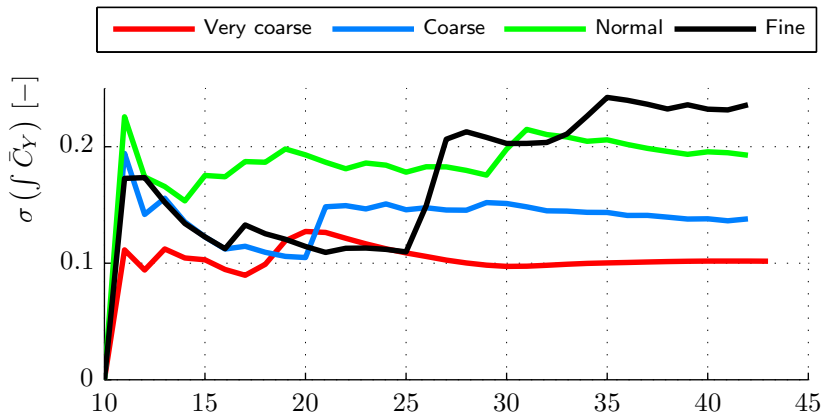
Besides the mesh resolution also the maximum Courant number during calculation is a parameter influencing the results. A smaller Courant number will reduce the maximum time step and increase accuracy. For stable calculations the Courant number must be below 0.9, which is determined by means of trial and error. Large Courant numbers are also not possible in the 'clap-and-peel' simulations, since in that case too many cells will move through the symmetry plane within one time step. To determine which Courant number can be used a similar approach is taken as in the mesh study. Both the periodic flow and the chaotic flow are simulated with the coarse mesh. Based on the differences between the integrated periodic average and the trend of the force profile a Courant number can be chosen, which provides a good trade-off between efficiency and accuracy.

### 7.2.1 Periodic flow

Firstly the periodic flow is used to identify the influence of the Courant number. Again a free-stream velocity of 3  $m/s$  is used to generate a periodic result. Four Courant numbers are used in the simulations: 0.8, 0.4, 0.2 and 0.1. In Figure



(a) Average upward force coefficient.



(b) Standard upward force coefficient.

**Figure 7.3** Statistical parameters convergence for mesh study using hovering conditions creating a 'periodic chaotic' flow.

7.4 the resulting periodic solutions are shown for all four Courant numbers. It is clear that only the Courant number of 0.8 shows visible difference in both the force profile and the integrated value. Compared to the differences due to the mesh resolution these differences are small. In Table 7.3 the values for the integrated periodic average upward force coefficient and their relative difference from the lowest Courant number can be found. From these results it can be concluded that all Courant numbers provide acceptable accuracy. However for stability reasons and the topology changing algorithm a Courant number lower than 0.8 will be a better choice.

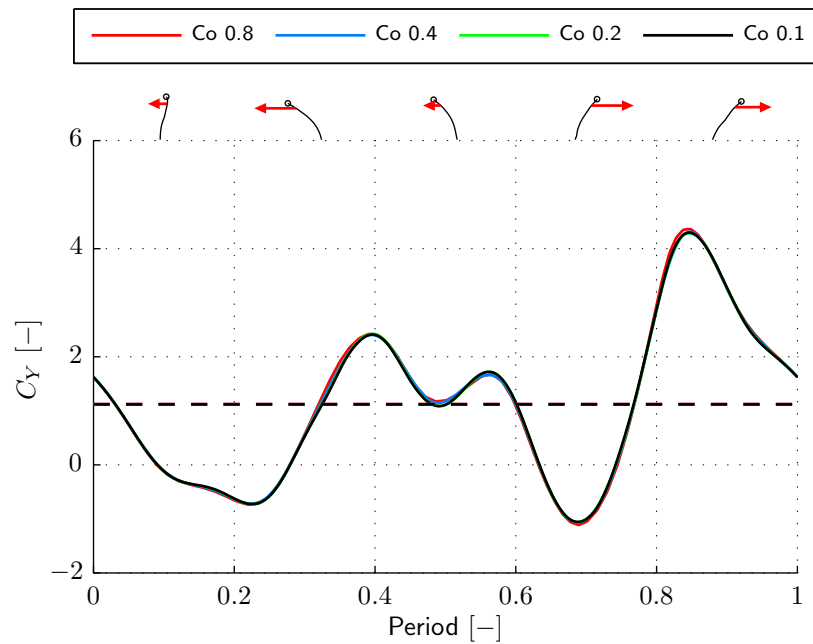


**Figure 7.4** Upward force coefficient for different Courant numbers for a flow with a free-stream velocity of 3 m/s creating a periodic flow.

**Table 7.3** Integrated upward force for 4 Courant numbers in the periodic and chaotic conditions.

Courant number	Periodic	Chaotic
0.8	1.124 (0.706 %)	2.88 (0.35%)
0.4	1.119 (0.214 %)	2.95 (1.89 %)
0.2	1.116 (0.075 %)	2.97 (2.8 %)
0.1	1.117 (0 %)	2.89 (0 %)

### 7.2.2 Chaotic flow

When hovering conditions are considered the flow becomes chaotic. Based on the periodic results Courant numbers between 0.1 and 0.8 provide similar results. However due to the chaotic character no such trend is expected in these results. In Figure 7.5 the results for hovering conditions are shown for the four Courant numbers. For a Courant number of 0.8 there is almost no difference in the integrated value compared to the results with a Courant number of 0.1. However looking at the periodic average force profile it can be seen that there is a small dip present in the force profile during the out-stroke with a Courant number of 0.8. At 24 % of the period this dip can be found in Figure 7.5. The other two (0.4 and 0.2) do not show this dip, but for a Courant number of 0.1 a similar but smaller dip is found.

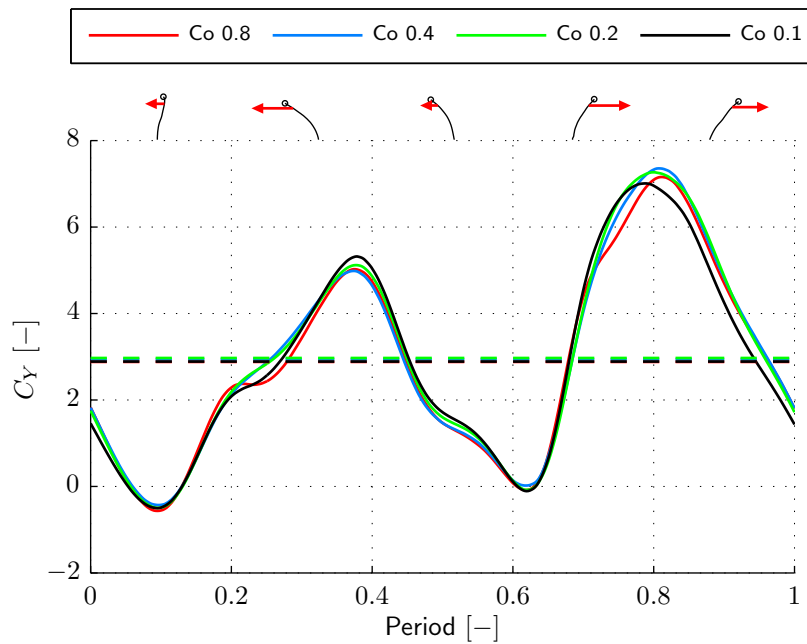


**Figure 7.5** Upward force coefficient for different Courant numbers for hovering conditions creating a chaotic flow.

Looking at the integrated periodic average, the differences are within the margin provided by the influence of chaotic flow due to solver parameters. As already stated in the previous paragraph a Courant number lower than 0.8 is desired considering stability and the topology changing method. Therefore a Courant number of 0.4 will be used in all remaining simulations.



# 8

## Results

With the method of introducing a symmetry plane in the mesh while maintaining good mesh quality, simulations of the 'clap-and-peel' motion can be performed. The first step in determining the influence of a deforming wing on the performance is made by simulating a single wing. The second step is to simulate the 'clap-and-peel' motion. Before this is done the two methods discussed earlier are compared and validated using the Miller-Peskin motion. For the mesh topology changing method the DeFly II 'clap-and-peel' motion is simulated for all wing kinematics discussed in Chapter 4. Finally the influence of the gap size during the 'clap-and-peel' motion on the aerodynamics is investigated by increasing and decreasing the minimum size of this gap during a period. Additionally the motion of the DeFly II deforming wing is rotated to ensure that the minimum gap at the leading and trailing edge are the same.

### 8.1 Influence of flexibility for a single wing

With the normal mesh and a Courant number of 0.4 the simulations for a single wing in motion are performed. Each of the four wings discussed in Chapter 4 are simulated to determine the influence of flexibility for a single wing. This will give a first indication on what phenomena are important to determine the difference between rigid and flexible wings. Both the periodic average as well as the vorticity fields will be shown to indicate the important differences. At the end of this section the upward force coefficient and the required energy per period are compared for all wings.

For the rigid and flexible wings the forces are calculated for several periods. In total 44 periods are simulated for each calculation. A periodic average is calculated from periods 11 till 44. In Figure 8.1 the periodic average of the upward force is shown for the different wings making the single wing motion. The dashed line is the integrated force of the average period. Comparing the four wings it can be seen that the integrated periodic average upward force coefficient increases when flexibility increases. The main differences are around 24 %, 38 %, 52 % and 82 % of the period. The vorticity field for these times are shown in Figure 8.2 for the rigid, flexible and super-flexible wing. For the semi-flexible wing vorticity plots are not

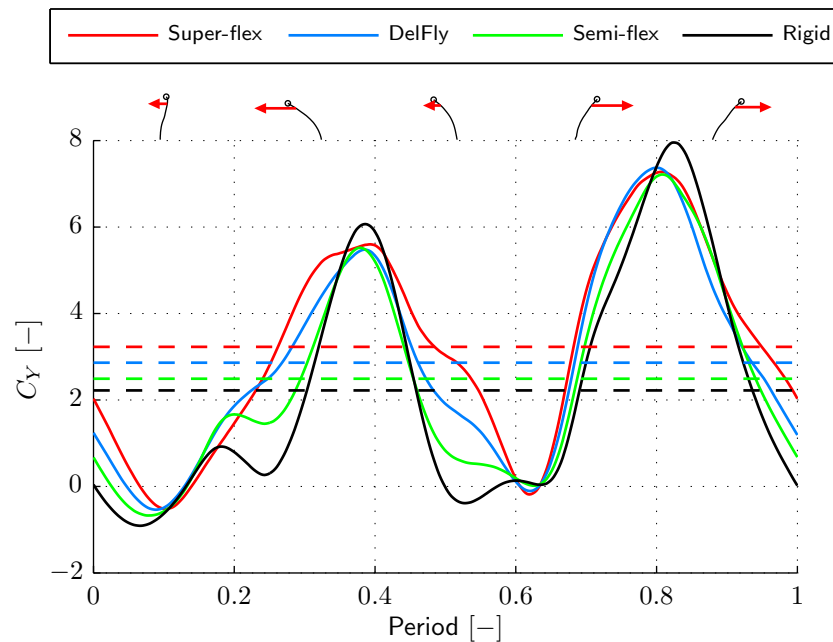


**Figure 8.1** Periodical average of the upward force for the rigid and flexible wings in the single wing motion.

shown because they are a mix of the rigid and DelFly wing in this case. They do not add extra insight in the influence of flexibility in single flapping wings. At the beginning of the out-stroke there is a clear difference between all four wings in the force profile. For the rigid and semi-flexible wing a dip is present at 25 % of the period, which is caused by the shedding of the leading edge vortex (LEV) as can be seen in Figure 8.2(a). This is caused by the high angle of attack at the beginning of the out-stroke. When flexibility is present the angle of attack is already reduced before the out-stroke starts. Due to this the vortex remains attached longer (or does not shed at all in the case of the super-flexible wing, see Figure 8.2(c)). The DelFly wing is on the verge of shedding the LEV (see Figure 8.2(b)) but just before the LEV is shed (around 50 % of the period) the wing decelerates to start the stroke reversal (from 50 % to 60 % of the period). Due to this the LEV remains near the wing and does not effect the force in a large extend. In this phase more flexibility provides a higher upward force due to the attachment of the LEV caused by the relatively low angle of attack.

Just after the middle of the out-stroke (at 38 %) all four wings show a large peak in the force. At this time the LEV has a high strength and the trailing edge vortex (TEV) is shedding. There are no major differences in the vorticity fields. For the most flexible wing the first LEV is still present (see Figure 8.2(f)), while for the rigid wing the second LEV has developed fast and causes a larger force peak as can be seen in Figure 8.2(d). For the DelFly wing a lower value of the force can be seen because part of the LEV has shed just before this point in the period (see Figure

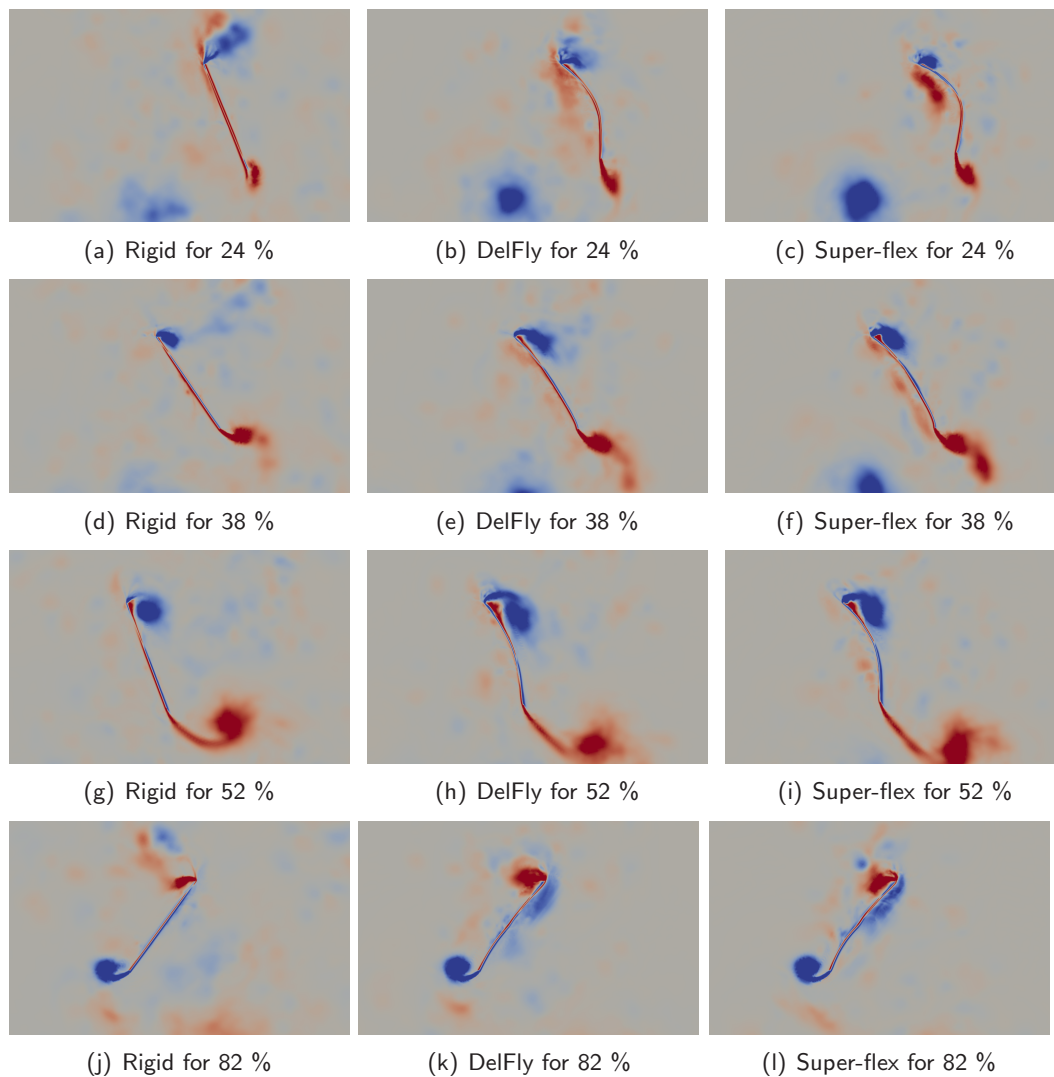


**Figure 8.2** Vorticity fields for the rigid, flexible and super-flexible wing. Times in the period are shown for which the main differences occur in the force profile, shown in Figure 8.1.

8.2(e)). However all show a strong LEV and a shedding of the TEV. At the end of the out-stroke and start of stroke-reversal (around 52 % of the period) several effects can be seen. Firstly the TEV is convected away from the wing faster for the DelFly and the super-flexible wing than for the rigid wing, causing a higher upward force. The rigid wing has a lower force mainly due to the orientation of the wing. Due to the rotation the wing is almost vertical, while more flexibility causes a lower angle of attack and thus more horizontal area. Even though the rigid wing has a similar LEV as the DelFly wing (see Figure 8.2(g) and 8.2(h)) the resulting upward force is lower. Besides the orientation, the LEV is also providing a higher force for the super-flexible wing, which is seen in Figure 8.2(i).

Finally the middle of the in-stroke (at 82 % of the period) is considered. In Figure 8.1 a difference can be found between the flexible wings and the rigid wing. The rigid wing shows a significantly higher force, than the other three wings. After rotation the rigid wing develops its first LEV very fast, because it interacts with the previously shed LEV from the out-stroke. This LEV convects upwards causing an increase in the velocity over the leading edge. This new LEV is shed immediately due to this increase in velocity after which the second vortex LEV is developed (see Figure 8.2(j)), which is at its strongest around 82 % of the period. For the DelFly wing also the capturing of the LEV from the out-stroke influences the development of the new LEV. Because of the curvature of the wing the previous LEV is captured below the wing and the effect seen in the rigid wing is only partly there. As a consequence the LEV does develop, but starts shedding during translation, resulting in a lower peak than the rigid wing. In Figure 8.2(k) this shedding can be seen, while for the rigid wing no real shedding has started yet. For the super-flexible wing similar phenomena are observed as for the DelFly wing because the amount of deformation during the in-stroke is minimal. The LEV has also started shedding slightly at 82 % of the period, which can be seen in Figure 8.2(l). For all wings the development and shedding of the TEV is similar and does not cause a major difference. This second peak around 82 % of the period is higher than the first peak during the out-stroke (at 38 %). Because of the larger angle of attack during the in-stroke this difference is present.

Several aspects have been identified in the analysis of the influence of flexibility on a single flapping wing. During the out-stroke the decreased angle of attack due to flexibility is beneficial because it prevents shedding of the LEV. Also the orientation of the wing can be of major influence. With a deforming wing the orientation and angle of attack of the leading edge can be altered before translation, while for a rigid wing this is more difficult. Because these motions are also used for the 'clap-and-peel' motion no further investigation is done in the effects of different rigid wings in the single wing case. A smaller angle of attack during translation might reduce the differences. However a rigid wing will never be able to change its leading edge angle of attack without rotation. For the flexible wing this is possible by bending its leading edge and thus causes a low angle of attack and more horizontal area at the start of the out-stroke.

During the in-stroke the most important phenomena is the interaction with the previously shed LEV during the out-stroke. Due to the curved shape of the flexible wings the LEV remains mainly below the leading edge, while for the rigid wing the LEV is convected upwards. This eventually leads to a stronger developed LEV for the rigid case at in-stroke.

Integrating the periodic average force profile shows large differences between the wings. In Table 8.1 the integrated values and relative differences can be found. It can be seen that the integrated upward force coefficient ( $C_Y$ ) increases for increasing flexibility. Especially the differences between the rigid and the DelFly and super-

**Table 8.1** Integrated upward force and absolute horizontal force for the 4 wings with different amounts of flexibility.

Wing	$\bar{C}_Y$	$\bar{C}_X$
Super-flexible	3.23 (45.1 %)	6.92 (29%)
DelFly	2.87 (29 %)	6.19 (15 %)
Semi-flexible	2.50 (12 %)	5.37 (0 %)
Rigid	2.23 (0 %)	5.37 (0 %)

flexible wing are significant. Compared to a difference of 4 %, which can be created by the chaotic aerodynamics, the increase in upward force due to flexibility is big. These differences can be contributed to the aspects discussed above. Especially the possibility of flexible wings to quickly reduce their angle of attack at the LE before translation influences the vortex development and thus force production.

Besides the integrated upward force coefficient also the integrated absolute horizontal force coefficient ( $C_X$ ) is shown. It can be seen that the drag increases when the flexibility is increased. This gives a first indication on the amount of energy needed to translate this wing. To determine the energy needed, the power needed in time is integrated for the average period. For the power calculations the periodic average drag is multiplied by the horizontal velocity of the leading edge. The energy needed per period is computed by integrating over a single period and dividing by the characteristic velocity. In mathematical form this is shown in Equation (8.1).

$$E = \frac{\int_0^1 C_X(\tau) U_X^{le} d\tau}{U_{ref}} \quad (8.1)$$

The DelFly wing is solely controlled by a translational movement of the leading edge. All the other movements seen in the experiments are caused by the flexible wing. Therefore, under the assumption that the shape enforced during the simulations is close to the flexible shape, the total drag coefficient of the wing is multiplied by the horizontal leading edge velocity to obtain the power. However the wings are not simulated as passive flexible wing, but as active flexible wings. The assumption made for the energy calculation is becoming less realistic when the deformation is increased. Still this method gives a indication on the efficiency found in flexible wing motions instead of using the lift over drag ratio. In Table 8.2 the energy for the four wings considered is shown. It can be seen that the trend seen in the drag is similar to the trend in the energy. The amount of energy needed to perform this motion on the assumption of flexible wings increases for a more flexible wing. However the ratio of lift over energy needed per period is still increasing for increasing flexibility. It should be noted that the more deformation a wings shows, the less realistic the assumption becomes.

**Table 8.2** Energy needed per period for the 4 wings in single wing motion.

Wing	E [-]	$\frac{C_Y}{E}$
Super-flexible	8.05 (31 %)	0.412 (12 %)
DelFly	7.31 (21 %)	0.393 (7 %)
Semi-flexible	6.49 (7.18 %)	0.385 (5 %)
Rigid	6.05 (0 %)	0.369 (0 %)

## 8.2 Clap and peel with flexible and rigid wings

Simulating two wings clapping and peeling together is done by imposing an immersed symmetry boundary in the mesh. Two methods are used and are compared first. After this the differences between the four wings (rigid, semi-flexible, DelFly and super-flexible) are studied. During this comparison the results obtained with a single wing are also used to determine the influence of the 'clap-and-peel' motion for the different wing kinematics.

### 8.2.1 Method comparison

Two methods are used for simulating the 'clap-and-peel' motion. Both methods use an immersed symmetry plane to model the presence of the second wing. The first method is the explicit immersed boundary method which enforces the symmetry conditions by interpolation and iterating over the PISO loop (see section 5.2). Secondly a method which deforms the cells cut by the immersed symmetry plane, such that a row of faces can form an actual boundary, is used (see section 5.1). In this way the boundary conditions are enforced implicitly and inside the discretisation. In this paragraph both the methods are compared to determine which method provides the best results considering the 'clap-and-peel' motion. The Miller-Peskin motion at a Reynolds number of 128 is used as first comparison. Secondly the DelFly II motion (at a Reynolds number around 9600) is simulated to determine if at the higher Reynolds numbers the methods can perform well.

#### Miller-Peskin motion

In this paragraph the focus is on the comparison between the two methods and not on the validation of the methods with [25]. Known problems with the immersed boundary method are numerical oscillations (see [21]). However these problems also depend on the Reynolds numbers. At higher Reynolds numbers a sharper interface must be present to prevent numerical oscillations and larger interpolation errors (see e.g. [27]). The focus in this part is to see whether both the methods are able

to capture the correct behaviour without significant oscillations at a low Reynolds number (128).

In Figure 8.3 and Figure 8.4 the resulting lift coefficient and drag coefficient from the Miller-Peskin fling motion is shown for the immersed symmetry plane method and the topology changing method together with the results from [25]. From the

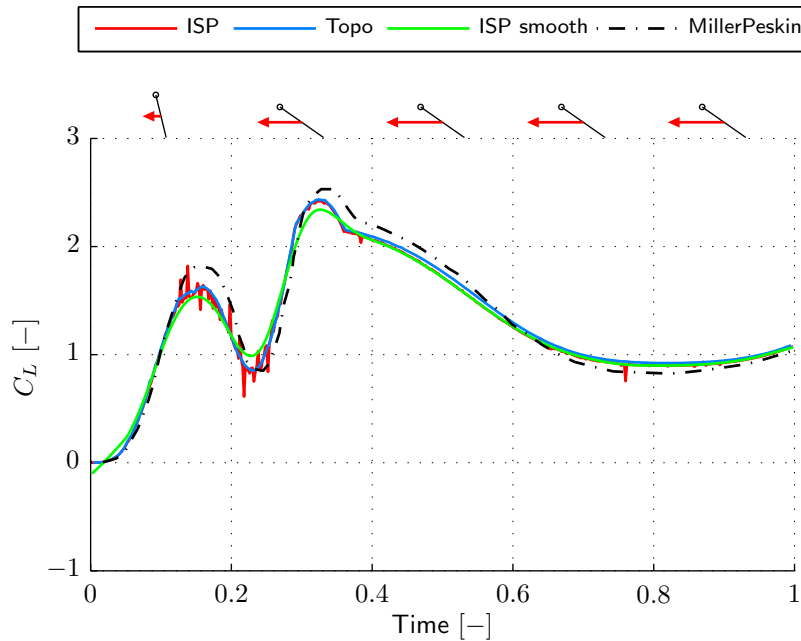


**Figure 8.3** Lift coefficient for the fling motion of Miller-Peskin at a Reynolds number of 128. Two methods, the immersed symmetry plane (ISP) and the topology changing method (Topo), are compared in this graph. Also the results from [25] are plotted.

force profile it can be seen that the immersed symmetry plane method does show some oscillations, especially at the first part when the immersed symmetry plane is close to the wing. At those moments the interpolation has a more direct effect on the pressure near the wing and thus on the forces. When smoothing is applied to the results of the immersed symmetry plane the trend and values of the force profile are similar to the results from the topology changing method. This topology changing method is however not smoothed. In the drag coefficient there is a small oscillation present for the topology changing method, which can be contributed to the simple interpolation for the new cells entering the domain. These cells can be badly shaped when entering the domain causing this small oscillation. The difference between the methods can be explained by the fact that the boundary conditions are enforced implicitly using the same discretisation as the whole field and are at the correct location in the topology changing method. In the immersed symmetry plane method the boundary conditions are enforced using an explicit method and interpolation to the nearest cells. However smoothing does provide a similar result.

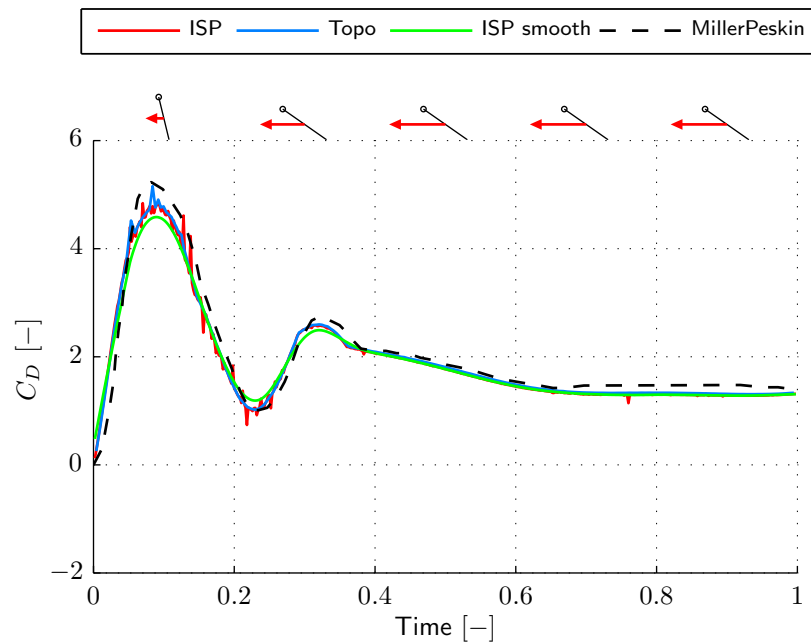


**Figure 8.4** Drag coefficient for the fling motion of Miller-Peskin at a Reynolds number of 128. Two methods, the immersed symmetry plane (ISP) and the topology changing method (Topo), are compared in this graph. Also the results from [25] are plotted.

### DeIFly II motion

At higher Reynolds numbers the influence of a non-sharp interface becomes bigger ([27]). For the immersed symmetry plane this is of great importance. In this paragraph the comparison between the ISP and Topo method is continued. For the results used in this paragraph 44 periods are simulated with the immersed symmetry plane to model the second wing. Both methods are used for this. An average periodic force profile is calculated based on the 11 till 44 period. In Figure 8.5 and Figure 8.6 the results can be found together with the smoothed force profile of the ISP method. Compared to the results from the Miller-Peskin motion, at a Reynolds number of 128 from the previous paragraph, a large increase in numerical oscillations are found in the results from the immersed symmetry plane method. Besides the higher Reynolds number also the minimum distance between the wing and the symmetry plane (and thus the interpolated cell values) is smaller compared to the Miller-Peskin motion. Both these aspects result in more numerical oscillations. However the integrated value of the upward force coefficient does provide a good estimate when compared to the integrated value of the topology changing method. They differ by 7 %. In the trend of the smoothed ISP curve there are some differences at the two 'peaks' compared to the topology changing force curve. When comparing the horizontal force coefficient a larger difference is found, which results in a difference of 20 % in the integrated value. Especially during the out-stroke this

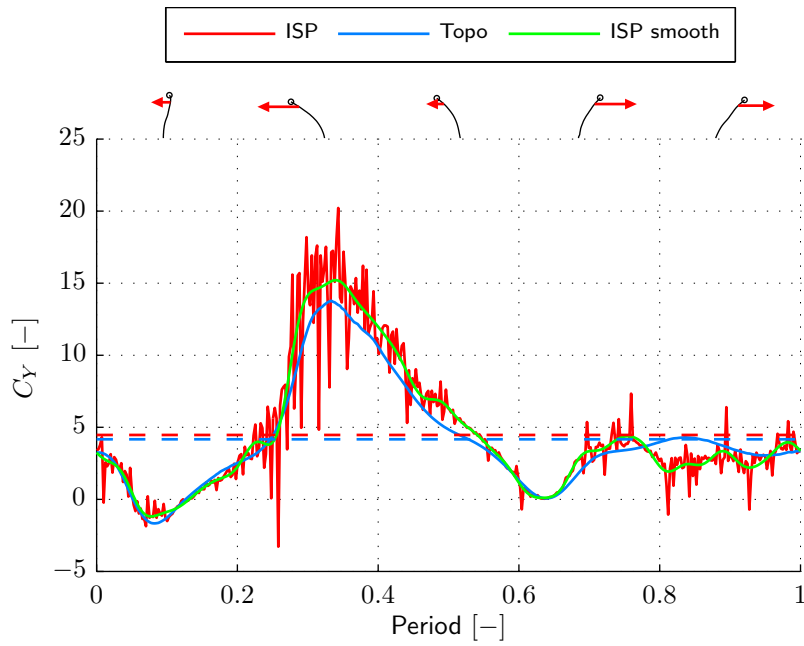


**Figure 8.5** Lift coefficient for the DelFly II 'clap-and-peel' motion at a Reynolds number of approximately 9600. Two methods, the immersed symmetry plane (ISP) and the topology changing method (Topo), are compared in this graph.

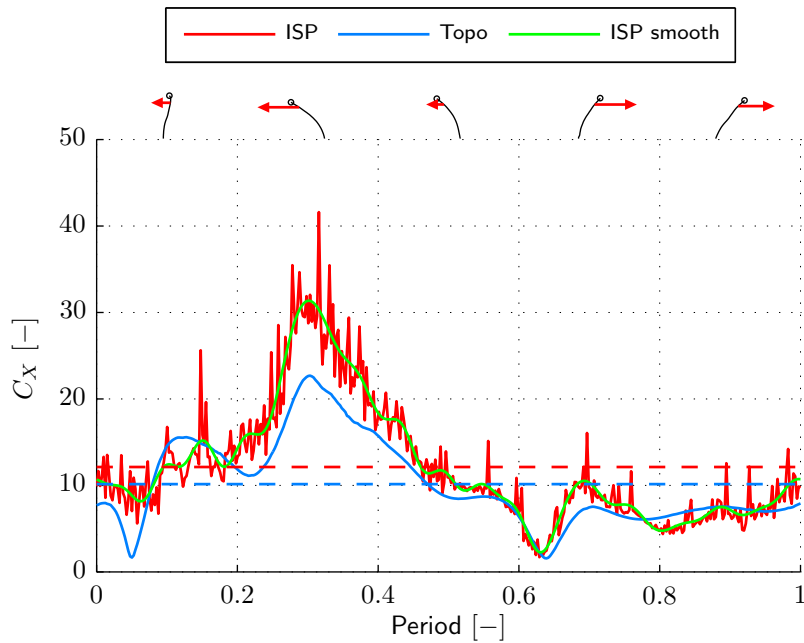


**Figure 8.6** Drag coefficient for the DelFly II 'clap-and-peel' motion at a Reynolds number of approximately 9600. Two methods, the immersed symmetry plane (ISP) and the topology changing method (Topo), are compared in this graph.

large difference is present. At this point the part of the wing at the trailing edge is almost vertical and very close to the symmetry plane. When the out-stroke starts lots of cells will enter the domain near the trailing edge, causing the oscillations and the offset. Due to the orientation (almost vertical at trailing edge) and kinematics of the wing (bending of the leading edge away from the symmetry plane) this is not found back in the upward force coefficient and only seen in the horizontal force coefficient. The topology changing method does provide a better solution, because of the absence of the oscillations. Also the enforcement of the boundary conditions are correct, while in the immersed symmetry plane they are only used to interpolate values near the symmetry plane via a weighted non-linear least squares interpolation. This interpolation does not ensure that the conditions are exactly enforced when the cell centre is exactly at the symmetry plane due to the least squares interpolation.

Known solutions to numerical oscillations due to the use of the immersed boundary method are stated in [21]. The two proposed methods are decreasing the cell size of the mesh and increasing the time step. According to [21] the best method is to increase the mesh resolution. Also the possibilities to increase the time-step are limited, because unstable simulations will arise due to the large Courant number. For the coarse mesh in Figure 8.5 the maximum difference between the smoothed curve and the original curve is 60 %. The value is normalized by the range of the smoothed curve. When taking this same approach for the normal mesh a maximum difference of 43 % is found. However the cell size is reduced by a factor of 4. Going much further in cell size will make the simulation times extremely long, while the topology changing method will still perform better.

From the comparisons shown in the two paragraphs it is clear that both methods perform well in terms of integrated periodic average upward force, even though the ISP method needs some filtering. For the higher Reynolds number DelFly II case the numerical oscillations found in the ISP method after averaging over 34 periods are large and undesirable. Filtering does provide a solution to get a smooth curve, which also has an integrated value close to the topology changing result when the upward force coefficient is considered. When the horizontal force coefficient is considered this is not the case. A large off-set is found between the smoothed ISP curve and the topology changing curve. The ISP method does not enforce the boundary conditions at the exact correct location, while the topology changing method does. Together with the extra iterations needed for the ISP method due to the loop over the complete PISO solver, the topology changing method is chosen. This method provides reliable results due to the correct enforcement of the boundary conditions and the absence of the numerical oscillations.

### 8.2.2 Validation with Miller-Peskin

To validate the topology changing method the results from the paper of Miller and Peskin from 2005 ([25]) are used. In their study two motions were investigated for low Reynolds numbers (8 to 128). These results are used to validate the method of immersing a symmetry plane in the flow to simulate the 'clap-and-fling' motion. Only the topology changing method are compared with the results from [25]. As shown in Chapter 4 a fling motion and a single 'clap-and-peel' motion are used. In this paragraph the comparison of the results will be discussed. During these simulations also a wing with a small thickness is used to show why a 'zero-thickness' wing is a valid assumption.

#### Fling

First the half-stroke fling is simulated. The wings start clapped together and start to fling apart and keep moving outside until the end of the motion. Both a single wing and a double wing simulation will be compared to the results from [25]. First the single wing simulation is used to determine if the mesh density is sufficient. In Figure 8.7 the lift and drag coefficient for two meshes are shown together with the results from [25]. From these results it is clear that both the coarse and normal mesh show similar results and that the coarse mesh is sufficient for simulations of the Miller-Peskin motion at a Reynolds number of 128. In [25] the mesh study showed that on their coarse mesh the force peaks are overpredicted. When compared to the fine mesh results from Miller and Peskin there is good correspondence. The differences between their coarse mesh results and topology changing method results, can be assigned to the use of the coarse mesh in the Miller and Peskin results (shown in [25]) and the immersed boundary method, which is generally outperformed by the ALE N-S approach (see [24]).

The next step is to look at the results of the double wing, which is simulated by means of a symmetry plane instead of two wings as done in Miller and Peskin. In Figure 8.8 the results of the double wing motion is displayed. Here the difference between the results and the reference from Miller and Peskin is bigger at the peaks as seen for the single wing. However a part of this difference is caused by the coarse mesh used in [25], which they showed at the beginning of the paper for the two wing fling motion. At the same time some discrepancies are expected since different methods are used. When looking at the general trend in the results, they are similar and show that the topology changing method does work properly and provides reliable results.

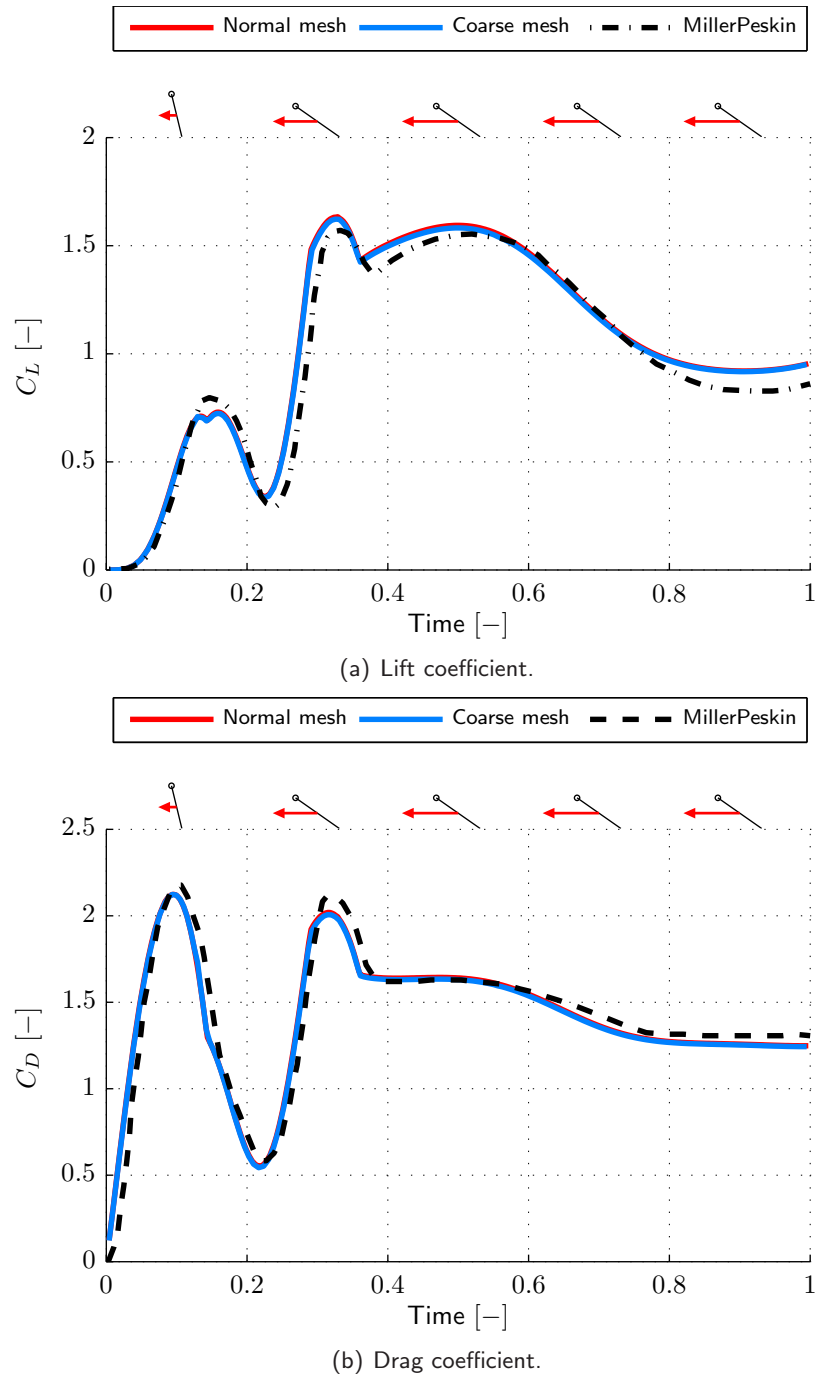
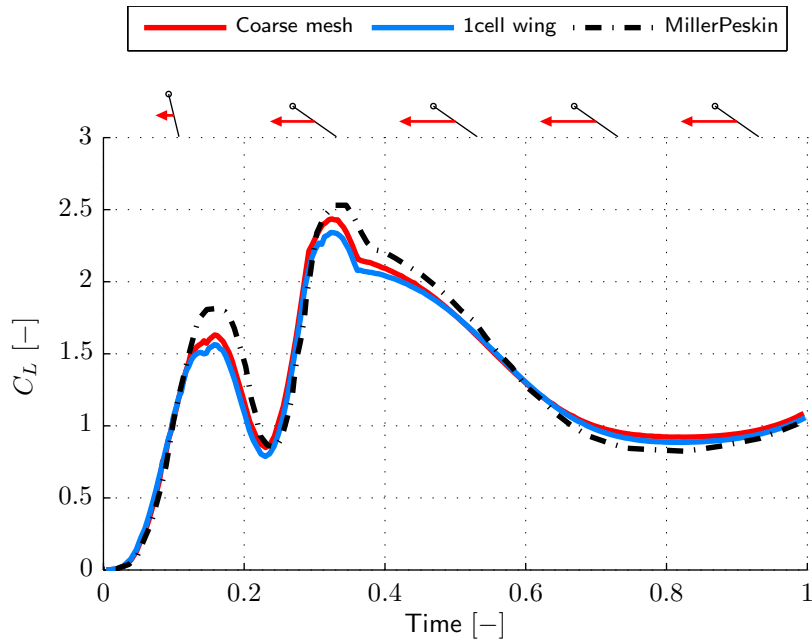
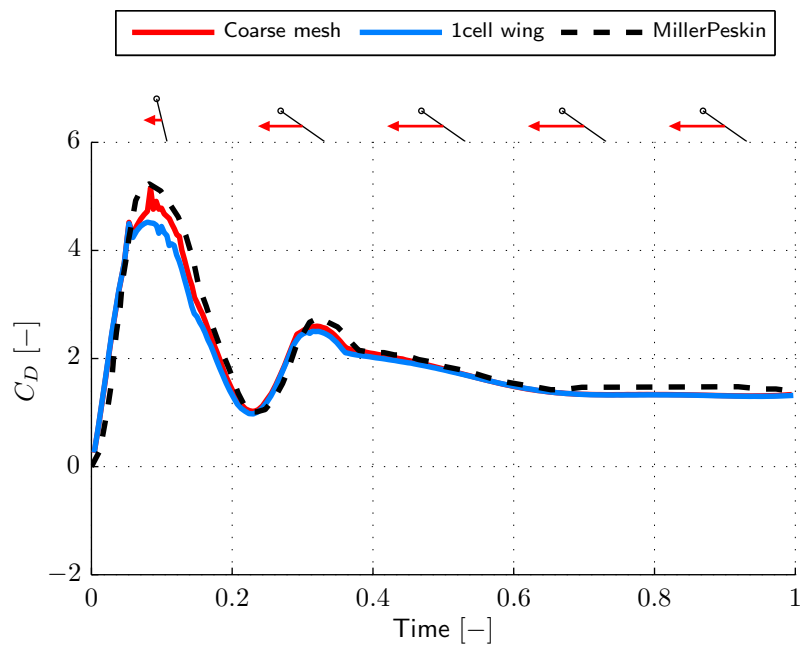


**Figure 8.7** Force coefficients for Miller-Peskin fling motion performed by a single wing.



(a) Lift coefficient.



(b) Drag coefficient.

**Figure 8.8** Force coefficients for Miller-Peskin fling motion performed by two wings.

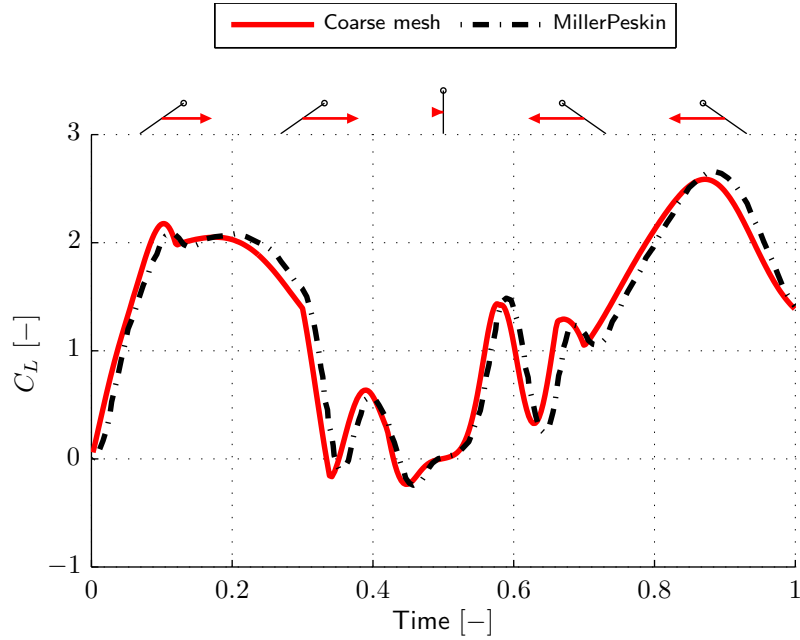
### Clap and fling

Additionally the full clap and fling motion is simulated to further check the validity of the proposed topology changing method. As done for the fling motion both a single wing and a double wing are simulated. In Figure 8.9 the results are shown for the single wing. There is a clear shift in time between the results. Since the profile of the force coefficient is shifted with the same amount over the whole period, the most logical explanation is a small time lag between the two motions. It might be the case that in [25] a small delay is present at the beginning of the motion. Besides the time shift there are some minor differences at the peaks in both the drag and lift coefficient. However the trends are captured correctly and the differences are relatively small considering the difference in methods and meshes.

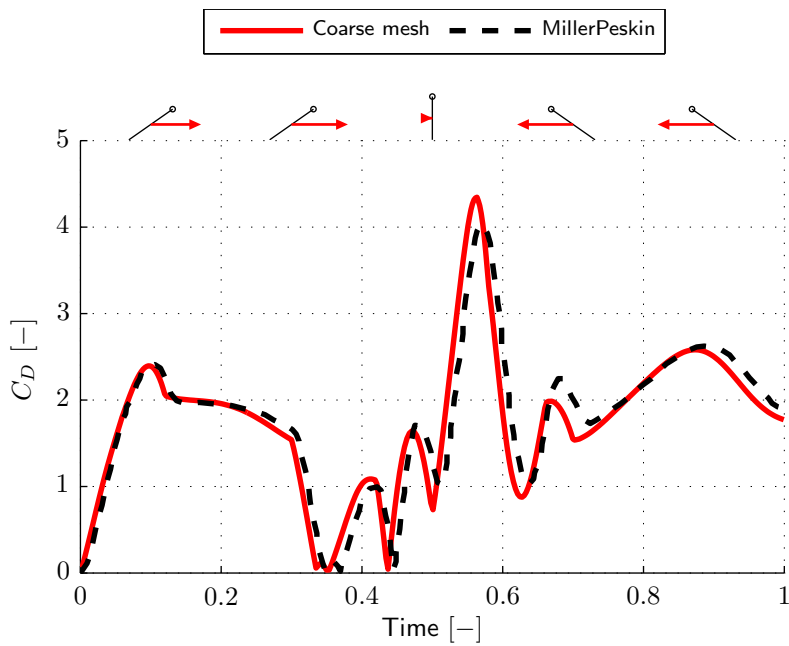
Lastly the complete clap and fling motion is simulated with the symmetry plane at the correct location. As seen in the fling case some differences can be expected due to the mesh and method used in [25]. The results can be found in Figure 8.10. In the two winged case all trends found in the results of [25] can also be seen in results of the topology changing method. Some small oscillations can be found in the drag coefficient (see Figure 8.10(b) at 55 % of the period), which are caused by the interpolation of (bad shaped) cells entering the domain. However this is expected due to the simple interpolation (weighted average), simple cell deformation algorithm near the symmetry plane and the coarse mesh. At the same time this is the most critical part of the period, because the wing just starts its fling phase. During this phase lots of cells enter the domain, while the wing is very close to the symmetry plane. When a finer mesh is used these oscillations will be barely visible on the global scale seen in Figure 8.10. The absolute value of the larger peaks can differ significantly and a small shift in time is present in the results. As discussed in the previous results the difference at the peaks can be expected due to the different methods and meshes. The shift is already present at the start of the simulations. However the movement enforced in the simulations are the kinematics explained in [25] and in Chapter 4. It might be the case that in the simulations of Miller and Peskin a small delay is present before the motion is initiated. However this does not change the conclusions on the validity of the topology changing method. The method is able to capture the development and shedding of the vortices which largely influence the forces. This method will be used in the further analysis of the influence of deforming wings in the 'clap-and-peel' motion.

### Influence of wing thickness

All simulations in this thesis are performed using a wing with no thickness. This wing is created by two rows of faces with no space between them. To check what the influence of a wing with a small thickness (1 cell) is the first simulation of a single wing making the fling motion is also performed. As can be seen in Figure 8.8 there is no significant influence when compared to the difference between the



(a) Lift coefficient.



(b) Drag coefficient.

**Figure 8.9** Force coefficients for Miller-Peskin clap-and-fling motion performed by a single wing.

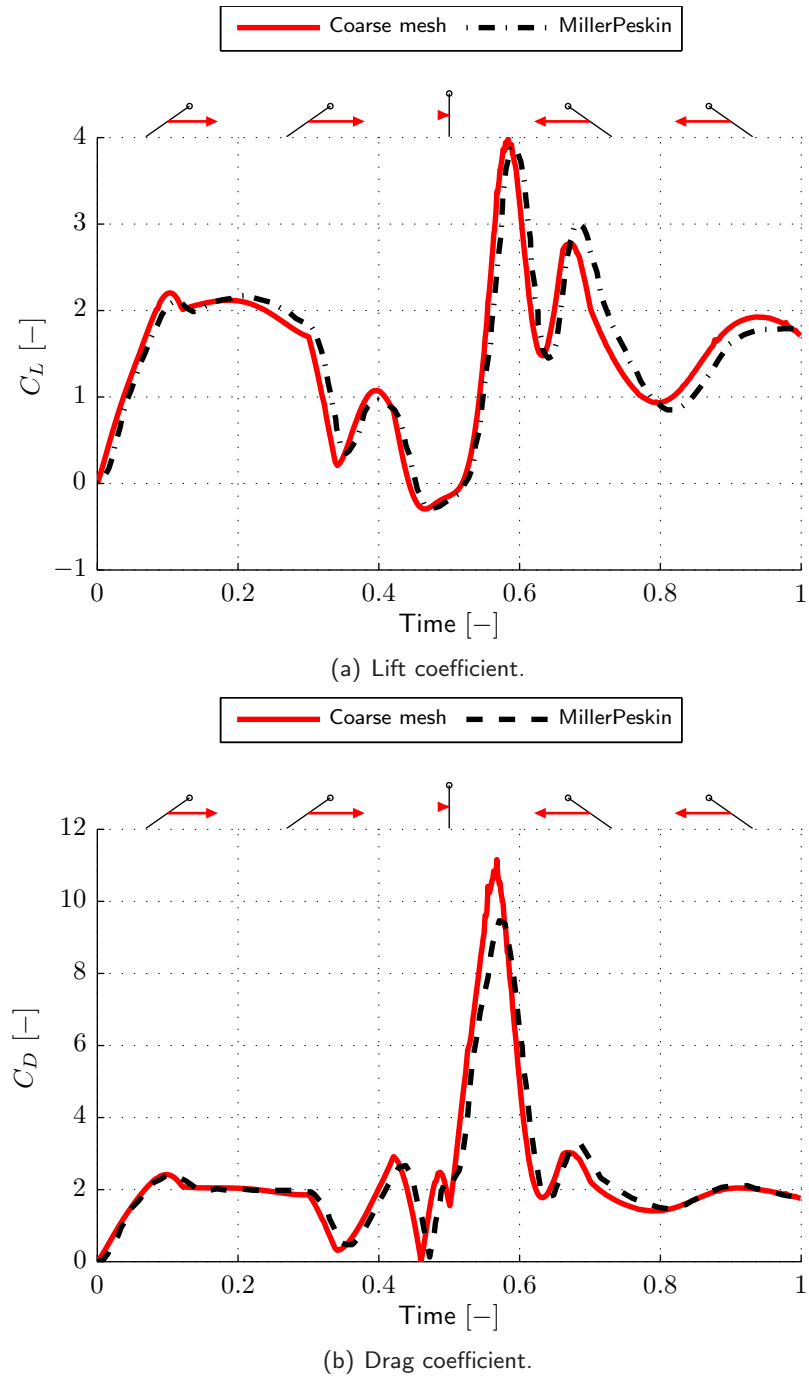


**Figure 8.10** Force coefficients for Miller-Peskin clap-and-fling motion performed by two wings.

Miller and Peskin results and the other results. Together with the uncertainty due to the chaotic aerodynamics in the main simulations a wing with 'zero' thickness will provide good results. For all remaining simulations the wing with 'zero-thickness' will be used.

### 8.2.3 Influence of flexibility

With the topology changing method to enforce a symmetry plane inside the domain the 'clap-and-peel' motion is simulated for the rigid and flexible wings. In this section a similar comparison as done for a single wing is made as well as a comparison between single wing movement and the 'clap-and-peel' motion. A periodic average is obtained by averaging from period 11 till 44. In Figure 8.11 the resulting periodic average is found for all four wings. The dashed line is the integrated periodic average. Looking at the integrated force a similar pattern can be found as for the single

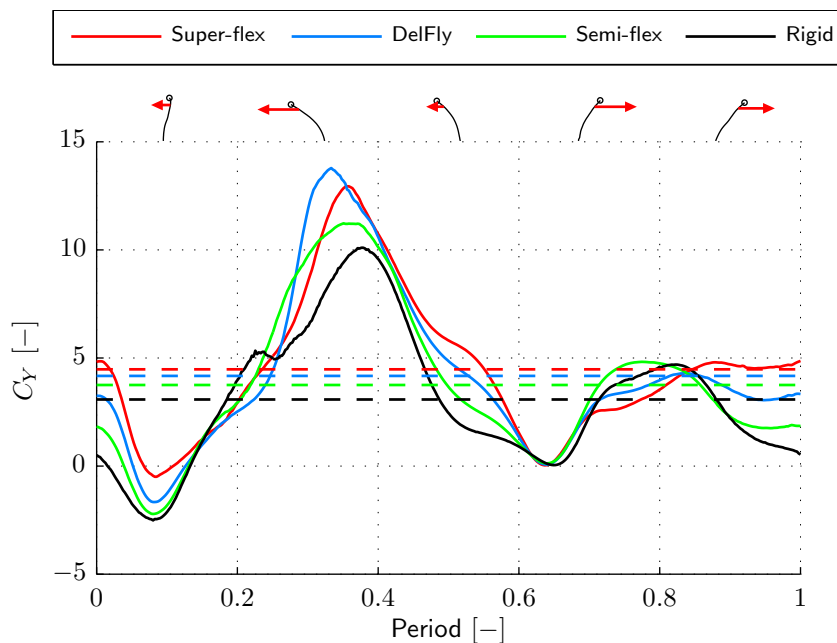


**Figure 8.11** Periodical average of the upward force for the rigid and flexible wings in 'clap-and-peel' motion.

wing. Increasing the flexibility increases the integrated periodic average upward force. Interesting points in the cycle to determine where these differences originate from are at 20 %, 30 %, 52 % and 98 % of the period. In Figure 8.12 the vorticity fields are shown for 20 %, 30 % and 52 % and the pressure field is shown for 98 % of the period.

From the force profile at 20 % of the period it can be seen that in the following

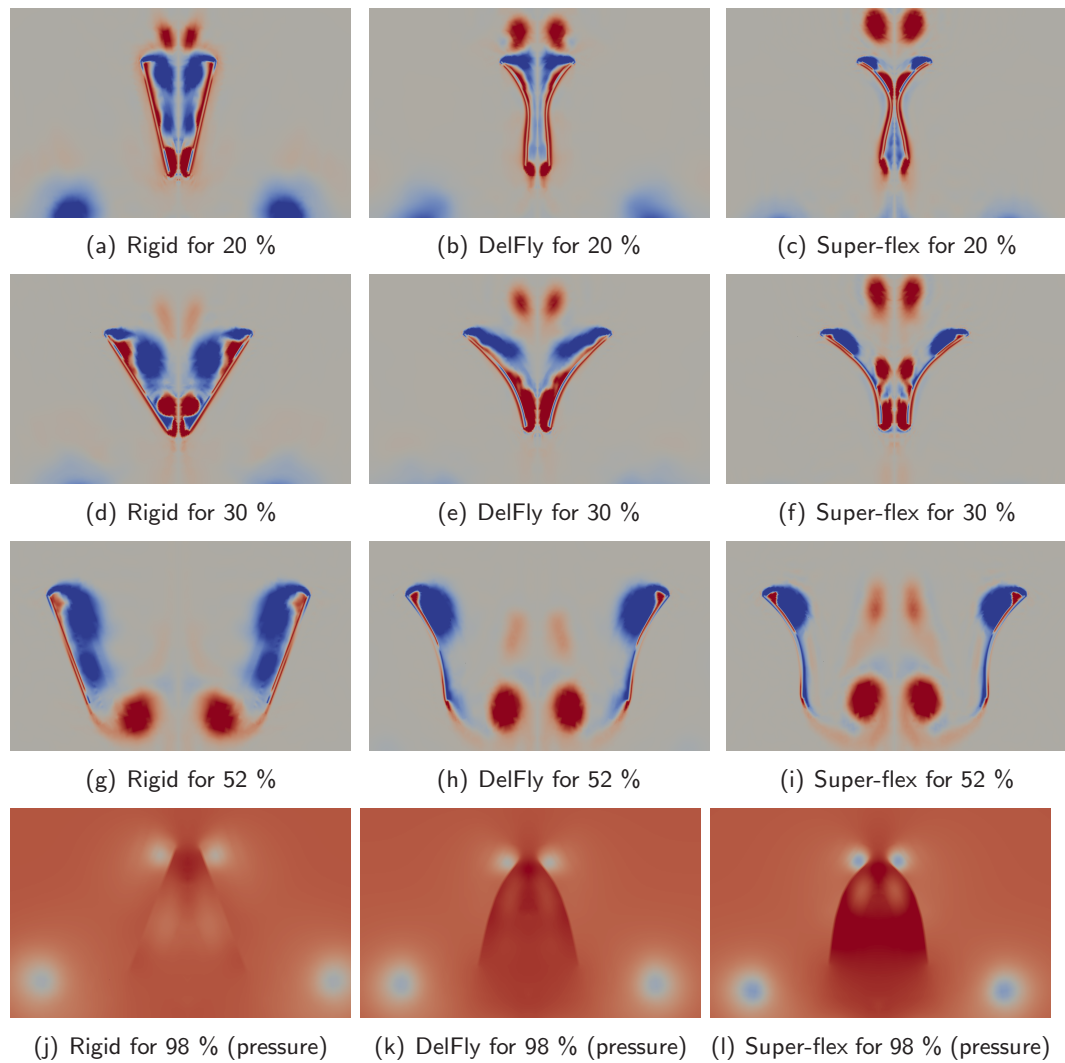


**Figure 8.12** Vorticity fields for the rigid, flexible and super-flexible wing performing the 'clap-and-peel' motion. Times in the period are shown where the main differences in the force profile, shown in Figure 8.11, originate from. For the last row of fields (at 98 % of the period) the pressure is shown instead of the vorticity.

phase the two most flexible wings will have a large increase in force, while the rigid wing will have a dip and does recover, but to a lower maximum force. At 20 % of the period the most important phenomena which cause this difference can already be seen. Due to the low pressure between the wings, caused by the fling phase, the flow velocity over the leading edge is high for all wings. This will be beneficial for the forming of the LEV. However in Figure 8.12(a) the large LEV already started shedding due to the rapid growth and the high angle of attack of the rigid wing. A similar effect is observed for the single wing (see Figure 8.2(a)). For the DelFly wing the lower angle of attack causes the shedding to be less. The small dip observed around 24 % of the period is caused by this, while for the super-flexible wing the LEV develops without shedding. As seen for the single wing the angle of attack of the leading edge is of major importance during peel phase. For 'clap-and-peel' motion this is further increased due to low pressure between the wings created by the peel phase.

After the peel phase has finished the translation phase starts. Around 35 % of the period the highest upward force is found for all wings. Looking at 30 % of the period the reason for the difference in maximum force can be derived. The rigid wing has shed its first LEV and started to develop the next one. However the translational phase is almost ending and therefore the LEV cannot develop further after 38 % of the period. Due to the shedding of the first LEV the maximum force reached is significantly lower than that of the other wings. The main difference between the DelFly and super-flexible wing is how fast the LEV develops. For the DelFly wing the first LEV did shed, but remained near the wing. In Figure 8.12(e) the two vortices are seen as one. Due to the higher angle of attack a stronger vortex is developed. For the single wing case the earlier shed vortex did not convect downwards but upwards, because of the lack of suction between the wings. In the case of 'clap-and-peel' this suction causes the LEV to convect downwards and contribute to the production of the force. For the super-flexible wing an extra anti-clock wise (for the left wing) vortex is created at the middle of the wing (see Figure 8.12(f) at the middle of the wing). This causes the force to build up a bit slower. Once this vortex is shed (just before 30 % of the period) the slope of the force profile increases. In Figure 8.12(f) the shed vortex can be seen, while the LEV is strong and big. However due to the extra vortex the maximum force is lower than the maximum force of the DelFly wing, which does not have this extra vortex.

At the end of the out-stroke (52 % of the period) similar differences can be found as for the single wing comparison (see Figure 8.1 and 8.11). The explanation for the differences are also the same and thus independent of the 'clap-and-peel' motion. The lower angle of attack causes the shedding of the vortex to happen at a later time for the more flexible wings, while for the rigid wing this happens earlier (see Figure 8.12(i), 8.12(h) and 8.12(g)). Also the more favourable orientation of the flexible wings causes this difference in upward force.

Finally at the end of the in-stroke a difference is seen between the wings. This is clearly different from the single wing force profile, where a large peak was present during the in-stroke. In the case of a single wing this large peak was caused by a

**Table 8.3** Integrated upward force and absolute horizontal force for the 4 wings with different amounts of flexibility performing the 'clap-and-peel' motion. Increase in force coefficients relative to the single wing motion is also stated.

Wing	$\bar{C}_Y$	$\bar{C}_X$	$\frac{\bar{C}_Y - \bar{C}_Y^{single}}{\bar{C}_Y^{single}}$	$\frac{\bar{C}_X - \bar{C}_X^{single}}{\bar{C}_X^{single}}$
Super-flexible	4.47 (45 %)	9.84 (11%)	38 %	42 %
DelFly	4.17 (35 %)	10.15 (15 %)	45 %	64 %
Semi-flexible	3.75 (22 %)	9.52 (7 %)	50 %	77 %
Rigid	3.08 (0 %)	8.86 (0 %)	38 %	65 %

big LEV being developed during this phase. However in the case of 'clap-and-peel' the LEV of the out-stroke remains in the stroke path and is captured by the wing in the in-stroke. Because the size and strength of this vortex in the 'clap-and-peel' motion is significantly bigger the development of a new LEV is slowed down and for a large part prevented. At the end of the in-stroke there is a LEV formed, but also immediately shed because the wing starts to rotate again. This is the same for all four wings. The difference seen in the force profile can better be explained by looking at the pressure field. In Figure 8.12(j), 8.12(k) and 8.12(l) the pressure field is shown for the three wings at 98 % of the period. During the clap phase an important parameter is the pressure between the wings. The higher the pressure the higher the upward force. For a more flexible wing the pressure inside is higher and thus causes a higher upward force together with the orientation of the wing, which has more horizontal area for the flexible wings to generate an upward force. This higher pressure for a more flexible wing can be explained by the amount of volume which is 'trapped' between the wings. For the more flexible the wing is, the more volume is 'trapped' between the wings. All this volume must be pushed downwards during the clap phase. Consequently there is a larger momentum transport downwards when the flexibility of the wings is increased. This momentum change causes an upward force. Together with the more favourable orientation of the more flexible wings, this explains the differences found in the peak during the clap phase. The question remains if this high pressure will be there if fluid-structure interaction would be applied. For a more flexible wing the high pressure will cause the outward deformation, relaxing the pressure. Now the wings are actively deformed and thus the most 'flexible' wing will cause high pressures, without having feedback on its shape. The difference between the single wing motion and the 'clap-and-peel' motion is explained by the high pressure which is possible to build up inside do to the presence of the second wing.

Integrating the upward force coefficient over complete average flapping cycle results in the periodic average upward force. In Table 8.3 these values are shown together with the horizontal force and the relative increase from the single wing results. From this table it is clear that flexibility increases the relative difference with the rigid

**Table 8.4** Energy needed per period for the 4 wings in 'clap-and-peel' motion.

Wing	E [-]	$\frac{E-E_{single}}{E_{single}}$	$\frac{C_y}{E}$
Super-flexible	10.04 (8 %)	25 %	0.445 (35 %)
DelFly	10.80 (16 %)	48 %	0.386 (17 %)
Semi-flexible	10.35 (11 %)	60 %	0.362 (10 %)
Rigid	9.34 (0 %)	54 %	0.330 (0 %)

wing for the flexible wings. Even adding a bit of flexibility (semi-flexible wing) does increase the upward force significantly compared to the rigid wing. Besides the large increase compared to a rigid wing the difference with the single wing motion is also significant. For all wings, including the rigid wing, the integrated average upward force increases when the 'clap-and-peel' motion is performed, with a maximum of 50 % for the semi-flexible wing. Besides the upward force also the horizontal force does increase. Relative to the rigid wing the increase is relatively small. However when the comparison with the single wing is made a large increase is found. This increase varies from 40 % to almost 80 %, which is a relatively larger increase compared to the increase in upward force. This is also reflected back in the required energy. Besides the integrated upward force coefficient also the integrated absolute horizontal force coefficient is shown. It can be seen that the drag increases when the flexibility is increased except for the most flexible wing. This gives a first indication on the amount of energy needed to translate this wing. To determine the energy needed, the power needed in time is integrated for the average period. For power calculations the periodic average drag is multiplied by the horizontal velocity of the leading edge. The energy needed per period is computed by integrating over a single period and dividing by the characteristic velocity. In mathematical form this results in Equation (8.1). In Table 8.4 the energy for the four wings considered is shown. It can be seen that the trend seen in the drag is similar to the trend in the energy. While for the single wing there is a clear trend between flexibility and required energy, in the 'clap-and-peel' motion the trend in the required energy is not clear. For the super-flexible wing there is less energy needed compared to the semi-flexible and DelFly wing. Also the increase in energy compared to a single wing is present for all wings, but for a more flexible wing this increase is less when compared to the semi-flexible wing and the rigid wing. As stated before the assumptions made in the calculation of the required energy become less valid for more flexible wings. From these results it cannot be strongly concluded that the super-flexible wing in clap and peel motion is by far the most efficient wing kinematics. However the trend indicates that efficient flapping wings can be achieved by using flexible wings in combination with the 'clap-and-peel' motion. In Figure 8.13 all results are summarized by plotting the upward force coefficient against the required energy. Here the trend in terms of efficiency becomes more clear. For both

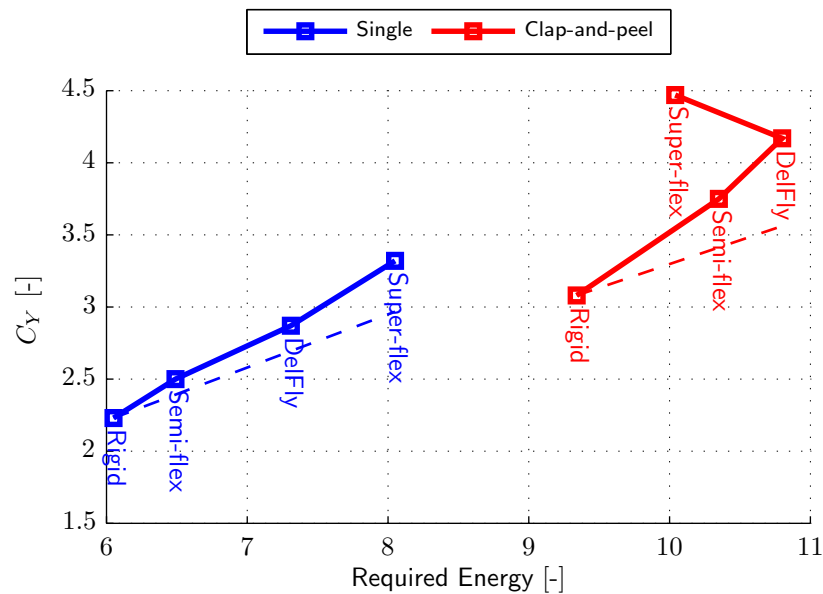


**Figure 8.13** Upward force coefficient against the required energy for the single wing motion and the clap-and-peel motion. All four wings are shown.

the single and the 'clap-and-peel' motion the efficiency increases when flexibility is increased. When comparing the single wing with the 'clap-and-peel' motion the single wing motion performs better in terms of efficiency when looking at less flexible wings. For the DelFly wing there is almost no difference in the efficiency term. For the super-flexible wing an increase in efficiency is found when comparing the single wing motion with the 'clap-and-peel' motion. However, as stated before, the values for the required energy become less reliable for increasing flexibility.

To determine where the difference in the required energy originates from, the power, the horizontal force coefficient and the horizontal leading edge velocity are plotted in a single graph. This is done for two typical wing kinematics ('clap-and-peel' motion for rigid and DelFly wing). In Figure 8.14 this graph is shown. It is immediately clear that the main difference originates from the out-stroke phase of the motion, which is performed from 20 % to 40 % of the period. As seen in the vertical force coefficient, there is significant increase for the DelFly wing in the horizontal force at this phase when compared to the rigid wing. Due to the high horizontal velocity during this phase a larger difference is found in the power, which leads to a difference in the required energy. Another point of interest is the stroke reversal after the out-stroke. For both wings a negative power is found and thus energy is 'created'. This happens because the leading edge already reversed its velocity, while the horizontal force is still in the out-stroke phase. Due to the interaction with the previously shed LEV a suction area is present in front of the wing causing a positive horizontal force and thus prolonging the out-stroke phase in the horizontal force.

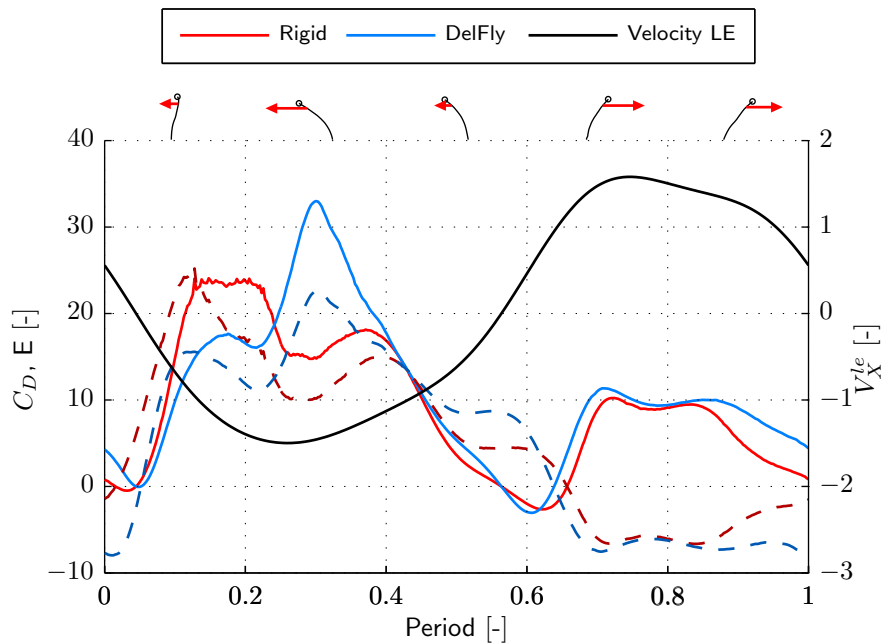


**Figure 8.14** Periodic power, horizontal force coefficient and leading edge velocity for the rigid and DelFly wing in 'clap-and-peel' motion. The full lines represent the power, while the darker dashed lines show the horizontal force coefficient for the two wings. Both wings have the same leading edge velocity and the horizontal component of this velocity is shown by the black line.

### 8.3 Rotated wing and gap size

In the motion enforced during the simulations the minimum gap between the 'two' wings is not equal at the leading and trailing edge. The minimum gap during the cycle is close to the leading edge, while at the trailing edge the gap is slightly larger. As a consequence the known effect of preventing the TEV is not as strong as possibly can be. By rotating the wing the gap at the trailing edge can be minimised. With the original and rotated wing a study into the effect of gap size during flexible clap-and-fling is performed. First the derivation and resulting rotated wing motion is explained, after which this new shape is used in the discussion on the effect of gap size in 'clap-and-peel'.

#### 8.3.1 Rotated wing

To derive the rotated wing two steps are taken. First the position on the wing where the minimal gap during a full flapping period occurs is obtained. This is the point, which moves with the wing in time, where the complete wing is rotated around. By analysing the deformation in time, this point is found to be just below the leading edge. Secondly the angle over which the wing must be rotated is determined. The

goal is to achieve the smallest gap size possible at the trailing edge. By analysing the minimum gap size along the wing chord the angle is obtained. The angle obtained is 3.56 degrees. With this angle the minimum gap at the trailing edge is equal to the global minimum gap present in the original DelFly II wing. To illustrate the difference between the original and rotated wing the two wings shapes are shown in Figure 8.15 for two instances.

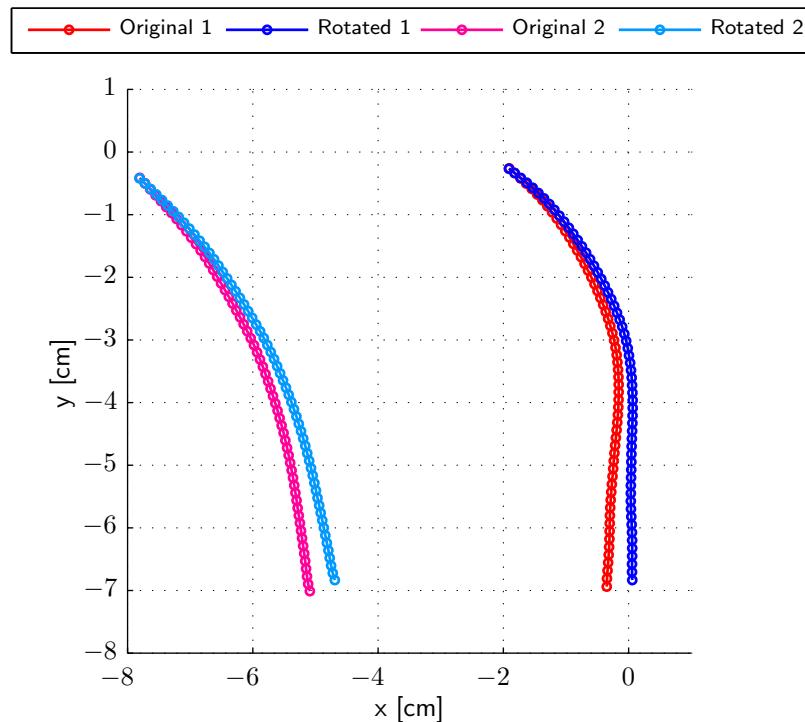


**Figure 8.15** Wing shape of original and rotated wing for two instances during the flapping period.

### 8.3.2 Influence of the gap size

In [31] an investigation into the influence of the gap size on the upward force during clap and fling was carried out with a rigid wing for low Reynolds numbers. They concluded that there is only a slight difference when the gap between the two wings is varied from 20 % to 10 % of the chord. However in this case the motion is different, flexible wings are used, the Reynolds number is higher and chaotic aerodynamics are present. Therefore it is interesting to see if the gap size does influence the 'clap-and-peel' motion significantly when flexible wings are used. To study this effect both the original and the rotated wing are used with different gap sizes. In this

study the gap size is the distance between the wing and the symmetry plane, which is half the distance between the two wings. Gap sizes of 4.7 %, 3.5 %, 2.3 % and 1.2 % are used for both the wings.

**Original wing**

For the original wing the minimum gap at the trailing edge is larger than at the leading edge. The minimum gap size stated in Figure 8.16 is the gap size at the leading edge. In this section the influence of the gap size in the original wing on the forces is studied. In Figure 8.16 the resulting periodic average upward force coefficient can be found for four different gap sizes. It can immediately be seen that

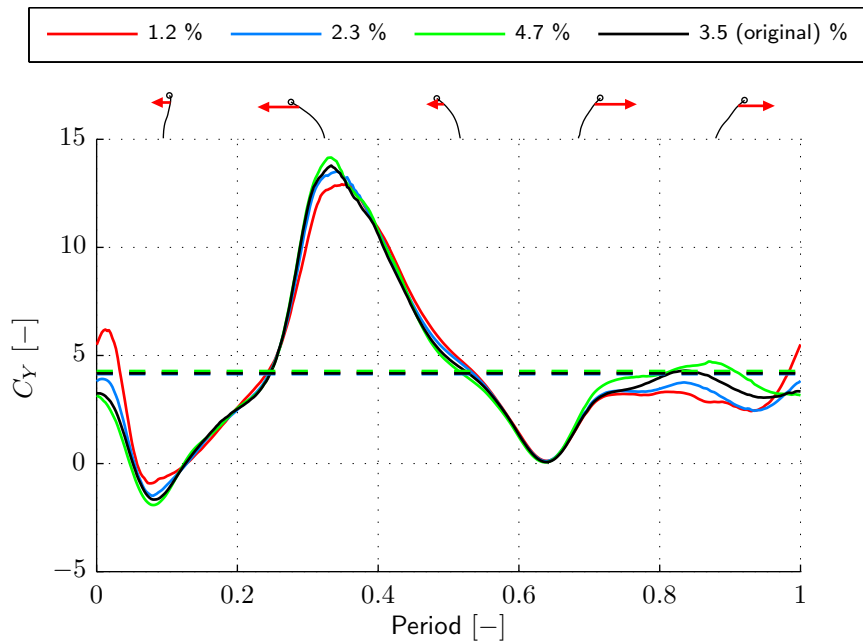


**Figure 8.16** Periodic average upward force for different gap sizes for the original DelFly II wing in clap-and-peel motion.

the influence on the integrated force is minimal (a couple of percent) and thus not significant. However in the trends a difference is found. During the in-stroke and especially during the clap phase differences are observed. For the two smallest gaps a lower force is found during the in-stroke, but this is compensated by a significantly larger peak during the clap. Especially the last phenomena is directly influenced by the gap size. Because the gap size is reduced the area between the wings is smaller, which directly results in a higher pressure. Because the wing is still slightly orientated horizontally the upward force is increased due to this increase in pressure between the wings. For the trailing edge vortex development no significant influence is found, because in the original wing there is still enough space for the TEV to form.

### Rotated wing

To further investigate the influence of the gap size the wing is rotated to ensure that the gap at the trailing edge is as small as possible (relative to the smallest gap near the leading edge). Again the same four gap sizes are used to determine whether the influence of the gap size is directly related to the force production. In Figure 8.17 the periodic average upward force is shown for the different gap sizes. Similar behaviour can be found as for the original DelFly wing. The in-stroke force

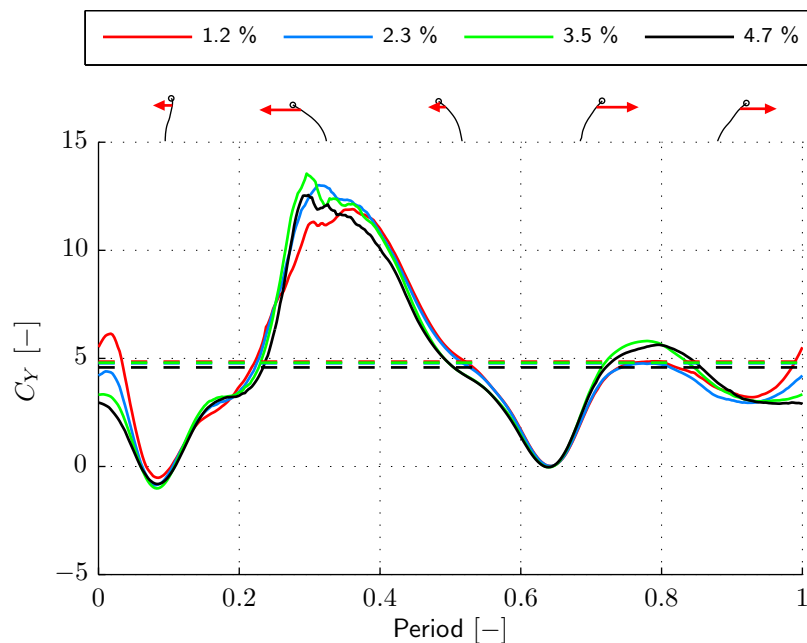


**Figure 8.17** Periodic average upward force for different gap sizes for the rotated DelFly II wing in clap-and-peel motion.

produced is lower for the smallest gap size when compared to the largest gap size. Also at the end of the in-stroke the magnitude of the peak increases for decreasing gap size. Again this last peak can be contributed to the significant increase of pressure between the wings (along the complete chord) when the gap size is decreased. Another difference found in the vortex field is the slight delay in the formation of the trailing edge vortex. In the force profile this can be seen between 14 % and 20 % of the period. The smallest gap size does not show a significant dip. However the resulting differences in the integrated forces are up to 6 %. This is of the same order as the influence of solver parameters and thus not a convincing difference. Again the force profile is indeed significantly influenced by the gap size, but on the integrated upward force only a minor difference is found.

In both cases the main difference is caused by the higher pressure between the wings for decreasing gap size. However when fluid-structure interaction would be

included this direct effect on the pressure might be reduced due to the increase of outward deformation due to this specific pressure build up.

**Original versus rotated wing**

When both wings are compared a clear difference can be found in the force. Both in the force profile and the integrated periodic average upward force shows differences. In Figure 8.18 the periodic average of the upward force is shown. From the dashed lines, representing the integrated value, it is clear that the rotated wing has a significantly higher integrated force. The difference between the original and the rotated wing (for both gap sizes) is approximately 15 %. During the clap phase there is no

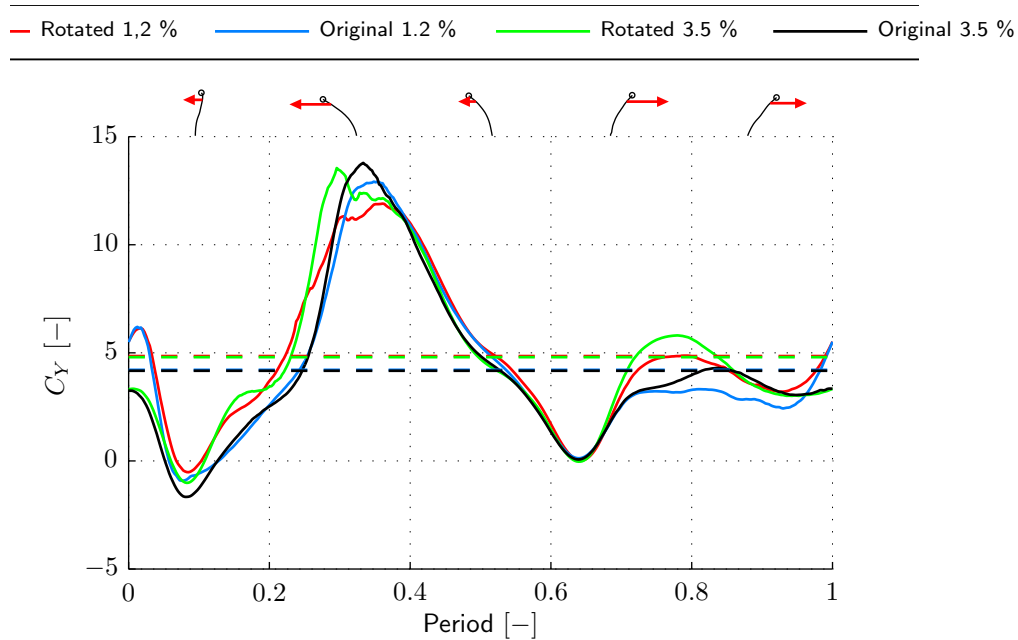


**Figure 8.18** Periodic average upward force for two different gap sizes for both the original and rotated Delfly II wing in clap-and-peel motion.

difference found between the two wings. The only difference visible is caused by the gap size. Essential for the increase in force for the rotated wing is the moment the LEV starts forming. For the rotated wing the out-stroke angle of attack is lower, which already starts during the fling phase. Due to this the LEV can start forming slightly earlier, while it stays attached during the rest of the translational phase. Because this a relatively long part of the period the integrated force is increased significantly.

Also during the in-stroke a small increase is seen in the force. During this part of the motion the angle of attack is slightly increased causing a LEV to be formed and causing the force to increase. Even though this LEV is shed rather soon, this short part of the phase where the LEV is attached does increase the force.

These last results show how much impact a small deviation in the motion can have on the forces, both in the periodic average as well as in the integrated force.

# 9

## Conclusion and recommendations

### 9.1 Conclusions

In this thesis the influence of flexibility on flapping wings performing the 'clap-and-peel' motion is studied. Four wings (with different flexibility) are simulated in single wing motion and while performing the 'clap-and-peel' motion. To accomplish this, the RBF mesh interpolation is further improved and two new methods (immersed symmetry plane and topology changing method) are developed to simulate the 'clap-and-peel' motion. Conclusions are reached on all of these aspects and will be stated in this chapter.

#### RBF mesh interpolation

First the mesh deformation was studied to determine whether the RBF mesh interpolation would be a good method to move the mesh in a smooth way.

- A double row of control points is required to preserve the mesh quality. A single row of control points will only interpolate the translation into the mesh, while the second row ensures that the wing rotation is also interpolated. In this way the mesh remains locally perpendicular to the wing and preserves the mesh quality throughout the flapping cycle.

#### Enforcing the wing kinematics

To use the recorded wing shapes in the simulations Fourier series interpolation in time is used, to generate a continuous and periodic function for the motion.

- Fourier series interpolation ensures a continuous function in the acceleration, which is needed to prevent discontinuities in the pressure field.
- The highest mode used in the Fourier series interpolation will dominate the acceleration. Due to this the dominating frequency in the force is equal to the highest mode used in the Fourier series interpolation. This is caused due

to the strong relation between the acceleration and the pressure, especially in incompressible flow.

- When enforcing a wing without fluid-structure interaction the interpolation will have a large effect on the results. Ensuring a strict approximation in space does not automatically make the simulations more realistic. The most important parameter during such simulations and interpolations is the acceleration of the wing.

### Periodic chaotic flow

Simulations of the flapping wings in hovering conditions show periodic chaotic forces. Based on the analysis of this chaotic behaviour these conclusions follow.

- A global circulatory flow is observed in the results. This flow pattern transports previously shed vortices back into the stroke plane in an irregular interval. Together with the vortices which remain near the wing chaotic aerodynamics are created despite the periodic motion.
- Adding a global convective flow (free-stream velocity) both these phenomena can be eliminated by transporting the vortices downwards. A free-stream velocity of 2 m/s or higher will result in a periodic flow.
- During hovering conditions all parameters do have a significant influence on the instantaneous flow. All four solver parameters, which were varied, started with a small difference ( $10^{-6}$ ) in the upward force coefficient and grew exponentially with a Lyapunov coefficient of 50. Until the difference between the results obtained is of the same order as the results itself this exponential growth continued. This results in instantaneous force profiles to differ in the same order as the solution itself after 4 periods of simulation.
- Averaging a large number of periods a converged periodic average can be found. The differences between the solver parameters on the integrated periodic average can be up to 4 %. Differences in this order cannot be considered significant when analysing physical phenomena.

### Mesh and Courant number study

Both the periodic and the chaotic flow is used to determine the mesh density needed for accurate simulations.

- For a periodic flow there is a clear convergence of results. The difference between the coarse (15.000 cells) and fine mesh (230.000 cells) is of the same magnitude as can be caused by varying solver parameters in chaotic flow. Only the coarsest mesh (6.000 cells) shows a large difference.

- Based on the chaotic flow results the normal mesh (60.000 cells) is a good choice in terms of accuracy and efficiency. However for 'clap-and-peel' motions no parallel processing is available. Therefore the coarse mesh (15.000 cells) is used, which still captures the periodic behaviour correctly according to the mesh study.
- Based on the results a Courant number of 0.8 is sufficient to obtain accurate results, however a Courant number of 0.4 is used to ensure stable calculation when using the mesh topology changing method for the immersed symmetry plane.

### **Symmetry plane method comparison**

To simulate the 'clap-and-peel' motion two methods to introduce a symmetry plane into the mesh are tested: an explicit interpolation of the symmetry conditions on the surrounding cells and a topology changing algorithm to enforce the symmetry conditions implicitly at the correct location.

- At a low Reynolds number (128), using the Miller and Peskin motion from [25], small numerical oscillations are present in the explicit interpolation method. For larger Reynolds numbers these oscillations increase dramatically. This is due to the explicit nature and interpolation of this method.
- Oscillations can be reduced by increasing mesh resolution and thus decreasing the cell size.
- The topology changing method does provide a reliable and robust method independent of the Reynolds number (in the range which is investigated), without numerical oscillations.
- Using the mesh topology changing method shows good agreement with the clap and fling results from [25], which uses a immersed boundary method and simulates two wings instead of using a symmetry plane. Using an immersed symmetry plane to model the second wing is an appropriate method to simulate 'clap-and-peel' motion in hovering conditions.
- Results from a 'zero-thickness' wing and a single cell thickness wing only show small deviations and thus can be used both as wing topology.

### **Influence of flexibility**

Four different wings are used in the simulations to study the influence of a flexible deforming wing on the aerodynamics and performance. A rigid and three flexible (semi-flexible, DelFly and super-flexible) wings are simulated in both single wing motion and 'clap-and-peel' motion.

- Increasing flexibility, and thus deformation, increases the integrated periodic average upward force coefficient. This trend is present throughout all wings used.
- Differences in integrated periodic upward force are up to 45 %, if the rigid wing is compared to the super-flexible wing. These differences are significant compared to the chaotic variations (4 %).
- Bending the leading edge of the wing in the stroke direction before the out-stroke starts causes a stronger and better attached vortex due to the relatively lower angle of attack. The rigid wing sheds the vortex at the beginning of the out-stroke because this low angle of attack at the start of the out-stroke is not possible with a rigid wing.
- The orientation of the flexible wing can create more effective horizontal area during stroke reversal, increasing the upward force compared to a rigid wing.
- Capturing of the previously shed vortex influences the development of the new LEV. For the rigid wing in single wing motion the interaction with the previously shed LEV has a positive effect due to the very fast shedding of the first LEV and fast development of the second LEV. Flexible wings are limited in developing a LEV in the in-stroke due to the capturing of the previous LEV underneath the wing. This is caused by the curvature of the wing.
- During the clap phase in the 'clap-and-peel' motion a higher pressure is present between the wings when flexibility is increased. This results in a higher upward force when flexibility is increased. Due to the larger volume between the two wings, more mass must be transported downward, which increases the momentum change when flexibility is increased and thus the pressure between the wings. As a consequence the upward force during the clap phase increases when flexibility is increased. However the high pressures might prevent the more flexible wings from clapping together when fluid-structure interaction is included.
- The required energy per period increases for increasing flexibility. For the super-flexible wing in 'clap-and-peel' motion this trend is not present. This can be explained by the assumptions used during the calculations of the required energy. By assuming passive flexibility instead of active flexibility (which is actually simulated) the validity of the required energy calculations reduces when a more flexible wing is used.
- The ratio of integrated periodic upward force over the required energy increases for increasing flexibility. This is a simple measure of efficiency, which shows that a higher force can be reached and the efficiency can be increased by using flexibility. It should be mentioned that the required energy calculations assumes that the enforced wing shape is close to the shape obtained with

fluid-structure interaction. This assumption becomes less valid when more deformation/flexibility is applied. Therefore the results on efficiency only give a first indication of the trend.

### **Influence of 'clap-and-peel'**

The same wings as used in the single wing motion are used to perform the 'clap-and-peel' motion. From these results conclusions are reached on the influence of the 'clap-and-peel' motion on the performance of these clapping wings.

- The 'clap-and-peel' motion increases the integrated periodic average upward force per wing significantly when compared to the single wing motion. All four wings show this behaviour. The increase is in the range of 40 % to 50 %.
- During the peel phase a low pressure region is created between the wings causing a high velocity over the leading edge. The LEV formed during the out-stroke is therefore much stronger when compared to the single wing.
- The importance of the angle of attack during the start of the out-stroke is shown clearly during the 'clap-and-peel' motion. A lower angle of attack ensures that the LEV stays attached. In the case of this 'clap-and-peel' motion the flow velocities are higher due to the suction region. Therefore the LEV is stronger and thus shedding of the vortex causes a major influence of the produced force.
- Capturing the previously shed vortex prevents the LEV from forming during a large part of the in-stroke. During the in-stroke lower forces are found for all four wings when compared to the single wing motion. This is caused by the stronger LEV in the out-stroke.
- During the clap phase the 'clap-and-peel' motion generates an extra force peak. This peak is caused directly by the presence of the 'second' wing. The volume between the wings can only move downwards and thus creates a momentum change in the vertical direction. This causes the upward force to increase during the clap phase.
- In terms of efficiency the 'clap-and-peel' motion performs slightly less compared to a single wing. Only for the more flexible wings a similar or higher efficiency is reached.

### **Gap size influence**

Different gap sizes are used in the simulations for both the original wing and the rotated wing.

- In the range of gap sizes investigated (1 % to 5 % of the chord) no significant difference in the integrated periodic average upward force is found for either of the two wing kinematics.
- During the clap phase the peak force is increased when a smaller gap is used due to the higher pressure between the wings.
- TEV development can be delayed slightly by using a smaller gap. However no significant influence is found on the forces produced during this phase.
- A small change in the rotation of the wing causes an increase of 15 % in the integrated periodic average upward force. This shows how much a small change in the kinematics can have on the aerodynamics.

### Final conclusions

These simulations showed that the combination of flexible flapping wings with the 'clap-and-peel' motion have the potential to increase the force production while gaining efficiency. Both the flexibility and the 'clap-and-peel' motion show an increase in upward force produced when compared to a rigid wing in single motion. However further investigation is needed including fluid-structure interaction and three dimensional simulations to determine whether these effects will be present during these simulations. The method of efficiency calculations is rather crude and the resulting values should be considered as rough approximations.

## 9.2 Recommendations

Based on the methods used and the results obtained recommendations are given for further research. Several aspect and problems have been discovered during this study into the influence of flexibility on the performance of the 'clap-and-peel' motion. Each of these will be discussed here shortly.

- Add fluid-structure interaction to include the interaction from the flow on the structure. Especially for the more flexible wings this is important. Doing this will reduce the direct influence of high acceleration of the wing on the forces found, since the deforming wing will damp this direct interaction. Another reason to go to full fluid-structure interaction is to eliminate the influence of interpolation between shapes in time. If an intermediate step is desired a simple algorithm can be developed which can 'relax' the wing shape, enforced in the simulations, based on the pressure at the wing. This will include a simple form of damping. However a step to full fluid-structure interaction will result in a more realistic simulation if a correct structural model can be found/developed.

- Go to 3D simulations. All methods discussed and used can be adjusted to work in three dimensions too. This step is needed to determine if the mechanisms found during this study in two dimensional simulations will also be present in a three dimensional wing performing the 'clap-and-peel' motion.
- For shorter simulations times a forward flight mode can be chosen to eliminate the chaotic periodic aerodynamics. This eliminates the large amount of periods needed to calculate a converged periodic average.
- Although the topology changing method performs well compared to the explicit immersed symmetry plane interpolation, improvements are needed. Firstly the code should be made parallel, such that more detailed meshes can be used without large calculation times. Also the implementation in OpenFOAM should be changed such that the conditions are applied directly into the matrix without splitting and stitching the mesh, which costs a lot of CPU time.



# A

## Solver charts

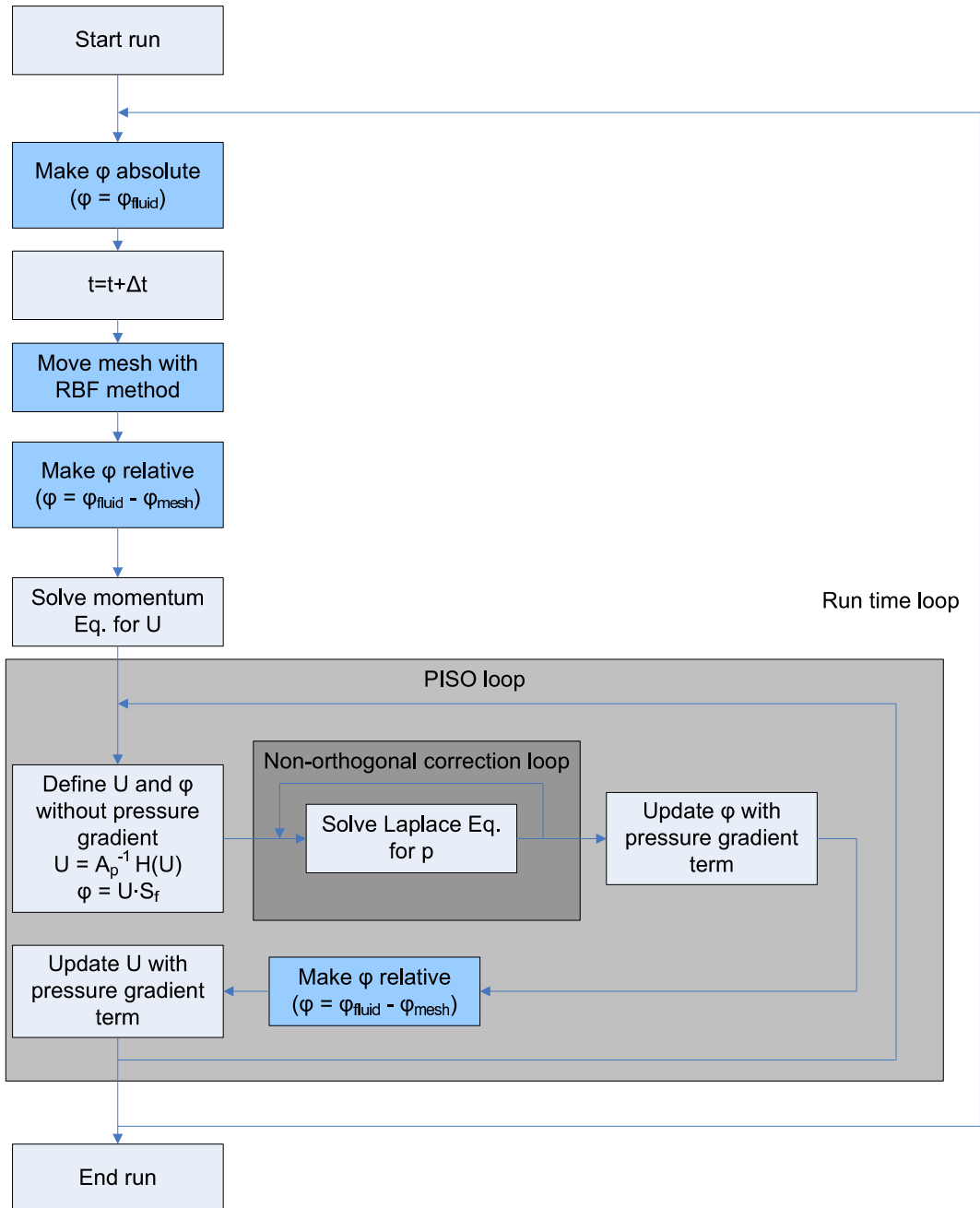


**Figure A.1** Flow diagram describing the PISO loop for moving meshes in OpenFOAM.

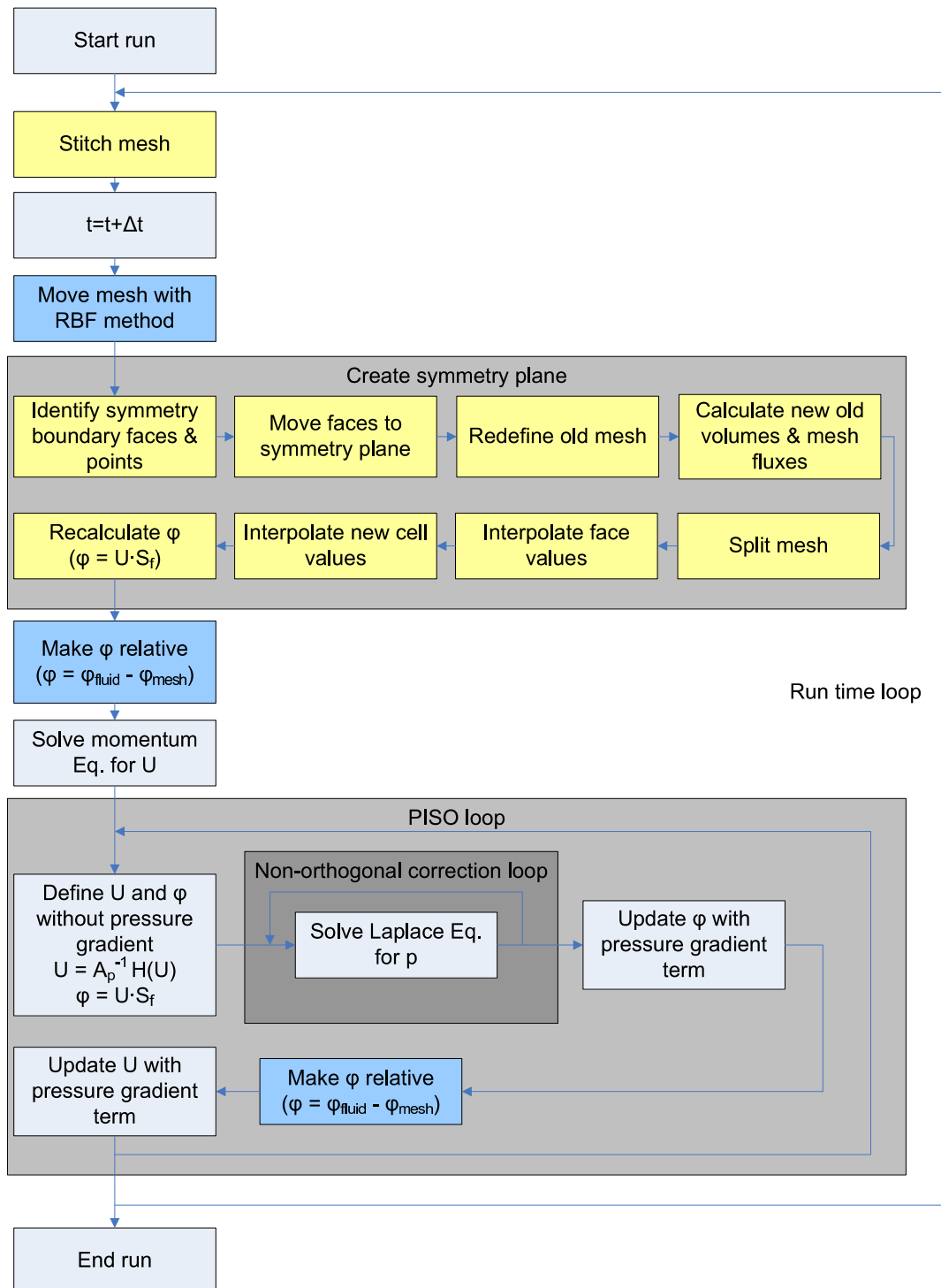


**Figure A.2** Overview of incompressible solver with moving mesh and local topology changes to create a symmetry plane.

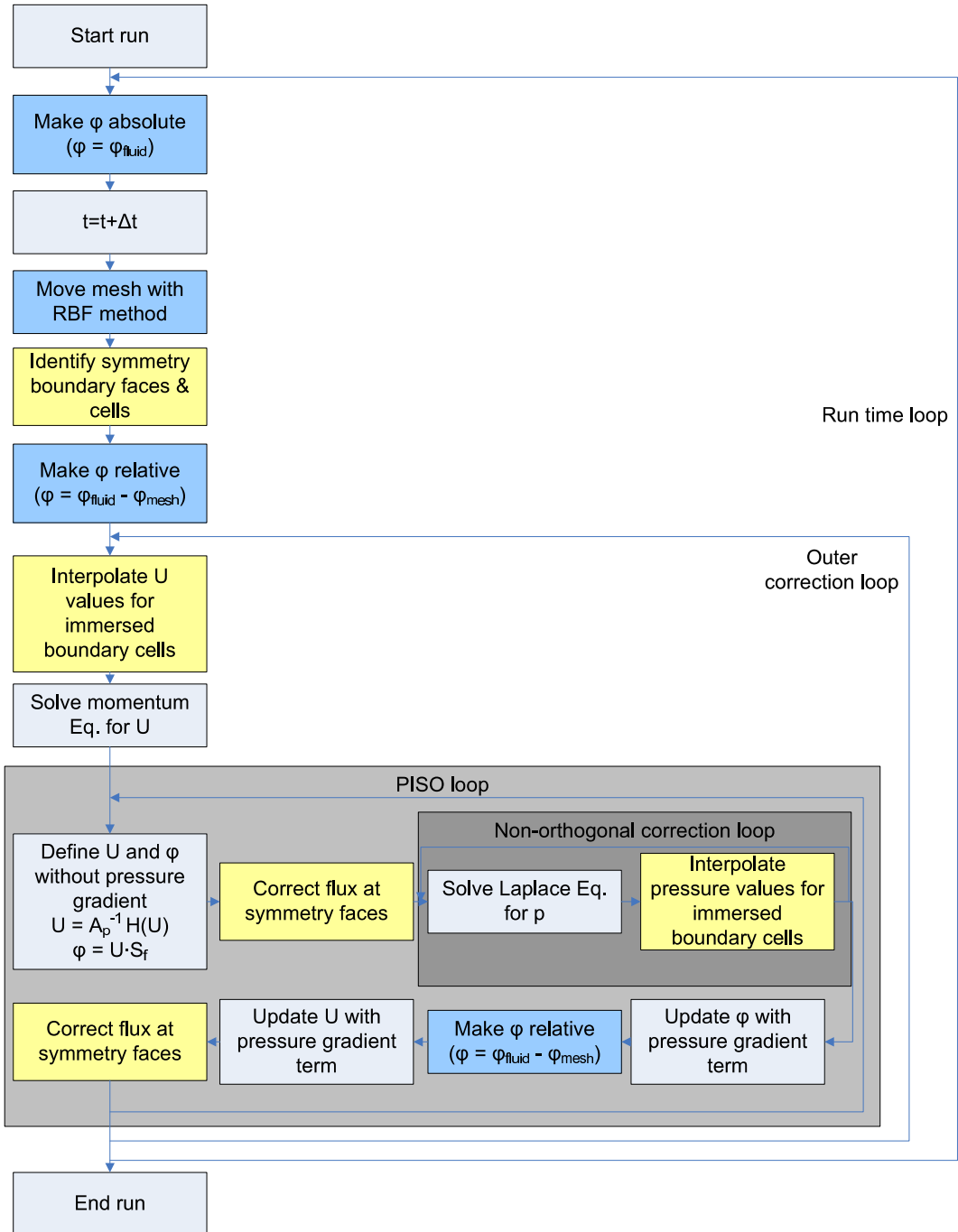


**Figure A.3** Overview of incompressible solver with moving mesh and the immersed symmetry plane.

# B

## Fourier coefficients

Table B.1 Fourier coefficients for x-coordinates used for the interpolation of the wing shapes.

$a_0$	$a_1$	$a_2$	$a_3$	$a_4$	$b_1$	$b_2$	$b_3$	$b_4$
-8.077E-02	1.078E-02	4.644E-03	2.561E-03	-1.865E-03	4.108E-02	-6.848E-04	-3.249E-03	6.278E-04
-8.088E-02	1.120E-02	4.535E-03	2.404E-03	-1.704E-03	4.104E-02	-9.726E-04	-3.100E-03	6.296E-04
-8.083E-02	1.152E-02	4.411E-03	2.303E-03	-1.571E-03	4.087E-02	-1.102E-03	-3.023E-03	6.109E-04
-8.064E-02	1.176E-02	4.274E-03	2.260E-03	-1.476E-03	4.057E-02	-1.085E-03	-3.014E-03	5.803E-04
-8.046E-02	1.201E-02	4.140E-03	2.206E-03	-1.381E-03	4.026E-02	-1.044E-03	-3.027E-03	5.701E-04
-8.033E-02	1.229E-02	4.025E-03	2.126E-03	-1.295E-03	3.996E-02	-1.019E-03	-3.051E-03	5.831E-04
-8.027E-02	1.259E-02	3.940E-03	2.015E-03	-1.213E-03	3.970E-02	-1.017E-03	-3.090E-03	6.247E-04
-8.023E-02	1.291E-02	3.863E-03	1.892E-03	-1.129E-03	3.943E-02	-1.020E-03	-3.125E-03	6.662E-04
-8.018E-02	1.323E-02	3.783E-03	1.772E-03	-1.044E-03	3.915E-02	-1.021E-03	-3.150E-03	7.030E-04
-8.013E-02	1.356E-02	3.698E-03	1.650E-03	-9.536E-04	3.886E-02	-1.015E-03	-3.172E-03	7.362E-04
-8.008E-02	1.389E-02	3.611E-03	1.519E-03	-8.602E-04	3.856E-02	-1.009E-03	-3.197E-03	7.646E-04
-8.003E-02	1.424E-02	3.518E-03	1.373E-03	-7.698E-04	3.827E-02	-9.984E-04	-3.230E-03	7.937E-04
-7.997E-02	1.460E-02	3.425E-03	1.215E-03	-6.847E-04	3.798E-02	-9.859E-04	-3.261E-03	8.198E-04
-7.990E-02	1.496E-02	3.327E-03	1.056E-03	-6.010E-04	3.767E-02	-9.659E-04	-3.288E-03	8.355E-04
-7.981E-02	1.533E-02	3.219E-03	8.963E-04	-5.181E-04	3.734E-02	-9.401E-04	-3.303E-03	8.433E-04
-7.971E-02	1.570E-02	3.111E-03	7.354E-04	-4.438E-04	3.700E-02	-9.094E-04	-3.311E-03	8.458E-04
-7.961E-02	1.608E-02	3.003E-03	5.785E-04	-3.805E-04	3.665E-02	-8.808E-04	-3.318E-03	8.460E-04
-7.950E-02	1.646E-02	2.886E-03	4.218E-04	-3.222E-04	3.629E-02	-8.478E-04	-3.321E-03	8.332E-04
-7.937E-02	1.685E-02	2.764E-03	2.678E-04	-2.742E-04	3.591E-02	-8.101E-04	-3.326E-03	8.077E-04
-7.922E-02	1.725E-02	2.643E-03	1.141E-04	-2.394E-04	3.553E-02	-7.678E-04	-3.330E-03	7.792E-04
-7.910E-02	1.767E-02	2.531E-03	-5.387E-05	-2.143E-04	3.515E-02	-7.303E-04	-3.336E-03	7.555E-04
-7.897E-02	1.809E-02	2.421E-03	-2.240E-04	-1.951E-04	3.477E-02	-6.948E-04	-3.335E-03	7.347E-04
-7.883E-02	1.853E-02	2.313E-03	-3.925E-04	-1.902E-04	3.437E-02	-6.476E-04	-3.328E-03	7.116E-04
-7.869E-02	1.897E-02	2.215E-03	-5.548E-04	-2.041E-04	3.396E-02	-5.947E-04	-3.319E-03	6.899E-04
-7.854E-02	1.942E-02	2.121E-03	-7.050E-04	-2.249E-04	3.352E-02	-5.384E-04	-3.294E-03	6.638E-04
-7.839E-02	1.988E-02	2.025E-03	-8.513E-04	-2.501E-04	3.307E-02	-4.756E-04	-3.256E-03	6.338E-04
-7.822E-02	2.035E-02	1.940E-03	-9.876E-04	-2.777E-04	3.261E-02	-4.122E-04	-3.200E-03	5.950E-04
-7.808E-02	2.084E-02	1.860E-03	-1.119E-03	-3.050E-04	3.213E-02	-3.410E-04	-3.136E-03	5.654E-04
-7.794E-02	2.132E-02	1.790E-03	-1.241E-03	-3.337E-04	3.165E-02	-2.699E-04	-3.063E-03	5.399E-04
-7.782E-02	2.181E-02	1.729E-03	-1.348E-03	-3.625E-04	3.117E-02	-2.013E-04	-2.984E-03	5.150E-04
-7.773E-02	2.229E-02	1.674E-03	-1.441E-03	-3.874E-04	3.068E-02	-1.249E-04	-2.900E-03	4.804E-04
-7.768E-02	2.276E-02	1.620E-03	-1.509E-03	-4.077E-04	3.018E-02	-4.118E-05	-2.803E-03	4.432E-04
-7.765E-02	2.322E-02	1.564E-03	-1.555E-03	-4.232E-04	2.967E-02	4.830E-05	-2.697E-03	4.077E-04
-7.763E-02	2.368E-02	1.502E-03	-1.591E-03	-4.396E-04	2.913E-02	1.272E-04	-2.582E-03	3.741E-04
-7.764E-02	2.414E-02	1.435E-03	-1.618E-03	-4.551E-04	2.857E-02	1.849E-04	-2.458E-03	3.391E-04
-7.768E-02	2.463E-02	1.363E-03	-1.643E-03	-4.651E-04	2.800E-02	2.122E-04	-2.318E-03	2.948E-04
-7.774E-02	2.515E-02	1.300E-03	-1.674E-03	-4.583E-04	2.743E-02	2.232E-04	-2.163E-03	2.606E-04
-7.781E-02	2.569E-02	1.248E-03	-1.706E-03	-4.372E-04	2.686E-02	2.328E-04	-1.996E-03	2.344E-04
-7.790E-02	2.624E-02	1.210E-03	-1.725E-03	-4.125E-04	2.628E-02	2.452E-04	-1.818E-03	2.133E-04
-7.799E-02	2.680E-02	1.175E-03	-1.737E-03	-3.786E-04	2.568E-02	2.636E-04	-1.633E-03	1.948E-04
-7.807E-02	2.737E-02	1.142E-03	-1.742E-03	-3.442E-04	2.508E-02	2.814E-04	-1.448E-03	1.806E-04
-7.816E-02	2.794E-02	1.114E-03	-1.743E-03	-3.116E-04	2.447E-02	2.956E-04	-1.264E-03	1.629E-04
-7.826E-02	2.852E-02	1.090E-03	-1.737E-03	-2.753E-04	2.385E-02	3.022E-04	-1.085E-03	1.610E-04
-7.835E-02	2.910E-02	1.072E-03	-1.722E-03	-2.397E-04	2.323E-02	3.003E-04	-9.096E-04	1.694E-04
-7.845E-02	2.970E-02	1.060E-03	-1.711E-03	-2.020E-04	2.260E-02	2.889E-04	-7.305E-04	1.864E-04
-7.853E-02	3.030E-02	1.055E-03	-1.684E-03	-1.711E-04	2.196E-02	2.770E-04	-5.573E-04	2.070E-04
-7.861E-02	3.090E-02	1.045E-03	-1.637E-03	-1.425E-04	2.130E-02	2.674E-04	-3.897E-04	2.195E-04
-7.868E-02	3.152E-02	1.037E-03	-1.571E-03	-1.206E-04	2.062E-02	2.608E-04	-2.265E-04	2.226E-04
-7.876E-02	3.214E-02	1.030E-03	-1.491E-03	-1.001E-04	1.992E-02	2.553E-04	-6.636E-05	2.184E-04
-7.885E-02	3.277E-02	1.021E-03	-1.402E-03	-8.455E-05	1.921E-02	2.471E-04	9.766E-05	2.157E-04
-7.896E-02	3.341E-02	1.011E-03	-1.315E-03	-6.582E-05	1.848E-02	2.314E-04	2.504E-04	2.128E-04
-7.906E-02	3.405E-02	1.002E-03	-1.214E-03	-4.630E-05	1.773E-02	2.020E-04	4.001E-04	2.056E-04
-7.918E-02	3.468E-02	9.911E-04	-1.102E-03	-1.689E-05	1.697E-02	1.712E-04	5.399E-04	2.012E-04
-7.932E-02	3.532E-02	9.762E-04	-9.819E-04	-1.093E-05	1.619E-02	1.378E-04	6.761E-04	2.012E-04
-7.947E-02	3.596E-02	9.641E-04	-8.429E-04	4.478E-05	1.539E-02	9.194E-05	8.092E-04	2.024E-04
-7.964E-02	3.660E-02	9.607E-04	-6.891E-04	7.829E-05	1.458E-02	3.414E-05	9.387E-04	1.939E-04
-7.982E-02	3.723E-02	9.498E-04	-5.270E-04	1.166E-04	1.375E-02	-4.018E-05	1.048E-03	1.743E-04
-8.005E-02	3.783E-02	9.284E-04	-3.578E-04	1.661E-04	1.290E-02	-1.406E-04	1.134E-03	1.378E-04
-8.035E-02	3.839E-02	8.990E-04	-1.857E-04	2.224E-04	1.206E-02	-2.623E-04	1.183E-03	8.988E-05
-8.091E-02	3.888E-02	8.422E-04	-9.270E-05	3.139E-04	1.137E-02	-4.699E-04	1.206E-03	3.450E-05

Table B.2 Fourier coefficients for y-coordinates used for the interpolation of the wing shapes.

$a_0$	$a_1$	$a_2$	$a_3$	$a_4$	$b_1$	$b_2$	$b_3$	$b_4$
-1.393E-01	3.526E-04	-1.020E-03	-1.617E-04	7.581E-04	8.360E-04	-2.201E-03	4.915E-04	2.154E-04
-1.370E-01	4.255E-04	-1.012E-03	-1.734E-04	7.805E-04	9.418E-04	-2.257E-03	5.332E-04	1.735E-04
-1.346E-01	4.400E-04	-9.931E-04	-1.690E-04	7.830E-04	9.929E-04	-2.247E-03	5.341E-04	1.496E-04
-1.322E-01	4.441E-04	-9.592E-04	-1.701E-04	7.816E-04	1.038E-03	-2.221E-03	5.095E-04	1.452E-04
-1.298E-01	4.515E-04	-9.305E-04	-1.679E-04	7.703E-04	1.071E-03	-2.184E-03	4.856E-04	1.369E-04
-1.273E-01	4.550E-04	-9.087E-04	-1.619E-04	7.609E-04	1.097E-03	-2.136E-03	4.576E-04	1.253E-04
-1.249E-01	4.589E-04	-8.760E-04	-1.591E-04	7.532E-04	1.120E-03	-2.084E-03	4.297E-04	1.108E-04
-1.225E-01	4.657E-04	-8.442E-04	-1.541E-04	7.464E-04	1.142E-03	-2.034E-03	4.002E-04	9.553E-05
-1.201E-01	4.766E-04	-8.183E-04	-1.502E-04	7.403E-04	1.156E-03	-1.976E-03	3.701E-04	8.504E-05
-1.177E-01	4.808E-04	-7.901E-04	-1.426E-04	7.319E-04	1.170E-03	-1.919E-03	3.456E-04	7.040E-05
-1.153E-01	4.877E-04	-7.613E-04	-1.339E-04	7.320E-04	1.188E-03	-1.861E-03	3.174E-04	5.479E-05
-1.130E-01	4.930E-04	-7.307E-04	-1.261E-04	7.241E-04	1.205E-03	-1.795E-03	3.004E-04	3.735E-05
-1.106E-01	4.956E-04	-6.998E-04	-1.195E-04	7.225E-04	1.224E-03	-1.724E-03	2.769E-04	2.220E-05
-1.082E-01	4.985E-04	-6.640E-04	-1.092E-04	7.202E-04	1.244E-03	-1.652E-03	2.461E-04	1.452E-07
-1.058E-01	5.070E-04	-6.317E-04	-1.035E-04	7.229E-04	1.263E-03	-1.583E-03	2.159E-04	-1.985E-05
-1.035E-01	5.168E-04	-5.946E-04	-9.007E-05	7.134E-04	1.289E-03	-1.510E-03	1.857E-04	-3.334E-05
-1.011E-01	5.177E-04	-5.545E-04	-8.035E-05	7.059E-04	1.313E-03	-1.439E-03	1.523E-04	-5.480E-05
-9.874E-02	5.179E-04	-5.134E-04	-7.097E-05	7.039E-04	1.342E-03	-1.365E-03	1.248E-04	-6.737E-05
-9.639E-02	5.159E-04	-4.678E-04	-5.489E-05	6.987E-04	1.365E-03	-1.283E-03	1.026E-04	-8.673E-05
-9.406E-02	5.164E-04	-4.261E-04	-4.068E-05	6.953E-04	1.391E-03	-1.192E-03	8.829E-05	-1.045E-04
-9.173E-02	5.085E-04	-3.838E-04	-2.521E-05	6.850E-04	1.425E-03	-1.106E-03	6.235E-05	-1.281E-04
-8.941E-02	5.044E-04	-3.357E-04	-4.510E-06	6.798E-04	1.449E-03	-1.016E-03	4.273E-05	-1.471E-04
-8.708E-02	4.977E-04	-2.902E-04	1.813E-05	6.771E-04	1.476E-03	-9.216E-04	2.226E-05	-1.688E-04
-8.476E-02	4.871E-04	-2.395E-04	3.904E-05	6.684E-04	1.511E-03	-8.213E-04	-7.980E-07	-1.871E-04
-8.247E-02	4.834E-04	-1.901E-04	6.274E-05	6.631E-04	1.539E-03	-7.180E-04	-2.335E-05	-2.060E-04
-8.018E-02	4.698E-04	-1.407E-04	7.937E-05	6.559E-04	1.574E-03	-6.173E-04	-4.022E-05	-2.243E-04
-7.792E-02	4.631E-04	-9.190E-05	9.897E-05	6.526E-04	1.607E-03	-4.934E-04	-6.846E-05	-2.396E-04
-7.566E-02	4.471E-04	-3.403E-05	1.211E-04	6.429E-04	1.639E-03	-3.884E-04	-9.500E-05	-2.594E-04
-7.339E-02	4.395E-04	1.973E-05	1.384E-04	6.274E-04	1.662E-03	-2.866E-04	-1.183E-04	-2.766E-04
-7.111E-02	4.404E-04	7.399E-05	1.425E-04	6.161E-04	1.680E-03	-1.881E-04	-1.399E-04	-2.891E-04
-6.884E-02	4.414E-04	1.296E-04	1.417E-04	5.877E-04	1.693E-03	-9.469E-05	-1.608E-04	-2.941E-04
-6.656E-02	4.513E-04	1.820E-04	1.411E-04	5.569E-04	1.698E-03	-2.316E-06	-1.841E-04	-2.983E-04
-6.428E-02	4.679E-04	2.415E-04	1.337E-04	5.192E-04	1.703E-03	8.657E-05	-2.063E-04	-3.079E-04
-6.202E-02	4.911E-04	3.050E-04	1.300E-04	4.819E-04	1.708E-03	1.731E-04	-2.279E-04	-3.151E-04
-5.977E-02	5.181E-04	3.673E-04	1.330E-04	4.437E-04	1.714E-03	2.626E-04	-2.412E-04	-3.254E-04
-5.754E-02	5.382E-04	4.312E-04	1.392E-04	4.070E-04	1.717E-03	3.525E-04	-2.521E-04	-3.383E-04
-5.533E-02	5.623E-04	4.991E-04	1.408E-04	3.676E-04	1.710E-03	4.475E-04	-2.644E-04	-3.521E-04
-5.312E-02	5.928E-04	5.711E-04	1.378E-04	3.265E-04	1.704E-03	5.421E-04	-2.749E-04	-3.599E-04
-5.093E-02	6.281E-04	6.467E-04	1.245E-04	2.883E-04	1.694E-03	6.449E-04	-2.906E-04	-3.676E-04
-4.875E-02	6.653E-04	7.169E-04	1.146E-04	2.507E-04	1.679E-03	7.484E-04	-3.037E-04	-3.771E-04
-4.658E-02	7.082E-04	7.854E-04	1.050E-04	2.090E-04	1.659E-03	8.523E-04	-3.138E-04	-3.846E-04
-4.443E-02	7.499E-04	8.525E-04	9.423E-05	1.619E-04	1.637E-03	9.621E-04	-3.292E-04	-3.876E-04
-4.227E-02	7.823E-04	9.149E-04	8.881E-05	1.111E-04	1.617E-03	1.068E-03	-3.457E-04	-3.914E-04
-4.011E-02	8.133E-04	9.841E-04	8.236E-05	6.095E-05	1.599E-03	1.178E-03	-3.609E-04	-3.997E-04
-3.797E-02	8.351E-04	1.050E-03	8.210E-05	1.212E-05	1.579E-03	1.283E-03	-3.769E-04	-4.028E-04
-3.583E-02	8.570E-04	1.116E-03	9.127E-05	-3.748E-05	1.563E-03	1.395E-03	-3.845E-04	-4.079E-04
-3.371E-02	8.767E-04	1.177E-03	9.624E-05	-9.058E-05	1.544E-03	1.513E-03	-3.894E-04	-4.025E-04
-3.162E-02	9.007E-04	1.237E-03	9.771E-05	-1.396E-04	1.525E-03	1.625E-03	-3.903E-04	-3.898E-04
-2.953E-02	9.236E-04	1.301E-03	1.043E-04	-1.964E-04	1.502E-03	1.752E-03	-3.900E-04	-3.768E-04
-2.747E-02	9.480E-04	1.369E-03	1.081E-04	-2.436E-04	1.474E-03	1.887E-03	-3.963E-04	-3.664E-04
-2.541E-02	9.778E-04	1.437E-03	1.151E-04	-2.963E-04	1.443E-03	2.019E-03	-3.977E-04	-3.491E-04
-2.338E-02	1.009E-03	1.498E-03	1.203E-04	-3.440E-04	1.407E-03	2.161E-03	-4.024E-04	-3.280E-04
-2.136E-02	1.043E-03	1.558E-03	1.343E-04	-3.976E-04	1.372E-03	2.307E-03	-4.030E-04	-3.057E-04
-1.935E-02	1.075E-03	1.624E-03	1.511E-04	-4.481E-04	1.334E-03	2.445E-03	-4.009E-04	-2.777E-04
-1.737E-02	1.108E-03	1.695E-03	1.718E-04	-5.067E-04	1.288E-03	2.584E-03	-3.933E-04	-2.413E-04
-1.539E-02	1.142E-03	1.764E-03	1.943E-04	-5.614E-04	1.235E-03	2.728E-03	-3.816E-04	-1.948E-04
-1.343E-02	1.176E-03	1.836E-03	2.145E-04	-6.190E-04	1.182E-03	2.866E-03	-3.588E-04	-1.385E-04
-1.147E-02	1.210E-03	1.912E-03	2.511E-04	-6.657E-04	1.113E-03	2.996E-03	-3.386E-04	-8.225E-05
-9.538E-03	1.287E-03	1.977E-03	2.625E-04	-6.586E-04	1.058E-03	3.065E-03	-2.845E-04	-4.296E-05
-7.585E-03	1.373E-03	2.037E-03	3.199E-04	-6.754E-04	8.971E-04	3.133E-03	-2.271E-04	-1.861E-05



## References

- [1] J. Anderson Jr. *Fundamentals of Aerodynamics*. McGraw-Hill Inc., 2005.
- [2] H. Aono, C. kwon Kang, C. E. Cesnik, and W. Shyy. A numerical framework for isotropic and anisotropic flexible flapping wing aerodynamics and aeroelasticity. In *28th AIAA Applied Aerodynamics Conference*, Chicago, Illinois, July 2010. AIAA 2010-5082.
- [3] H. Beckert, A;Wendland. Multivariate interpolation for fluid-structure-interaction problems using radial basis functions. *Aerospace Science and Technology*, 5:125–134, 2001.
- [4] A. Betz. A paper to explain glider flight. *Zeitschrift fuer Flugtechnik und Motorluftschiffahrt*, 3:269–272, 1912.
- [5] d. A. Boer, v. d. M. Schoot, and H. Bijl. Mesh deformation based on radial basis function interpolation. *Computers and Structures*, 85:784–795, 2007.
- [6] F. Bos. *Numerical simulations of flapping foil and wing aerodynamics*. PhD thesis, Technical University Delft, 2010.
- [7] L. Bull. Researches on the insect flight. *COMPTEs RENDUS HEBDOMADAIRES DES SEANCES DE L ACADEMIE DES SCIENCES*, 149:942–944, 1909. ISSN 0001-4036.
- [8] L. Bull. The inclinations of the wing of the insect during flight. *COMPTEs RENDUS HEBDOMADAIRES DES SEANCES DE L ACADEMIE DES SCIENCES*, 150:129–131, 1910. ISSN 0001-4036.
- [9] D. Chandar and M. Damodaran. Computations of a low reynolds number flexible flapping wing aerodynamics using overlapping grids, January 2009. AIAA 2009-1273.
- [10] J. Donea, S. Giuliani, and J. Halleux. An arbitrary lagrangian-eulerian finite element method for transient dynamic fluid-structure interactions. *Computer methods in applied mechanics and engineering*, 33:689–723, 1982.
- [11] R. Dwight. Robust mesh deformation using the linear elasticity equations. In H. Deconinck and E. Dick, editors, *Computational Fluid Dynamics 2006*. Springer, 2004.
- [12] C. Ellington. The novel aerodynamics of insect flight: applications to micro-air-vehicles. *The Journal of Experimental Biology*, 202:3439–3448, 1999.
- [13] C. Ellington, C. van den Berg, A. Willmott, and A. Thomas. Leading-edge vortices in insect flight. *Nature*, 384:626–630, 1996.

- [14] M. Groen, B. Bruggeman, B. Remes, R. Ruijsink, B. v. Oudheusden, and H. Bijl. Improving flight performance of the flapping wing mav delfly ii, 2010. International Micro Air Vehicle conference and competitions.
- [15] S. Heatcote and I. Gursul. Flexible flapping airfoil propulsion at low reynolds numbers. *AIAA Journal*, 45:1066–1079, 2007.
- [16] B. Helenbrook. Mesh deformation using the biharmonic operator. *International Journal for numerical methods in Engineering*, 56:1007–1021, 2003.
- [17] I. Issa. Solution of the implicitly discretised fluid flow equations by operator-splitting. *Journal of computational physics*, 62:40–65, 1985.
- [18] H. Jasak. *Error analysis and estimation in the finite volume method with applications to fluid flow*. PhD thesis, Imperial College, 1996.
- [19] R. Kautz. *Chaos, The Science of Predictable Random Motion*. Oxford University Press, 2011.
- [20] R. Knoller. The laws of wind resistance. *Flug-und Motertechnik (Wien)*, 3:1–7, 1909.
- [21] J. Lee, J. Kim, H. Choi, and K. Yang. Sources of spurious force oscillations from an immersed boundary method for moving-body problems. *Journal of Computational Physics*, 230:2677–2695, 2011.
- [22] H. Liu and K. Kawachi. A numerical study of insect flight. *Journal of Computational Physics*, 146:124–156, 1998.
- [23] H. Liu, C. Ellington, K. Kawachi, C. van den Berg, and A. Willmott. A computational fluid dynamic study of hawkmoth hovering. *The Journal of Experimental Biology*, 201:461–477, 1998.
- [24] R. v. Loon, P. Anderson, F. v. d. Vosse, and S. Sherwin. Comparison of various fluid-structure interaction methods for deformable bodies. *Computer and Structures*, 85:833–843, 2007.
- [25] L. Miller and C. Peskin. A computational fluid dynamics of 'clap and fling' in the smallest insects. *The Journal of Experimental Biology*, 208:195–212, 2005.
- [26] L. Miller and C. Peskin. Flexible clap and fling in tiny insect flight. *The journal of experimental biology*, 212:3076–3090, 2009.
- [27] R. Mittal and G. Iaccarino. Immersed boundary methods. *Annual Review of Fluid Mechanics*, 37:239–261, 2005.
- [28] M. Rosenstein, J. Collins, and C. De Luca. A practical method for calculating largest lyapunov exponents from small data sets. *Physica D*, 65:117–134, 1993.

- [29] S. Sane. The aerodynamics of insect flight. *The Journal of Experimental Biology*, 206:4191–4208, 2003.
- [30] W. Shyy, H. Aono, S. Chimakurthi, T. P., C.-K. Kang, C. Cesnik, and H. Liu. Recent progress in flapping wing aerodynamics and aeroelasticity. *Progress in Aerospace Sciences*, In Press:1–44, 2010.
- [31] M. Sun and X. Yu. Flows around two airfoils performing fling and subsequent translation and translation and subsequent clap. *Acta Mechanica Sinica*, 19: 103–117, 2003.
- [32] Z. Wang. Dissecting insect flight. *Annual Review of Fluid Mechanics*, 37:183–210, 2005. ISSN 0066-4189. doi: {10.1146/annurev.fluid.36.050802.121940}.
- [33] T. Weis-fogh. Quick estimates of flight fitness in hovering animals, including novel mechanisms for lift production. *Journal of Experimental Biology*, 59: 169–230, 1973.
- [34] F. White. *Viscous fluid flow*. McGraw-Hill Inc., 2006.
- [35] T. Yang and M. Wei. Numerical study of flexible flapping wing propulsion, January 2010. AIAA 2010-533.





